REGULATION OF MICROTUBULE DYNAMICS BY TUBULIN DIVERSITY AND SEVERING ENZYMES

by
Annapurna Vemu

A dissertation submitted to Johns Hopkins University in conformity with

the requirements for the degree of Doctor of Philosophy

Baltimore, Maryland
March 2020

ABSTRACT

Microtubules are cytoskeletal polymers that cycle through polymerization and depolymerization, a phenomenon known as dynamic instability. This behavior is essential for basic cellular functions such as cell division, migration, and morphogenesis. Microtubule dynamics is tightly regulated by two broad mechanisms: 1) intrinsically by tubulin isotypes or tubulin post-translational modifications and 2) extrinsically by various microtubule effectors. While many studies have helped us understand how effectors tune microtubule dynamics, we still do not have an understanding of how tubulin isotypes affect microtubule dynamics. This is because the majority of the microtubule dynamics studies have been performed with brain tubulin. Brain tubulin is heterogeneous, consisting of multiple tubulin isotypes and chemically diverse post-translational modifications making it impossible to understand the contribution of a single tubulin isotype or post-translational modification to microtubule dynamic properties. In the first section of my thesis, I explore the dynamic properties of a recombinant single human unmodified tubulin isotype, α1A/βIII. I also purified unmodified α1B/βI+βIVb tubulin from a stable human embryonic kidney cell line and found that this tubulin composition has dramatically different dynamic parameters than hetergenous brain tubulin. Moreover, I found that the addition of α1A/βIII tuned α1B/βI+βIVb tubulin dynamics proportionally. Finally, I explored how extrinsic factors such as microtubule severing enzymes can modulate microtubule dynamics. Severing enzymes break microtubules in an ATP-hydrolysis dependent manner. They are essential for the generation of microtubule arrays in neurons, the plant cortex, and spindle. Despite their discovery 30 years ago, their effects on microtubule dynamics has remained unknown. We found that severing enzymes extract tubulin dimers out of the microtubule lattice. These “holes” can be repaired by spontaneous GTP-tubulin incorporation along the microtubule shaft. This results in

an increase in microtubule rescue frequency. Moreover, the newly severed ends emerge with a high-density of GTP-tubulin, which protects them from depolymerization. The combination of increased microtubule rescues and stable ends causes microtubule mass and number amplification. Together, my graduate work has shed light on how tubulin diversity tunes intrinsic microtubule dynamics and has surprisingly revealed a mechanism of severing enzyme mediated tubulin exchange along the once-thought static microtubule shaft.

Advisor: Dr. Antonina Roll-Mecak

Primary Thesis Reader: Dr. Kevin O'Connell

Secondary Thesis Reader: Dr. Taekjip Ha

ACKNOWLEDGEMENTS

I want to thank my committee members, Drs. John Hammer, Trina Schroer, and Taekjip Ha for spending a considerable amount of time to meet with me (especially Dr. Hammer for driving all the way from NIH to Hopkins!), providing unique insights into my projects, and for their support throughout my graduate school journey. Thank you to Dr. Kevin O'Conell for reading my dissertation and attending my defense exam. Also, thank you to Drs. Christian Kaiser, Nico Tjandra, and Elijah Roberts for serving on my Graduate Board Oral committee.

I would also like to thank members of the Roll-Mecak lab, past and present who I have had the pleasure of knowing and working with: Dr. Antonina Roll-Mecak for her scientific advice, Drs. Christopher Garnham and Jeff Spector for their infectious humor and their willingness to engage in any discussion, scientific and otherwise, Dr. Aga Szyk for her amazing biochemistry skills and for being a very understanding benchmate during my messy days, Dr. James Park for his witty comebacks and late night pep talks, Dr. Elena Zehr for all of the coffee we have imbibed together whilst discussing science, Drs. Ewa Szczesna and Jiayi Chen for being great desk mates, Max Valenstein, Ian Yu, Keith Keenan, and Steven Cummings for being my very very late night buddies in the lab, Chris Kim and Dr. Kishore Mahalingan for letting me push them into building the gingerbread house together.

Also, I am grateful to all of the collaborators that I have had the chance to work with throughout the years. A special thank you to Dr. Duck-Yeon Lee for all of the mass spec help and Dr. Yi He for all of the fermentor runs. A special thank you to Drs. Joseph Mindell, Kenton Swartz, and Mark Mayer for always attending my talks, being supportive, and asking questions which give me a fresh perspective on my work. A special thank you to Drs. Sharon Milgram,

Rejji Kuruvilla, Phil Wang, and Phil Ryan for their support. I am also thankful to Drs. Orna Cohen-Fix and Kumaran Ramamurthi, and Joan Miller for their unwavering support throughout my graduate career. Thank you to dear dear Julia Jarvis whose empathy and support continue to leave me awestruck and forever grateful.

Thank you to all of my dear friends, Mary, Senta, Sara, Angel, Tomomi, and Monique for all the laughs and comfort calls/text. My humble gratitude and deepest love to my husband and family for everything.

TABLE OF CONTENTS

LIST OF FIGURES

*Figures with data contributed solely by a collaborator.

I have had the good fortune of doing science in a very collaborative environment with amazing scientisits. Some of the scientific work I presented in my thesis has been performed by collaborators. Throughout the chapters in my thesis, on figures with data I did not contribute, I have listed the people who have done the work.

CHAPTER 1: Introduction

Since the early electron microscopy images of microtubules in the 1960s (1, 2), microtubule biology has been a rich area of fascinating biology and exciting discoveries. Together with actin and intermediate filaments, microtubules make up the three cytoskeletal filaments in eukaryotic cells. Microtubules serve many functions in non-dividing and dividing cells. In non-dividing cells, microtubules contribute to cell morphogenesis (3-5) and migration (6, 7), and also serve as cellular highways where microtubule motors can transport cargo (8, 9). In dividing cells, microtubules form the mitotic spindle, which is required for proper chromosome segregation into daughter cells (10, 11). Given, the role of microtubules in essential cellular functions, it is no surprise that disruption of the microtubules or its interacting partners leads to cancer, cardiovascular diseases, infections, as well as neurodegenerative diseases such as Parkinson's, Alzheimer's, and Amyotrophic lateral sclerosis (12-15). In fact, many oncology therapeutics, antifungals, and antitparasitics are microtubule-targeting agents and developing potent microtubule-targeting medicines is an active area of research (16, 17).

To respond to changing cellular environments, microtubules are dynamic, switching between phases of growth and shrinkage, a process known as dynamic instability(18). Dynamic instability allows microtubules to rapidly reorganize within in the cell and not be confined to a particular area or shape within the cell. Microtubule dynamics can be tuned by two factors: 1) intrinsically by tubulin isoforms or potentially by tubulin post-translational modifications (19) or 2) extrinsically, by microtubule associated proteins (20, 21). In this thesis, I explore how intrinsic factors such as tubulin isoforms and extrinsic factors such as severing enzymes tune microtubule dynamic properties.

.

Microtubules are made up of αβ tubulin heterodimers

The basic building block of the microtubule is the alpha and beta-tubulin obligate heterodimer (22, 23). These heterodimers interact with one another longitudinally in a "head to tail" fashion forming a protofilament (24). This longitudinal interaction gives the microtubule polarity where at the minus end, alpha-tubulin is exposed, while at the plus-end, beta-tubulin is exposed (25-27)(Figure 1). Plus ends grow faster than minus ends (28). In cells, the minus ends are typically embedded in the centrosome, the microtubule-organizing center while the plus ends point towards the cell periphery. Protofilaments interact laterally to form a hollow cylindrical tube with an outer diameter of 25 nm. Typically, microtubules are comprised of 13 protofilaments (29, 30). However, *In vivo and in vitro*, microtubules can vary from 11 – 16 protofilaments depending on various factors such as tubulin obtained from different species (31), tubulin isotypes (32, 33), or microtubule associated proteins (MAPs) (34).

Both α- and β- tubulin are made up of compactly folded bodies and negatively charged, disordered C-terminal tails (23, 35). The tubulin body is involved in making tubulin-tubulin interactions within the lattice and the C-terminal tails face the exterior on the microtubule surface (22) (Figure 2A). The C-terminal tails are binding sites of microtubule motors and MAPs, such as tau, MAP2, and severing enzymes (36) (37) (38). The tubulin body is highly conserved (80-95%) in sequence similarity between tubulin isotypes, but there are sequence differences between isotypes at microtubule polymerization interfaces, which could potentially affect microtubule dynamics. The majority of the sequence variation is on the C-terminal tails, where the sequence identity is ~50% between the tubulin tails (39) (Figure 2B). These C-terminal tails are also hotspots for diverse post-translational modifications (36, 40). These modifications range

from simple on/off modifications such as tyrosination, acetylation, and phosphorylation to poly-modifications such as glutamylation and glycylation (Figure 2A).

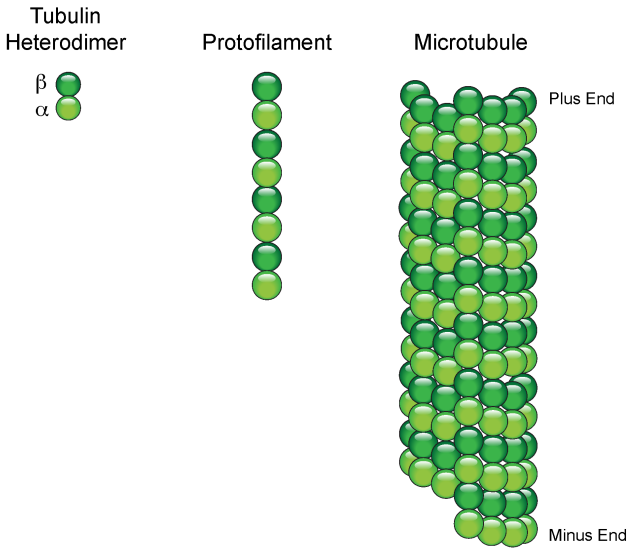

Figure 1: Microtubule Structure

A

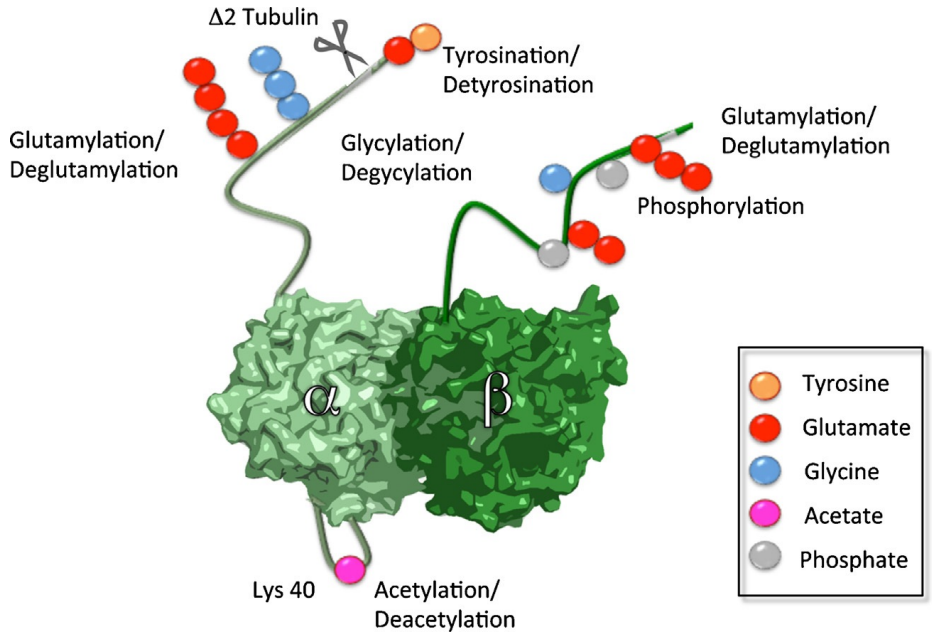

B

```
Hs Alpha 1A     (Q71U36)   EEGEFSEAREDMAALEKDYEEVGVDSVEGEGEEEGEEY
Hs Alpha 1B     (P68363)   EEGEFSEAREDMAALEKDYEEVGVDSVEGEGEEEGEEY
Hs Alpha 1C     (Q9BQE3)   EEGEFSEAREDMAALEKDYEEVGADSADGEDE--GEEY
Hs Alpha 3C     (Q13748)   EEGEFSEAREDLAALEKDYEEVGVDSVEAEAEE-GEEY
Hs Alpha 3E     (Q6PEY2)   EEGEFSEAREDLAALEKDCEEVGVDSVEAEAEE-GEAY
Hs Alpha 4A     (P68366)   EEGEFSEAREDMAALEKDYEEVGIDSYEDEDE--GEE
Hs Alpha 8      (Q9NY65)   EEGEFSEAREDLAALEKDYEEVGTDSFEEENE--GEEF

Hs Beta I       (P07437)   LVSEYQQYQDA--TAEEEEDFGEEAEEEA
Hs Beta II      (Q13885)   LVSEYQQYQDA--TADEQGEFEEEEGEDEA
Hs Beta III     (Q13509)   LVSEYQQYQDA--TAEEEGEMYEDDEEESEAQGPK
Hs Beta IVa     (P04350)   LVSEYQQYQDA--TAEE-GEFEEEAEEEVA
Hs Beta IVb     (P68371)   LVSEYQQYQDA--TAEEEGEFEEEAEEEVA
Hs Beta V       (Q9BUF5)   LVSEYQQYQDA--TANDGEEAFEDEEEEIDG
Hs Beta VI      (Q9H4B7)   LVSEYQQFQDAKAVLEEDEEVTEEAEM-EPEDKGH
```

Figure 2: Structure and sequence of tubulin (Figures are from (39))
A) Structure of αβ tubulin heterodimer showing tubulin post-translational modifications on the C-terminal tails. B) Sequences of α and β tubulin C-terminal tails depicting the sequence difference between isotypes.

Microtubule dynamics are coupled to GTP hydrolysis

Tubulin contains two GTP binding sites (41). One is located on alpha-tubulin, where the GTP is terminally bound in the non-exchangeable site. The other GTP is located in beta-tubulin and is exchangeable (42). The GTP bound to beta tubulin becomes hydrolyzed to GDP after the tubulin dimer becomes incorporated into the microtubule lattice (43, 44). When a microtubule is polymerizing, it grows with a protective GTP tubulin cap because there is a lag between GTP-tubulin incorporation and GTP hydrolysis (18, 45-48). When GTP-cap erodes, GDP tubulin is exposed. GDP-tubulin is unstable and the microtubule depolymerizes or catastrophes (Figure 3). When the microtubule transitions from a depolymerizing phase to a growth phase, it is known as rescue.

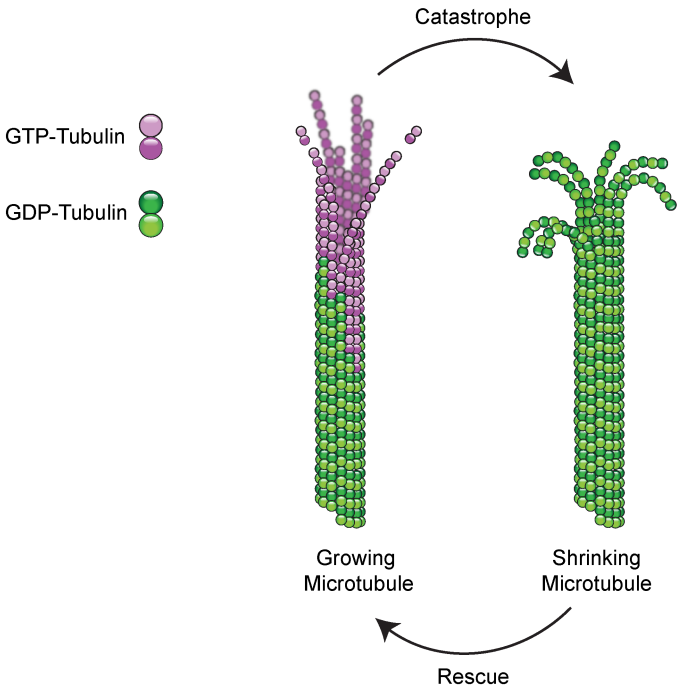

Figure 3: Microtubule cycling through phases of growth and shrinkage.

The tubulin code: multiple tubulin isotypes and tubulin post-translational modifications

In textbooks, microtubules are deceptively depicted as homogenous structures of repeating αβ tubulin heterodimers. However, tubulin is diversified by multiple α- and β-tubulin tubulin isotypes as well as chemically diverse post-translational modifications (19, 40). The combination of different tubulin isoforms and post-translational modifications gives rise to a staggering number of tubulin species. This genetic and chemical diversity of tubulin is the basis for the 'tubulin code', analogous to the histone code (49, 50). This tubulin code has the potential to tune microtubule dynamic properties as well as microtubule effector recruitment(49).

Eukaryotes have multiple tubulin genes (51). Yeast has 2 α- and 1 β- tubulin genes (52, 53), fruit flies have 4 α- and 4 β-tubulin genes (54-56), and humans have 8 α- and 9 β- tubulin genes (19). The majority of the sequence differences between tubulin isotypes are primarily located on the intrinsically disordered C-terminal tails (39). Additionally, there are sequence differences between tubulin isoforms at longitudinal and lateral interfaces that could potentially affect microtubule dynamic properties.

Some tubulin isoforms are ubiquitously expressed, while other isoforms are found in highly specialized cells such as sperm, neurons, and platelets. For example, βI tubulin is ubiquitously expressed (57), while βIII tubulin is found in neuronal cells(58). More information is known about the distribution of β-tubulin isotypes than α-tubulin isotypes. Moreover, it is not known if different α-tubulins have preferences for β–tubulin partners or if the binding between α- and β–tubulins is stochastic. This is because the majority of antibodies used to differentiate between the isotypes use tubulin C-terminal tails as the epitopes. The C-terminal tails of α-tubulin show higher sequence conservation than β-tubulin C-terminal tails. Therefore, there is a lack of antibody specificity between α-tubulin isoforms.

Loss of tubulin isoforms or mutations in tubulin leads to various disorders that have tissue and cell specific pathologies. For example, mutations in βVI tubulin lead to macrothrombocytopenia, affecting platelet formation (59). Mutations in βVIII tubulin leads to impaired oocyte maturation causing sterility (60). Mutations in neuronal βIII tubulin cause several neurodevelopmental disorders (61-63). Knockdown of βIII tubulin leads to delayed radial migration and decreased neuronal progenitor proliferation. Moreover, rescue experiments with other β-tubulin isotypes did not rescue the phenotype indicative of a lack of interchangeability between some tubulin isoforms (63). Another example of tubulin isotype specialization is found in *C. elegans*. While the majority of microtubules in *C. elegans* are made up of 11 protofilaments, *C. elegans* touch receptor microtubules are made up of specialized α-tubulin (MEC-12) and β-tubulin (MEC-7) isoforms that make 15 protofilaments microtubules that are essential for neuronal function (32, 33) (64). Taken together, these results indicate that tubulin isotypes are essential to obtain functional diversity.

Given the tissue specific distribution of tubulin isotypes, it is conceivable that different isotypes could potentially affect: 1) intrinsic microtubule dynamic properties, 2) microtubule structure, 3) mechanical properties, and/or 4) motor and MAP recruitment. In this thesis, I am going to focus on how tubulin isotypes can tune microtubule dynamics. Immunodepletion of βIII tubulin (the alpha-tubulin species that were depleted are unknown) from brain tubulin extracts *in vitro* caused microtubules to assemble twice as fast when compared to brain tubulin extract containing βIII tubulin (65). While brain tubulin has long been used in *in vitro* microtubule studies, it is not an ideal substrate to study microtubule dynamics. Brain tissue is rich in tubulin, therefore it is an excellent source for purifying tubulin using the classical method of polymerization and depolymerization (66). However, this tubulin is heterogeneous and is

composed of multiple α- and β-tubulin isotypes as well as a myriad of post-translational modifications (67). Therefore, using brain tubulin, it is impossible to understand how a single tubulin isoform or a single post-translational modification can tune microtubule dynamics.

Efforts have also been made to study *in vitro* microtubule dynamics from cell sources with less complex tubulin species than the tubulin species found in brain tissue. Tubulin purified from HeLa cells contains βI + βIVb tubulin (the alpha tubulin species is unknown) and had a lower catastrophe frequency when compared to brain tubulin (68). Tubulin purified from chicken erythrocytes contains >90% βVI tubulin and α1 tubulin (which α1 isotype is unknown as there are three isotypes α1A - α1C). Erythrocyte tubulin grows slower and rarely catastrophes when compared to brain tubulin (69, 70). In both of these studies, the alpha tubulin species are unknown and the post-translational modification state of the tubulin is also unknown. Together, these studies show that different tubulin compositions have different microtubule dynamic properties. However, from these studies, it is still unclear how a well-defined tubulin composition, without any post-translational modifications, or a single tubulin isotype can tune microtubule dynamics.

Recent advances in purifying single human tubulin isotypes recombinantly have opened up new possibilities to understand the relationship between tubulin sequence, structure, and function (71). Additionally, a recently developed tubulin affinity purification method developed has allowed us to purify milligrams of tubulin from various sources (72, 73). With these two advances, our lab and others have been able to demonstrate how tubulin isotypes can proportionally tune microtubule dynamics (74-76).

In chapter 2, I discuss how I used the tubulin purification system that was pioneered by the Muto lab (71) to characterize the properties of the isotypically pure human neuronal tubulin.

In chapter 3, I show that unmodified tubulin α1B/βI+βIVb has different dynamic parameters when compared to heterogenous brain tubulin and the dynamic parameters of α1B/βI+βIVb can be tuned proportionally with the addition of α1A/βIII tubulin.

While microtubule dynamic properties can be tuned intrinsically, cells use an arsenal of effectors to tightly regulate the plasticity of the microtubule cytoskeleton. For example, microtubule polymerases such as XMAP215 that can change microtubule growth speeds by an order of magnitude, microtubule depolymerases such as kinesin-13/MCAK family of proteins that promote catastrophe, and factors that promote microtubule rescues, such as the CLASP family of proteins (20, 21). While a lot of effort has been made to study the effects of these proteins on the microtubule cytoskeleton, very little is understood about how a class of enzymes, known as severing enzymes, affect microtubule dynamics.

Introduction to severing enzymes

In addition to a dizzying array of microtubule-associated proteins, cells also express severing enzymes. Severing enzymes cause internal breaks in the microtubule lattice in an ATP-hydrolysis dependent manner. The initial discovery of microtubule severing was made in Xenopus egg extracts (77). Subsequently, the first severing enzyme was purifited form sea urchin eggs and was named katanin, after the Japanese word for sword, 'katana' (78).

To date, there are three known severing enzymes, spastin, katanin, and fidgetin. These enzymes are essential for basic cellular processes such as the generation and maintenance of microtubule arrays in spindles, axons, and cilia (79, 80). Consistent with their involvement in several biological processes, mutations in severing enzymes leads to severe developmental disorders. For example, mutations in spastin lead to hereditary spastic parapeligia, where

individuals lose feeling in lower extremities (81, 82). Mutations in katanin lead to microcephaly and neurological disorders (83, 84).

Severing enzymes belong to the class of meiotic clade of AAA ATPases. They consist of an AAA ATPase domain that harnesses energy from ATP hydrolysis to extract tubulin dimers out of the microtubule lattice. Severing enzymes also contain a Microtubule Interacting and Trafficking (MIT) domain that binds the microtubule lattice (85-88). The AAA and MIT domains are sufficient for severing by spastin and katanin (85, 86, 89). Interestingly, katanin is comprised of a regulatory subunit, p80, which is responsible for katanin's localization and affinity for the microtubule lattice (90-94). In plants, katanin mediated microtubule severing occurs at microtubule crossovers (94). The p80 regulatory subunit is responsible for the precise localization of katanin to these crossovers (93, 94). Some p80 subunits contain a WD40 domain, which localizes katanin to centrosomes (91, 95). While the p80 domain is not required for microtubule severing activity, it enhances katanin's binding to the microtubule lattice (90). This enhanced binding increases microtubule severing activity. On the other hand, spastin's severing activity is robust with the catalytic subunit alone. To date, regulatory subunits for both spastin and fidgetin have not been found.

Severing enzymes have the astonishing capability of disassembling microtubule polymers, whose stiffness has been compared to that of Plexiglas (96), by using energy from ATP hydrolysis (86, 91, 97). The mechanism by which severing enzymes can accomplish this incredible task is being elucidated through structural and *in vitro* studies. Severing enzymes form hexamers in an ATP dependent manner (86). At physiological concentrations, severing enzymes are monomers, but oligomerization is stimulated in the presence of microtubules (86). In the presence of ATP, severing enzymes hexamerize and the central pore is positively charged. The

positively charged pore loop binds negatively charged tubulin tails, which are necessary for severing. Like other AAA ATPases such as the unfoldase CLP-X, it has been proposed that severing enzymes bind the tubulin tails via the central pore. The repeated tugging of the tubulin breaks tubulin-tubulin interactions dislodging the tubulin out of the microtubule lattice. Extraction of multiple tubulin dimers out of the lattice eventually causes the microtubule to sever.

Recent cryo-electron microscopy (EM) structures of katanin have shed light on how ATP hydrolysis is linked to severing enzyme conformational changes. The first structure is an asymmetric spiral structure where all six protomers are ATP-bound and a 40Å gate between the first and sixth protomer (87). Upon ATP hydrolysis, katanin form a planar closed ring conformation (87). The cycling between the spiral and ring structures would provide the power stroke necessary for microtubule severing.

From the name severing enzymes, severing enzymes have long been thought to be microtubule mass destroyers. However, several lines of evidence from cell work suggest that severing enzymes can be microtubule amplifiers. It has been proposed that severing enzymes sever microtubules into multiple smaller microtubules and these severed microtubule act as "seeds" from which new microtubules can grow. This would lead to microtubule number and mass amplification. Therefore, in a context dependent manner, severing enzymes are negative and positive regulators of microtubule mass.

Severing Enzymes as Microtubule Mass Destroyers

Severing enzymes are essential for the formation of the bipolar spindle. In *Xenopus*, katanin is responsible for controlling spindle lengths. Inhibition of katanin lengthened the

spindles and the kinetochore microtubule fibers were long and extended past the bipolar spindle poles (98). Therefore, in Xenopus meiotic spindles, severing enzymes act as microtubule pruners.

Another instance in which severing enzymes act as microtubule destroyers is in *Drosophila* peripheral sensory neuron dendritic pruning (99, 100). Dendritic pruning is the removal of specific neuronal processes that often occurs during development in organisms ranging from *C. elegans* to vertebrates (101, 102). During this process, microtubule disassembly is a feature. Loss of katanin leads to an increase in dendritic elaboration, therefore an increase in microtubule mass (99, 100).

Severing Enzymes as Microtubule Mass Amplifiers

Severing enzymes serving as microtubule amplifiers has been elegantly shown in plants. Severing enzymes function in dense microtubule arrays such as those in spindles and axonal arrays, where severing events cannot be visualized with light microscopy. However, in plants, microtubules are sparse enough to be able to directly visualize severing events. In plants, microtubules serve as tracks for cellulose deposition on the cell wall necessary for cell growth. During phototropism. microtubules and cellulose fibers reorient to facilitate plant growth towards light. Elegant imaging by Lindeboom *et al* has shown that severing enzyme localize to microtubule crossovers between shallow microtubules and existing parallel microtubules (103). Upon severing, the newly severed end continues to grow leading to rapid microtubule mass amplification.

To date, severing mediated microtubule amplification *in vivo* has been only directly viewed in plants due to the sparse microtubule arrays. However, severing mediated microtubule

amplification has been indirectly postulated in meiotic and mitotic spindles. In *C. elegans* female meiotic spindle, electron microscopy tomographic reconstructions tracing individual microtubules have shown that microtubules in the meiotic spindle have many short overlapping microtubules (104). However upon loss of katanin, spindles have reduced microtubule mass containing long microtubules and no short microtubules (104). This study suggests that in spindles, severing enzymes are important for promoting an increase in microtubule number and mass (105, 106).

Neuronal microtubule arrays are another place where severing enzymes can be used to regulate microtubule density. While severing enzyme mediated microtubule amplification has not been directly shown, it is an attractive hypothesis to explain spastin mutant phenotypes. In Drosophila, spastin-null mutants have sparse disorganized microtubules at the synaptic boutons (107). In Zebrafish, spastin knockdown mutants have disorganized sparse axonal microtubule arrays (108).

Typically microtubules are nucleated from a microtubule-organizing center where the minus ends are anchored at the center and the plus ends point radially outwards. However, in systems that lack a centrosome, such as in plants, in female meiotic spindles, and in neurons where there are microtubules far away from the microtubule organizing center (MTOC), there need to be alternative mechanisms to make microtubules (105, 106). Severing mediated microtubule amplification provides an attractive alternative. However, many questions remain regarding the mechanism of severing mediated microtubule amplification. Is severing alone sufficient for amplification? Are there additional factors that are required to stabilize the newly severed ends to promote growth? If severing alone is sufficient, how are the newly severed ends stabilized? These are the questions that I have addressed in my thesis studies.

Mechanistically, severing mediated microtubule amplification in the absence of any stabilizing factors is surprising given what we know about microtubule dynamics. During microtubule polymerization, microtubules have a GTP-tubulin cap because there is a lag between GTP hydrolysis and tubulin incorporation. This GTP-tubulin cap is protective and prevents the microtubule from depolymerizing. When the GTP-cap is lost, GDP-tubulin is exposed. GDP-tubulin is unstable and causes the microtubule to depolymerize (or catastrophe). Classic studies have shown that exposure of GDP-tubulin via UV-ablation or mechanical cuts causes the new plus end to depolymerize (109-114). Severing enzymes break the microtubule in the middle, exposing the GDP-microtubule lattice. Therefore, the prediction would be that severing enzymes should cause microtubules to depolymerize.

The majority of our understanding on severing enzymes comes from *in vivo* studies or *in vitro* studies performed on stabilized microtubules. Despite the discovery of severing enzymes almost 30 years ago, we do not have an understanding of how severing enzymes affect microtubule dynamics. Therefore, in chapter 4, I discuss the role of severing enzymes in regulating microtubule dynamics and microtubule amplification.

CHAPTER 2: Structure and Dynamics of Single-isoform Recombinant Neuronal Human Tubulin

This chapter is re-produced from:
Vemu, A.*, Atherton, J.A.*, Spector, J.O.*, Szyk, A., Moores, C.A., and Roll-Mecak, A. (2016) Structure and Dynamics of Single-isoform Recombinant Neuronal Human Tubulin. *J. Biol. Chem.*
*equal contribution

Abstract

Microtubules are polymers that cycle stochastically between polymerization and depolymerization i.e., they exhibit "dynamic instability". This behavior is crucial for cell division, motility and differentiation. While studies in the last decade have made fundamental breakthroughs in our understanding of how cellular effectors modulate microtubule dynamics, analysis of the relationship between tubulin sequence, structure and dynamics has been held back by a lack of dynamics measurements with and structural characterization of homogenous, isotypically pure, engineered tubulin. Here we report for the first time the cryo-EM structure and *in vitro* dynamics parameters of recombinant isotypically pure human tubulin. α1A/βIII is a purely neuronal tubulin isoform. The 4.2Å structure of unmodified human α1A/βIII microtubules shows overall similarity to that of heterogenous brain microtubules, but is distinguished by subtle differences at polymerization interfaces which are hotspots for sequence divergence between tubulin isoforms. *In vitro* dynamics assays show that, like mosaic brain microtubules, recombinant homogenous microtubules undergo dynamic instability but they polymerize slower and catastrophe less frequently. Interestingly, we find that epitaxial growth of α1A/βIII microtubules from heterogenous brain seeds is inefficient, but can be fully rescued by incorporating as little as 5% of brain tubulin into the homogenous α1A/βIII lattice. Our study

establishes a system to examine the structure and dynamics of mammalian microtubules with well-defined tubulin species and is a first and necessary step towards uncovering how tubulin genetic and chemical diversity is exploited to modulate intrinsic microtubule dynamics.

Introduction

Microtubules cycle stochastically between periods of polymerization and depolymerization; *i.e.*, they exhibit "dynamic instability" (18). This behavior is crucial in cell division, motility and differentiation. Despite the discovery of dynamic instability more than thirty years ago (18) and fundamental breakthroughs in our understanding of microtubule dynamics modulation by cellular effectors (115, 116), analysis of the relationship between tubulin sequence, structure and dynamics has been held back by a lack of structural and *in vitro* dynamics data with homogenous, isotypically pure, engineered tubulin. Eukaryotes have multiple tubulin genes (humans have eight α and eight β-tubulin isotypes) with tissue specific distributions (117). Some microtubules are isotype mixtures, while others are formed from a predominant single isotype (118). Moreover, tubulin is subject to abundant and chemically diverse posttranslational modifications that include acetylation, detyrosination, phosphorylation, glutamylation, glycylation and amination (40, 49). Virtually all biochemical studies have used tubulin purified from mammalian brain tissue through multiple cycles of *in vitro* depolymerization and polymerization (66). While tubulin is abundant in this source, the resulting material is highly heterogeneous, being comprised of multiple tubulin isotypes bearing chemically diverse and abundant posttranslational modifications (36, 58, 119). More than twenty-two different charge variants are repolymerized in random fashion for *in vitro* polymerization assays (67). Thus, microtubules used for *in vitro* dynamics assays have been mosaic, with random distributions of isoforms and posttranslational modifications. Moreover, this purification procedure selects tubulin subpopulations that polymerize robustly while discarding those that do not. Efforts to reduce metazoan tubulin heterogeneity exploited differences in isoform compositions between various tissues or cell lines (e.g. avian erythroctyes

(69) and HeLa cells (68)) or the use of isoform specific antibodies for immunopurification (120). However, neither of these approaches yielded homogenous, single-isoform tubulin.

Here we report for the first time the expression and purification of recombinant isotypically pure unmodified human tubulin competent for *in vitro* dynamics assays and report its dynamic parameters as well as cryo-EM structure at 4.2 Å resolution. We find that isotypically pure unmodified α1A/βIII tubulin exhibits subtle differences in dynamics when compared with heterogenous brain tubulin, consistent with the small conformational rearrangements at tubulin polymerization interfaces revealed by our near-atomic resolution structure of α1A/βIII microtubules. Our study establishes a system to examine the structure and dynamics of mammalian microtubules with well-defined α and β-tubulin species and is a first and necessary step towards exploring the biophysical correlates between sequence, structure and dynamics for mammalian microtubules.

Materials and Methods

Expression and Purification of Human Recombinant Tubulin Constructs

Codon optimized genes for human α1A tubulin (NP_001257328) with an internal His-tag in the acetylation loop and a Prescission protease cleavable C-terminally flag-tagged βIII tubulin (NM_006077) were custom synthesized by Integrated DNA Technologies and cloned into a pFastBac™ -Dual vector as described (71). The internal His-tag in α-tubulin allowed production of an α-tubulin ending in its natural carboxy-terminal tyrosine (38, 121). Without an affinity based selection for α-tubulin, the final sample contains ~30% contamination with endogenous insect α-tubulin species. The Bac-to-Bac System (Life Technologies) was used to generate bacmids for baculovirus protein expression. HighFive or SF9 cells were grown to a density between 1.3-1.6 x10^6 cells/ml and infected with viruses at the multiplicity of infection of 1. Cultures were grown in suspension for 48 hours and cell pellets were collected, washed in PBS and flash frozen. Cells were lysed by gentle sonication in 1XBRB80 buffer (80 mM PIPES pH 6.9, 1 mM $MgCl_2$, 1mM EGTA) with addition of: 0.5 mM ATP, 0.5 mM GTP, 1mM PMSF and 25U/ml benzonase nuclease. The lysate was supplemented with 500 mM KCl and cleared by centrifugation (15 min at 400,000xg). The crude supernatant (supplemented with 25 mM Imidazole pH 8.0) was loaded on a Ni-NTA column (Qiagen) equilibrated with high salt buffer (BRB80, 500 mM KCl, 25 mM Imidazole). His-tagged tubulin was eluted with 250 mM Imidazole in BRB80 buffer. The eluate was further purified on anti-flag G1 affinity resin (Gen Script). Flag-tagged tubulin was eluted by incubation with flag peptide (Gen Script) at 0.25 g/L concentration followed by removal of the tag by Prescission protease. A final purification step was performed on a Resource Q anion exchange column (GE Healthcare) with a linear gradient from 100 mM to 1M KCl in BRB80 buffer. Peak fractions were pooled and buffer exchanged on

a PD10 desalting column (GE Healthcare) equilibrated with BRB80, 20 μM GTP. Small aliquots of tubulin were frozen in liquid nitrogen and stored at –80 °C until use. The purified tubulin was subjected to ESI-TOF LC-MS analysis and detected no endogenous tubulin or posttranslational modifications (Fig.1A). The sensitivity of our mass spectrometric analyses is high enough to detect as little as 1% contaminating posttranslationally modified tubulin species (38). The final yield is ~1 mg of 99% recombinant isotypically pure ab-tubulin per L of SF9 cells.

Cryo-EM Sample Preparation and Data Collection

Recombinant human α1A/βIII tubulin was polymerized at a final concentration of 2.5mg/ml in BRB80 buffer (80mM PIPES, 2mM $MgCl_2$, 1mM EGTA, 1mM DTT) with 1mM GMPCPP or 2mM GTP at 37°C for 1 hour. GMPCPP-bound microtubules were double-cycled by depolymerizing on ice then repolymerized at 37°C for 1 hour with an additional 2mM GMPCPP. Stabilized α1A/βIII microtubules were diluted in BRB20 (20mM PIPES, 2mM $MgCl_2$, 1mM EGTA, 1mM DTT) to a final concentration of 2.5μM. Human kinesin-3 motor domain (Kif1A, residues 1-361 (122) was diluted to 20μM in BRB20 with 2mM AMPPNP. The microtubules and motor were applied sequentially to glow-discharged C-flat™ holey carbon grids (Protochips) and the sample was vitrified using a Vitrobot (FEI Co.). The presence of kinesin motor domain allowed differentiation between α- and β-tubulin during processing. Images were collected with a DE20 direct electron detector (Direct Electron) on a FEI Tecnai G2 Polara operating at 300kV with a calibrated magnification of 52,117x corresponding to a final sampling of 1.22Å/pixel. A total electron dose of ~50e-/$Å^2$ over a 1.5 seconds exposure and a frame rate of 15 frames/second was used, giving a total of 23 frames at ~2.2e-/frame. Dynamic microtubules grown from GMPCPP seeds were polymerized at 2mg/ml for 30 minutes, kept at 37°C throughout and

vitrified as above. Images were collected on a FEI Tecnai T12 operating at 120kV using a 4kx4k CCD camera (Gatan Inc.).

Data Processing for 3D Reconstruction

Individual ~2.2e- frames were globally aligned using IMOD scripts (123) then locally aligned using the Optical Flow approach (124) implemented in Xmipp (125). The full dose of ~50e- was used for particle picking and CTF determination in CTFFind3 (126), whereas ~25e- was used in particle processing to center particles and determine their Euler angles. Euler angles and shifts determined using ~25e- dose were used to generate reconstructions from either the first ~25e- or ~12e- of the exposure. Kinesin-3 microtubules were manually boxed in Eman Boxer (127), serving as input for a set of custom-designed semi-automated single-particle processing scripts utilizing Spider and Frealign as described previously (128) with minor modifications. 10,164 particles or 142,296 asymmetric units were used in the final reconstruction, which was assessed for over-fitting using a high-resolution noise-substitution test (129). Using local resolution estimates determined with the *blocres* program in Bsoft, the reconstruction was sharpened with a B factor of -180 up to a resolution of 5.5Å or 4Å for visualization of kinesin or tubulin densities, respectively. The overall resolution of the reconstruction is 4.2Å (FSCtrue, 0.143 criteria) (129) encompassing a resolution range of ~3.5-5.5Å. The best regions of the reconstruction are within the tubulin portion of the complex (Figures 1B and 2) from which we built an α1A/βIII microtubule model. The quality of our reconstruction was sufficient to confirm that GMPCPP was found in the E-site (Fig. 1C) and GTP in the N-site.

Model Building and Refinement

The polypeptide model of the unmodified α1A/βIII tubulin GMPCPP microtubule was built directly into density in Coot (130) using PDB 3JAT (131) as a starting model. The structure was refined under symmetry restraints in REFMAC v5.8 (132). Secondary structure and reference restraints based on the high-resolution tubulin crystal structure PDB 4DRX (133) were generated with ProSMART (134). Model building in Coot and refinement in REFMAC were repeated iteratively until the quality of the model and fit were optimized.

In vitro Microtubule Dynamics Assays

GMPCPP stabilized seeds were prepared as described (135). The GMPCPP seeds were immobilized in flow chambers using neutravidin as previously described (136). The final imaging buffer contained 1XBRB80 supplemented with 1mM GTP, 100mM KCl, 1% pluronic F-127 and oxygen scavengers prepared as described (137). An objective heater (Bioptechs) was used to warm the chamber to 30°C. All chambers were sealed and allowed to equilibrate on the microscope stage for 5 minutes prior to imaging. Darkfield images were acquired every 5 seconds for 30 minutes. For depolymerization rate measurements the frame rate used was 40 fps. Imaging was performed on a Nikon Eclipse Ti-E equipped with a high NA darkfield condenser, a 100x adjustable iris objective and a Hamamatsu Flash4.0 v2 camera with 2x2 binning. The final pixel size was 108 nm. Darkfield illumination was provided by a Lumencor SOLA SE-II light engine. A Nikon GIF filter was used to protect the seeds from excessive photodamage. All solutions were filtered through a 0.1 μm filter.

Dynamic Parameter Measurements

Using ImageJ, kymographs were generated from dark-field images. Kymographs were traced by hand and dynamic parameters were calculated. Growth and depolymerization rates were determined from the slope of the growing or depolymerizing microtubule in the kymographs. Catastrophe frequency was determined as the number of observed catastrophes divided by the total time spent in the growth phase. Extremely rare rescue events were observed under our experimental conditions and thus were not quantified. Mean microtubule lifetime was calculated as the average time a microtubule spent in the growth phase before a catastrophe. Mean microtubule length was calculated as the average length a microtubule reached before a catastrophe. The probability of nucleation was determined by determining the percentage of seeds that nucleated in 30 minutes in a field of view. Dynamicity was determined as defined in Toso *et al* as the sum of total growth and shortening lengths divided by total time (138). For each condition, 20 microtubules were selected at random for dynamicity calculations.

Results

Near-atomic Resolution Structure of Single-isoform Human α1A/βIII Microtubules

We selected for our study α1A/βIII tubulin. βIII is a neuronal isoform that constitutes 25% of purified brain tubulin (58). It is expressed in non-neuronal tissues only during tumorigenesis (139, 140). It is also the most divergent of all β-tubulin isotypes. It is highly overexpressed in non-neuronal cells upon transformation and has been identified as a strong prognosticator of poor clinical outcomes (140). We expressed human α1A/βIII tubulin in insect cells (71). Through a new double-selection strategy using affinity-tags on both α- and β-tubulin, we produced, for the first time, >99% homogenous, modification-free, single-isotype human αβ-tubulin, free of contamination from endogenous insect tubulins (Figure 1A and see Materials and Methods) that is assembly-competent in the absence of stabilizing drugs like taxol and thus suitable for *in vitro* dynamics assays. Our tagging scheme generates an α-tubulin with a native carboxy-terminus and thus this recombinant tubulin is suitable for the investigation of the effects of the tubulin detyrosination/tyrosination cycle on intrinsic microtubule dynamics and those mediated by the modification dependent recruitment of cellular effectors (141, 142).

To gain insight into the assembly properties of α1A/βIII recombinant tubulin we determined the structure of α1A/βIII microtubules in complex with the GTP analog GMPCPP at near-atomic resolution using cryo-electron microscopy and single-particle image reconstruction (128) (Figures 1B and 2). There is a resolution gradient in the reconstruction, with the best resolution (~3.5Å) within the body of the microtubule (encompassing a resolution range of ~3.5-4.5Å, Figure 2A). The resolution range of the kinesin motor domain, used to facilitate reconstruction is ~4.5-5.5Å. Overall, the reconstruction has a resolution of 4.2 Å resolution (Fourier shell correlation, 0.143 criterion (129), encompassing a resolution range of ~3.5-5.5Å)

(Figures 2B, C and supplemental Table 1)(128). The reconstruction shows clearly resolved β-sheets and α-helical pitch (Figs. 2D, E and F). The majority (92%) of human α1A/βIII GMPCPP microtubules have 14 protofilaments, similar to brain microtubules (143). The tubulin monomer consists of a well-folded globular core and highly negatively charged and flexible C-terminal tails (23). The C-terminal tails are the locus of the greatest chemical heterogeneity in tubulin. They appear disordered in all microtubule structures to date either because (i) they have no unique well-defined conformation or (ii) defined conformations unique to particular isoforms or posttranslationally modified forms are lost during the iterative averaging used in EM reconstructions due to the high heterogeneity of these tails in brain tubulin. Despite the chemical homogeneity of our sample, there is no density attributable to them, indicating that they are intrinsically disordered unless engaged by an effector (39, 144, 145).

Consistent with the high sequence conservation of the tubulin body, our structure is similar to that of heterogenous mosaic mammalian brain GMPCPP microtubules and the overall conformation of the tubulin dimers in our reconstruction is consistent with a GTP-like extended conformation (131) (Figure 1C). The backbone root-mean-square deviation (r.m.s.d) of our tubulin dimer model overlaid on that of the recently published structure of mammalian heterogenous brain GMPCPP 14 protofilament microtubules is <2Å. A difference in the tubulin repeat distance is observed between α1A/βIII and brain microtubules: 82.7 ± 0.2 v*s*. 83.1Å ± 0.0 measured from the EM reconstruction (i.e., model-independent); 82.6 *vs*. 83.2Å measured by comparing models, for a1A/bIII and brain microtubules, respectively (131, 146). However, the tubulin repeat distance for the recombinant α1A/βIII microtubules (~82.7 Å) is roughly comparable with the repeat distance for heterogeneous brain GMPCPP microtubules (~83Å), which is more extended than that of the GDP state (~81.5Å)(131, 146). Nevertheless, we find

two subtle differences that have the potential to impact polymerization dynamics. First, the loop connecting helices H1 and H1' in b-tubulin shifts ~3Å away from the H1'-S2 loop, which makes lateral contacts with the M-loop (microtubule loop) of the neighboring dimer (Figures 1D and E). The M-loop is a sequence element crucial to lateral contacts between adjacent protofilaments. Strikingly, the H1'-S2, H2-S3 and M-loops are a hotspot of sequence variation across β-tubulin isoforms (Figure 1F), consistent with the structural plasticity we observe at this interface. Second, when one a protomer each of brain GMPCPP and recombinant α1A/βIII GMPCPP microtubule protofilaments are superimposed, a clear displacement of successive recombinant α1A/βIII dimers becomes apparent (Fig. 3A). This propagates from the exchangeable GTP-site (E-site) and βIII-tubulin longitudinal interface and results in a progressive stagger that increases with each dimer along the protofilament, such that the first neighboring dimer is offset by 1.7 Å (all Ca r.m.s.d.), the second by 3.4 Å and so on. Together, these relatively subtle structural differences could contribute to differences in dynamic properties. Interestingly, we find that at 6 μM α1A/βIII tubulin, 92% of α1A/βIII GMPCPP seeds nucleate microtubules but only 33% brain seeds nucleate α1A/βIII microtubules (Fig. 3B), suggestive of lattice mismatch effects between the brain microtubule seed and the lattice parameters of the growing α1A/βIII microtubule. This is consistent with the subtle structural differences between α1A/βIII and heterogeneous brain microtubules that we identified (Figures 1D, 1E and 3A). Unexpectedly, robust growth off brain seeds at 6 μM α1A/βIII could be rescued (from 33% to 91%) if as little as 5% brain tubulin was added (Figure 3B). Thus, a small level of tubulin heterogeneity can alleviate the nucleation defect that arises from the potential mismatch between the lattices of the two microtubule types. Our finding has intriguing consequences for the nucleation *in vivo* of microtubules composed of mixtures of tubulin isoforms.

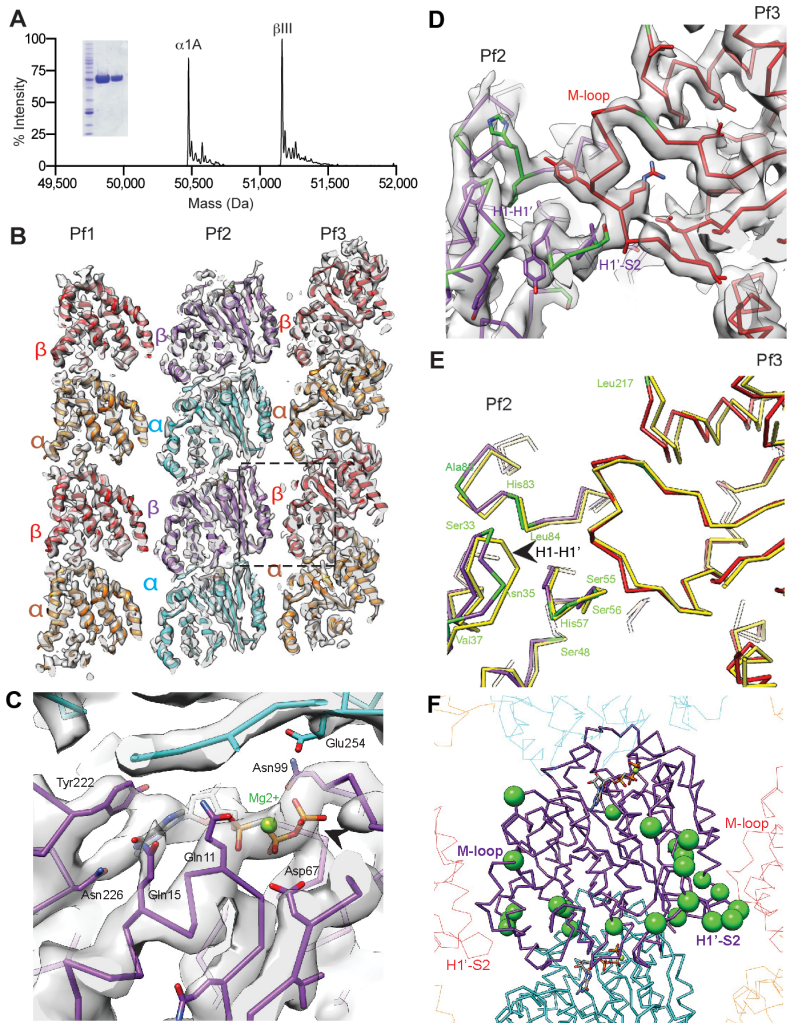

Figure 1: Structure of unmodified single-isoform human α1A/βIII microtubules
A) Mass spectra and SDS-PAGE gel (inset) of recombinant human α1A/βIII tubulin purified to >99% homogeneity. The experimentally determined masses for α1A and βIII tubulin were 50,477.8 Da and 51,163.6 Da, respectively. The theoretical masses for α1A and βIII tubulin are 50,476.8 Da and 51,162.4 Da, respectively. B) Cryo-EM map (4.2Å resolution, 2.8 s contour) and model of GMPCPP recombinant human α1A/βIII microtubules viewed from the lumen (three protofilaments shown). A central protofilament (Pf2) makes lateral contacts with adjacent protofilaments (Pf1 and Pf3); α-tubulin, orange, β-tubulin, red (Pf1, Pf3); α-tubulin, cyan; β-tubulin, purple (Pf2). C) The E-site in βIII-tubulin shows clear density for GMPCPP and its 3 phosphate groups. D) Model and map of the βIII-tubulin lateral interface (boxed and colored as in B). βIII-specific residues are in green. E) Superposition of the α1A/βIII (colored as in B) and brain (PDB: 3JAT; atomistic models of brain microtubules use the βII isotype sequence because it constitutes ~50% of these preparations (131, 145); yellow) microtubule structures; residues specific to βIII are in green. F) βIII sequence variability concentrates at the lateral interface. Green spheres denote residues that are different between the βIII and βII isotypes, the most abundant tubulin isoforms in brain tubulin preparations (58).

Figure 1A contributed by Dr. Agnieszka Szyk (I helped with the tubulin purification) and Figures 1B-F contributed by Dr. Joseph Atherton & Dr. Carolyn Moores.

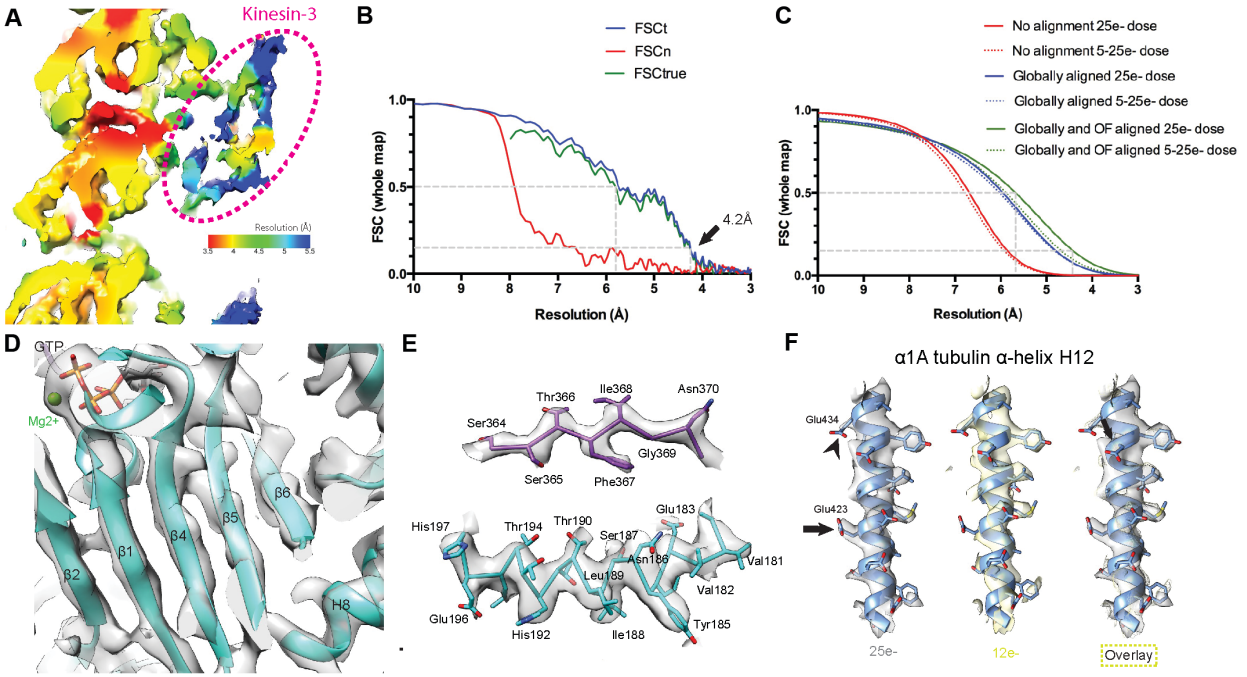

Figure 2: Data processing, map quality and resolution determination for cryo-EM reconstruction of recombinant human α1A/βIII microtubules

A) Local resolution estimates calculated using the Bsoft program blocres (147) were used to color the unfiltered whole reconstruction density. Red density corresponds to 3.5Å resolution, with a continuum of colors indicating increasingly lower resolution, ending with blue at 5.5Å resolution. Tubulin is at a higher resolution, ranging from ~3.5Å in central regions to ~ 4.5Å in more flexible peripheral surface exposed region. While used for the initial alignment, Kinesin-3 is less ordered (resolution of ~ 5.5Å) and excluded from display items. B) Fourier shell correlation (FSC) curves. The gold-standard noise-substitution test (129) on the whole microtubule+kinesin-3 map indicates no over-fitting at high resolution and an overall resolution of 4.2Å (FSCtrue at 0.143 cutoff). C) $R_{measure}$ (148)fitted curves give the same resolution estimate. Global alignment of whole movie frames improved resolution dramatically, while local alignment using an optical flow technique (124) yielded further improvements, especially for frames from early dosing of the data most susceptible to beam-induced motion. D) The higher resolution (< 4Å) in the tubulin dimer core is supported by clear density for the backbone and most side chains (see also panel E). E) Representative density for a β-strand in β-tubulin (top) and an α-helix in α-tubulin (bottom). F) Reconstructions from the first 12e- dose data (yellow) showed improved density for some side chains when compared with the 25e- dose data (grey), regardless of whether they were acidic. The highly negatively charged helix H12 of α-tubulin is shown. Arrowheads indicate acidic side chains that are notable for their different appearance in 12e- and 25e- maps.

Figure 2 contributed by Dr. Joseph Atherton & Dr. Carolyn Moores

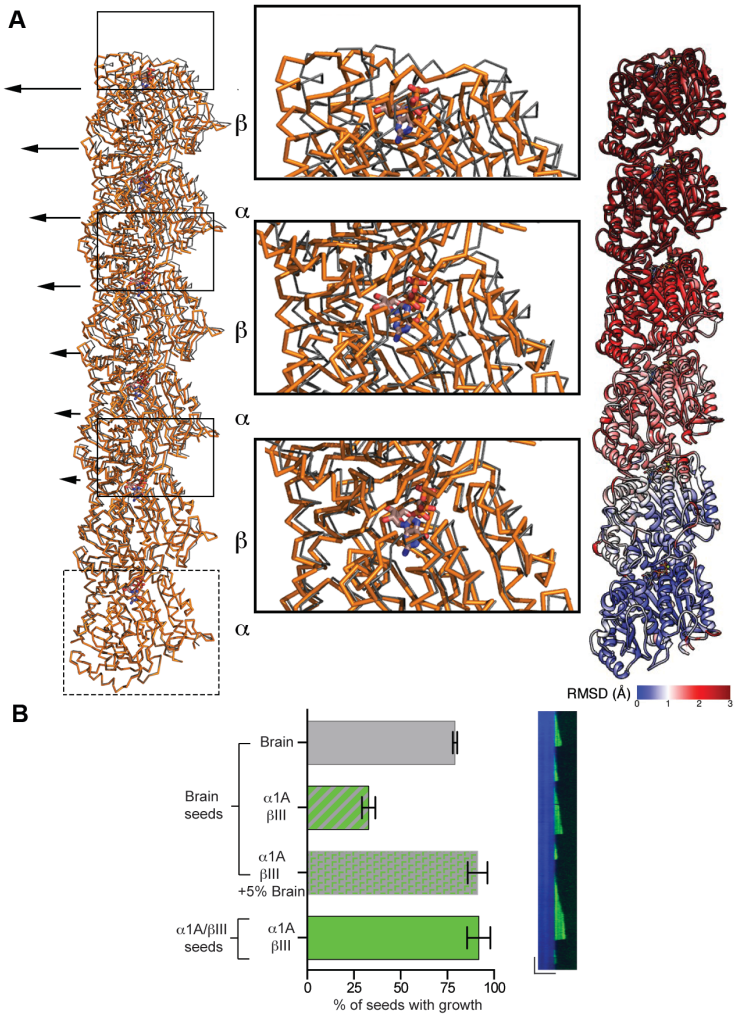

Figure 3: Comparison between α1A/βIII and mosaic brain 14 protofilament microtubule structures A) *Left panel,* Dimer displacement compared to the structure of mosaic brain microtubules PDB: 3JAT(131) as viewed from the microtubule lumen. The boxed α1A-tubulin protomer from the α1A/βIII structure (orange Ca trace) was superimposed on the α-tubulin protomer from the brain microtubule structure (grey Ca trace). Arrows indicate the gradual increase in displacement of the α1A/βIII heterodimers as one advances towards the plus-end of the protofilament. The GTP and GMPCPP in the N-site of α- and the E-site of β-tubulin are shown as ball-and-stick; *Middle panel,* Zoomed in view of regions highlighted by boxes in the left panel showing details of the displacement between the dimers from the recombinant α1A/βIII and brain microtubule structures; *Right panel,* Three a1A/bIII heterodimers within one protofilament colored according to main chain displacement from the brain microtubule structure. (131, 145) B) *Left panel,* Percentage of seeds that nucleate microtubules at 6μM tubulin. Brain, α1A/βIII, α1A/βIII + 5% brain tubulin elongated from brain seeds, α1A/βIII tubulin elongated from α1A/βIII seeds. More than 100 seeds across multiple chambers were counted for these measurements. *Right panel,* Kymograph of microtubule growth for recombinant α1A/βIII at 5.7 μM spiked with 5% Hilyte 488 brain tubulin (0.3μM) from brain GMPCPP seeds showing incorporation of the brain tubulin into the α1A/βIII lattice. Horizontal and vertical scale bar, 5 μm and 2 minutes, respectively.

Figure 3A contributed by Dr. Joseph Atherton & Dr. Carolyn Moores

In Vitro Dynamics of single-isoform α1A/βIII Tubulin

To determine dynamic parameters of single-isoform α1A/βIII tubulin, we performed label-free *in vitro* dynamic assays using darkfield microscopy (149) (Figure 4) so that our dynamic parameters are not confounded by effects arising from the addition of fluorescently labeled brain tubulin to the otherwise homogeneous microtubules. The α1A/βIII microtubules have the typical end-appearance observed for brain microtubules consisting of a mixture of short sheet-like and blunter structures (Figure 4B) (150). To quantify their dynamics, we generated kymographs from time-lapse imaging of dynamic microtubule assays (Figure 4*C*). The growth rates at the plus-end are 35% slower when compared with those of heterogenous brain tubulin while minus-end growth rates are statistically indistinguishable (Figures 4E and F). Consistent with this, the on rate of α1A/βIII tubulin at the plus-end is 1.8 dimers s^{-1} mM^{-1} compared to the 3.6 dimers s^{-1} mM^{-1} for brain tubulin (our measurements for brain microtubules are similar to those reported in (151)). Darkfield imaging allows data collection at the high frame rates needed to determine microtubule depolymerization rates with high accuracy (Materials and Methods). These measurements revealed that α1A/βIII microtubules depolymerize slower than brain microtubules (30.5 ± 1.3 μm/min versus 39.9 ± 1.5 μm/min; Figure 4D). This suggests that microtubules with different chemical compositions (isoform or posttranslational modifications) have the potential to generate different end depolymerization forces that could be harnessed to move cargo in the cell, such as chromosomes during cell division (152).

The catastrophe (the transition between growth and shrinkage) frequency of recombinant microtubules is slightly reduced by 20% and 44% at the plus and minus-ends, respectively when compared with heterogenous brain tubulin (Figures 4E and F). Interestingly, while 46% of brain microtubule exhibit growth at their minus ends, fewer than 7% of recombinant microtubules

display minus-end dynamics under our assay conditions. The difference in firing frequency could be due to α1A/βIII having a harder time growing off of the brain GMPCPP seeds. Early studies reported faster polymerization rates for αβIII tubulin (α denotes here an unknown mixture of α-tubulin isoforms) immunopurified from brain tubulin preparations than for brain tubulin (120). Those studies also found that αβIII tubulin immunopurified from brain tubulin preparations had higher dynamicity than brain tubulin, while our measurements with recombinant α1A/βIII show lower dynamicity for this species than for brain microtubules (1.31 ± 0.05 μm/min *versus* 2.30 ± 0.07 μm/min for α1A/βIII and brain, respectively; Material and Methods). However, it is important to note that the tubulin used in these earlier studies had an unknown a-tubulin composition and a poorly defined mixture of diverse posttranslational modifications, unlike our recombinant tubulin, which contains a single α- and β-tubulin isoform and is unmodified (Figure 1A and Material and Methods). It is unclear at this point whether the subtle differences in dynamics we observe between the recombinant α1A/βIII microtubules and heterogenous mosaic brain microtubules are due to isoform differences and/or the abundant and diverse posttranslational modifications found on brain microtubules. Future studies with recombinantly expressed isoforms and quantitatively defined postranslationally modified tubulin using the expression and purification system described here will shed light on their individual contributions to dynamic instability parameters.

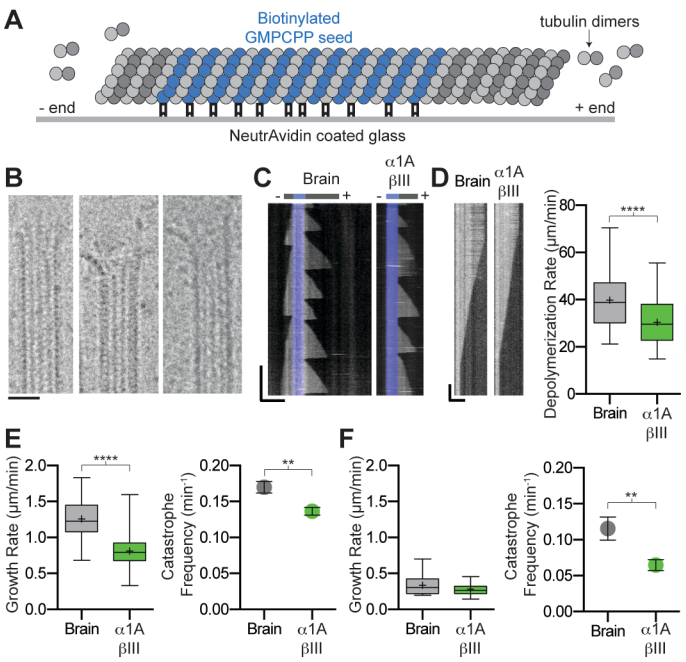

Figure 4: Dynamics of recombinant human α1A/βIII microtubules

A) Schematic of assay design (Experimental Procedures). B) Micrographs of representative dynamic α1A/βIII microtubule ends. Scale bar, 20 nm. C) Kymographs showing typical microtubule growth for brain and recombinant α1A/βIII tubulin at 9 μM. Blue marks the GMPCPP seed. Horizontal and vertical scale bars, 5 μm and 5 minutes, respectively. D*) Left panel*, Kymographs showing a typical depolymerization event for brain and α1A/βIII microtubules. Horizontal and vertical scale bar, 5 μm and 2 seconds, respectively. *Right panel*, Tukey plot showing plus-end depolymerization rates at 9μM tubulin; n = 55 and 58 events for brain and α1A/βIII microtubules, respectively. E) Plus end dynamics of brain and α1A/βIII tubulin at 9 μM tubulin. *Left panel*, Tukey plot showing growth rates; n = 255 and 504 events for brain and α1A/βIII tubulin, respectively. *Right panel*, Catastrophe frequencies; n = 48 and 167 microtubules for brain and α1A/βIII tubulin, respectively. F) Minus end dynamics of brain and α1A/βIII tubulin at 9 μM tubulin. *Left panel*, Tukey plot showing growth rates; n = 32 and 25 events for brain and α1A/βIII tubulin, respectively. *Right panel*, Catastrophe frequencies; n = 7 and 16 microtubules for brain and α1A/βIII tubulin, respectively. Error bars represent s.e.m. ** and ****, *p* values <0.01 and < 0.0001, respectively determined by unpaired *t*-test.

Figure 4B contributed by Dr. Joseph Atherton & Dr. Carolyn Moores. The dynamics data was collected and analyzed by Dr. Jeffrey Spector and me.

Discussion

Using our dual-tag purification system for recombinant tubulin we report for the first time the structure and *in vitro* dynamics parameters for isotypically pure human unmodified microtubules, an essential and important first step in quantitatively establishing the correlates between sequence and dynamics for mammalian microtubules. The dual tag selection system is necessary as a single tag purification strategy results in significant levels of contamination with endogenous tubulin (~30% of insect α-tubulin if α-tubulin is not selected *via* affinity tag purification). Thus, our tagging and purification strategy allows the characterization of both α- and β-tubulin engineered constructs. The majority of *in vitro* dynamics studies presently performed use heterogenous mosaic brain microtubules with isoform composition and posttranslational modifications different from those found *in vivo*, for example in an epithelial cell or the axonal or dendritic compartment of a neuron. A recent study revealed different activities of the *S. cerevisiae* Stu2p on yeast microtubules compared to heterogeneous brain microtubules (153), indicating the importance of examining the effects of regulators with the physiologically relevant tubulin substrate. Our study establishes a system to examine the dynamics of mammalian microtubules with well-defined tubulin species and opens the way to study tubulin isoform-specific effects of microtubule associated proteins and motors and uncover the tubulin sequence elements critical for their recruitment and activation.

Experimental Contributions:

The protocol for recombinant tubulin expression and purification was established by Max Valenstein and Dr. Agnieszka Szyk. The purification of the recombinant tubulin was done by Dr. Agnieszka Szyk and I assisted with the purification. Both Dr. Jeffrey Spector and I performed

the *in vitro* microtubule dynamics and analyzed the dynamics data. Dr. Joseph Atherton from Dr. Carolyn Moores' lab determined the EM structure. Any figures I did not contribute are highlighted throughout the chapter.

Chapter 3: Tubulin Composition Tunes Microtubule Dynamics

This chapter is re-produced from:
Vemu, A., Atherton, J.A., Spector, J.O., Moores, C.A., and Roll-Mecak, A. (2017) Tubulin Composition Tunes Microtubule Dynamics. *Mol. Biol. Cell.*

Abstract

Microtubules polymerize and depolymerize stochastically, a behavior essential in cell division, motility and differentiation. While many studies advanced our understanding of how microtubule-associated proteins tune microtubule dynamics in trans, we have yet to understand how tubulin genetic diversity regulates microtubule functions. The majority of *in vitro* dynamics studies are performed with tubulin purified from brain tissue. This preparation is not representative of tubulin found in many cell types. Here we report the 4.2Å cryo-EM structure and *in vitro* dynamics parameters of α1B/βI+βIVb microtubules assembled from tubulin purified from a human embryonic kidney cell line with isoform composition characteristic of fibroblasts and many cancer cell lines. We find that these microtubules grow faster and transition to depolymerization less frequently compared to brain microtubules, consistent with the higher tubulin on-rate at the microtubule plus-end that is twice of brain tubulin. Interestingly, analysis of EB1 distributions suggests no differences in GTP cap sizes. Cryo-EM reveals that α1B/βI+βIVb microtubules have less tapered ends consistent with the lower curvature for these dimers. Lastly, we show that the addition of recombinant α1A/βIII tubulin, an isotype overexpressed in tumors, proportionally tunes the dynamics of α1B/βI+βIVb microtubules. Our study is an initial step towards understanding how tubulin isoform composition tunes microtubule dynamics.

Introduction

Microtubules are essential dynamic polymers that stochastically switch between cycles of polymerization and depolymerization, a behavior known as dynamic instability (18, 149). Dynamic instability is essential for basic cellular processes such as cell division, motility and differentiation. The building block of the microtubule is the a/b-tubulin heterodimer. Cells use a diverse repertoire of tubulin dimers to build complex structures with diverse architectures and dynamics to perform these basic cellular functions. Eukaryotes have multiple tubulin isotypes; humans have eight α- and eight β-tubulin isotypes (154). While some tubulin isoforms are ubiquitously expressed, other tubulin isoforms are only found in specialized cells such as sperm, neurons and platelets (117, 155-157). *In vivo* studies have shown that tubulin isoforms are not functionally interchangeable suggestive of differential microtubule associate protein (MAPs) recruitment by different tubulin isoforms or changes in intrinsic polymer properties (158, 159). Tubulin is further functionalized through chemically diverse post-translational modifications that include glutamylation, glycylation, acetylation, phosphorylation and amination (40).

The majority of *in vitro* assays are performed with tubulin purified from brain tissue through repeated cycles of polymerization and depolymerization (160). While cost-effective, this procedure generates tubulin that is highly heterogeneous consisting of multiple tubulin isotypes that have chemically diverse and abundant post-translational modifications (58, 67). Most importantly, the composition of tubulin isotypes and tubulin post-translational modifications in these preparations is not representative of that found in most cell types as well as many of the cell lines used routinely in cell biological investigations. Classic studies have reported the characterization of tubulin with less complex compositions purified through polymerization/depolymerization cycles from chicken erythrocytes (70, 161) and Hela cells (68).

A recently introduced affinity purification approach finally enabled the isolation of biochemical amounts of tubulin from various tissues and cell lines (162) that together with recent advances in the expression and purification of pure single isoform human tubulin open a new chapter in the investigation of the biophysical correlates between tubulin sequence, structure and dynamics (71, 74).

Here, we purify tubulin from a human embryonic kidney (tsA201) cell line and report its 4.2Å cryo-EM structure and dynamic parameters. Tubulin purified from this cell line contains no detectable post-translational modifications and consists predominantly of one a-tubulin isoform, α1B and two β-tubulin isoforms, βI and βIVb. This b-tubulin composition is characteristic for fibroblasts (163) as well as many cancer cell lines (164, 165) used for cell biological investigations. *In vitro* dynamic assays show that these microtubules grow faster and catastrophe less frequently than brain microtubules. Moreover, we show that microtubule dynamic parameters vary proportionally with the ratio between non-neuronal tubulin isoforms and a recombinantly produced neuronal tubulin isoform that individually have different dynamic properties. Thus, differential use of tubulin isoforms can have dramatic effects on microtubule dynamics.

Materials and Methods

Affinity purification of tubulin from brain and tsA201 cells

Tubulin from tsA201 cells was purified as previously described (162, 166). Briefly, cells were lysed by gentle sonication in 1XBRB80 pH 6.8 (80mM PIPES, 1mM $MgCl_2$, 1mM EGTA), 1 mM DTT, and 25 μg/ml benzonase. The lysate was cleared by ultra-centrifugation at 444,000Xg for 15 minutes at 4°C. The homogenate was loaded onto a NHS-column (GE Healthcare) coupled to TOG1. The tubulin was eluted with 1XBRB80 supplemented with 0.5 M ammonium sulfate and was buffer exchanged using a PD-10 column (GE Healthcare) into 1XBRB80, 10% glycerol, and 20 μM GTP and was flash frozen in liquid nitrogen. The tubulin was further purified by cycling (167). Tubulin was buffer exchanged using a PD10 column into 1XBRB80 and 20μM GTP and flash frozen in liquid nitrogen. Mass spectrometric analysis of this tubulin indicated that it contains one major α-tubulin (α1B) and two β-tubulin (βI+βIVb) isoforms. Mouse brains were used as a source for TOG affinity based tubulin purification. Wild-type C57/BL6 mice were administered CO_2 gas. Their brains were immediately extracted, washed with cold 1XBRB80 pH 6.8 and flash frozen in liquid nitrogen. Brains were thawed on ice and homogenized in 50 mM Mes pH 6.6, 1 mM $CaCl_2$, 1 mM PMSF and 1 mM DTT using a polytron three times for 5 seconds each at low pulses and three times for 5 seconds at high pulses. The lysate was cleared and tubulin was purified as described above.

Purification of recombinant single-isoform human recombinant tubulin

Recombinant single-isoform human α1A/βIII tubulin was expressed using baculovirus and purified as previously described (74). In brief, a1A with an internal His-tag and βIII with a C-terminal cleavable Flag tag was purified using a Ni-NTA column (Qiagen) and anti-flag G1

affinity resin (Gen Script) to ensure no insect tubulin contamination. The tubulin was further purified by ion exchange chromatography using a Resource Q anion exchange column (GE Healthcare). Peak fractions were combined and buffer exchanged into 1XBRB80 supplemented with 20 μM GTP using a PD10 column.

In vitro microtubule dynamics assays

GMPCPP-stabilized microtubule seeds were prepared as described in Gell *et al* (135). The GMPCPP seeds were immobilized onto neutravidin coated glass as described Szyk *et al* (136). Dynamic assays were performed as described previously (74). The final imaging buffer contained 1XBRB80 pH 6.8 supplemented with 100mM KCl, 1mM GTP, 1% pluronic F-127, and oxygen scavengers. An objective heater (Bioptechs) was used to heat the chamber to 30°C. All chambers were sealed and allowed to equilibrated on the microscope stage for 5 mins before imaging. Darkfield images were taken once every 5 seconds. Image acquisition for the determination of accurate depolymerization rates, was performed at 40 frames/second. Kymographs were generated from darkfield images using the Multi Kymograph Plugin in ImageJ. Kymographs were hand traced and dynamic parameters were quantified as described (74).

Microtubule cryo-EM sample preparation

α1B/βI+βIVb tubulin was polymerized at 37°C for 45 minutes at a final concentration of 2.5mg/ml in BRB80 buffer (80mM PIPES, 2mM $MgCl_2$, 1mM EGTA, 1mM DTT) with 1mM GMPCPP. GMPCPP-bound microtubules were double-cycled by depolymerizing GMPCPP microtubules on ice for 5 minutes then repolymerizing at 37°C for 45 minutes after adding

additional 2mM GMPCPP. GMPCPP-bound MTs were diluted to a final concentration of 2.5 μM in BRB20 buffer (20mM PIPES, 2mM $MgCl_2$, 1mM EGTA, 1mM DTT) and added to glow-discharged C-flat™ holey carbon grids (Protochips, 2 μm holes, 4 μm spacing). 20 μM human kinesin-3 motor domain (Kif1A, residues 1-361, see (122)) in BRB20 containing 2mM AMPPNP was applied to the grid, and the sample was blotted then vitrified in liquid ethane using a Vitrobot (FEI Co.) operating at 25°C and 100% humidity.

Dynamic microtubules were prepared by polymerizing 5mg/ml a1B/bI+bIVb or bovine brain tubulin in BRB80 buffer with 1mM GTP at 37°C for 2 minutes. The sample was applied to holey carbon grids in a Vitrobot (FEI Co.) operating at 37°C and 70% humidity and allowed to polymerize for a further minute before blotting and vitrification in liquid ethane.

Data Collection and Sub-frame processing for 3D reconstruction

Images of microtubule-kinesin complexes were collected on a FEI Tecnai G2 Polara operating at 300kV with a DE20 direct electron detector (Direct Electron) with a calibrated magnification of 52,117x corresponding to a final sampling of 1.22Å/pixel and a defocus range of 0.5-3.5μm. A total electron dose of ~50e-/Å^2 over a 1.5 seconds exposure and a frame rate of 15 frames/second was used, giving in a total of 23 frames at ~2.2e-/Å^2/frame. Sub-frame processing was performed as described previously (74). In brief, individual ~2.2e-/Å^2 frames were globally aligned using Imod scripts (123) then locally aligned using the Optical Flow approach (124) implemented in Xmipp (125). The full dose of ~50e-/Å^2 was used for particle picking and CTF determination in CTFFind3 (126) whereas ~25e-/Å^2 was used in particle processing to center particles and determine their Euler angles.

Cryo-EM Data Processing

Data processing was performed as previously described (74). Briefly, straight kinesin-3 decorated 14pf microtubules were manually boxed in Eman Boxer, serving as input for a set of custom-designed semi-automated single-particle processing scripts utilizing Spider and Frealign as described previously (128) with minor modifications. The final 14pf MT reconstruction was assessed for over-fitting during refinement using a high-resolution noise-substitution test (129) Using local resolution estimates determined with the *blocres* program in Bsoft, the reconstruction was sharpened with a Bfactor of -180 up to a resolution of 5.5Å or 4Å for visualization of kinesin or tubulin densities respectively.

Cryo-EM Model Building and Refinement

α1B/βI+βIVb tubulin was built directly into density in Coot (130) using the recently solved high-resolution cryo-EM model of the brain tubulin 14pf GMPCPP microtubule (PDB 3JAT (131)) as a starting model. After model building, real-space refinement with symmetry restraints was performed in Phenix followed by refinement with symmetry restraints in REFMAC v5.8 modified for cryo-EM data (supplementary Table 1) (132). Secondary structure and reference restraints used with REFMAC based on the high resolution tubulin crystal structure PDB 4DRX (133) were generated with ProSMART (134).

Protofilament number, ring and end-length quantification

Using a FEI Tecnai T12 operating at 120kV and a 4kx4k CCD camera (Gatan Inc.) images of dynamic bovine brain or a1B/bI+bIVb tubulin microtubules were collected. A defocus range of 2-4μm, a total dose of 30e- over a 1 second exposure and low pass/fourier filtering was used to

allow visualization of moiré patterns and thereby assign the MT protofilament and helical start number (168). Ring diameters in these dynamic samples were quantified only for closed single rings using straight line and 'measure' in FIJI (169) from the longest edge-to-edge distance in rings imaged at different projection angles. The axial length of curved end regions in dynamic microtubule preparations were also measured using straight line and 'measure' in FIJI, by drawing a straight line continuing along the microtubule axis from the start of the curved/tapered region to the microtubule extreme end.

EB1-GFP Tip Tracking

Human full-length EB1 fused to a C-terminal GFP-tag was purified using a Ni-affinity purification. The final concentration of EB1 in the experiments was 100nM. Comets were analyzed to give a measurement of the average decay length of the GFP signal on the microtubule. First, ImageJ was used to draw kymographs of growing microtubule tips. These kymographs are then read in by a custom written MATLAB (Mathworks) script that analyzes the peaks. First, the maximum intensity in each line is found and a Gaussian fit to the line profile covering 3 μm of the lattice and going 2 μm beyond the microtubule tip is performed to find the center of the comet. The location of the center is then subtracted from each data point such that the brightest part of the tip is located at zero. These steps were repeated for each line in the kymograph. If a line was not able to be fit with a Gaussian to determine the center, it was skipped. Next, all of the aligned profiles are binned into single pixel size bins (77 nm) and their average values were calculated. These data were then plotted in Prism and a single exponential decay was fit from the first pixel after the peak to the end of the comet tail. The inverse of the fit parameter yielded the mean decay length for each condition.

Results

Purification of Human Unmodified α1B/βI+βIVb Tubulin and Brain Tubulin

We purified tubulin from mouse brain and human embryonic kidney (tsA 201) cell line using a modified TOG-affinity purification method (74, 162) (Materials and Methods) in order to obtain the purity required for reproducible *in vitro* dynamics assays. Mass spectrometric analysis shows that tubulin isolated from this cell line contains predominantly one α- and two β-tubulin isoforms with no detectable post-translational modifications (Figure 1). In order to allow a side-by-side comparison, we also purified tubulin from mouse brain using the same TOG based purification procedure. Mass spectrometric analysis shows its high level of heterogeneity with more than 30 different separate species consisting of varied α- and β-tubulin isoforms and post-translational modifications.

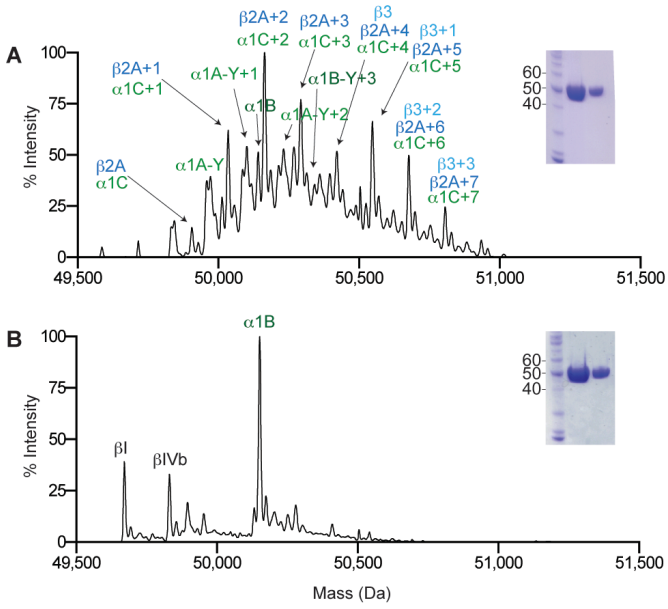

Figure 1: Mass spectra of TOG purified tubulin from brain tissue and tsA201 cells
A) Mass spectra and SDS-polyacrylamide gel (*inset*) of TOG-affinity purified and cycled mouse brain tubulin. B) Mass spectra and SDS-polyacrylamide gel (*inset*) of TOG-affinity purified and cycled tsA201 cell line. The two lanes on the gel are two different amounts of tubulin loaded: 5μgs (left) and 2μgs (right).

In Vitro Dynamics of Human Unmodified α1B/βI+βIVb Tubulin

To examine the dynamics of α1B/βI+βIVb tubulin, we performed label-free *in vitro* dynamic assays using darkfield microscopy (Figure 2). To quantify dynamic parameters, we generated kymographs from time-lapse images of dynamic microtubules (Figure 2A). We find the plus end growth rates for α1B/βI+βIVb microtubules are ~2-fold faster than brain microtubules (Figure 2D). Consistent with this, the plus-end on-rate is 3.7 dimers s^{-1} μM^{-1} compared to 2.0 dimers s^{-1} μM^{-1} for brain tubulin (Figure 2C). The plus-end catastrophe frequency (the transition from growth to shrinkage) is ~2-fold lower than that of brain microtubules (Figure 2D). Earlier studies reported Hela microtubules comprised mainly of βI+βIVb tubulin and an unknown α-tubulin composition, catastrophe less than brain microtubules, in agreement with our observations (68). The minus end growth rates and catastrophe frequencies for α1B/βI+βIVb microtubules are statistically indistinguishable from brain microtubules (Figure 2E). The dynamic parameters observed for α1B/βI+βIVb microtubules are reproducible across multiple preparations purified from different tsA201 cell growths (Figure S1). Thus, unmodified α1B/βI+βIVb microtubules are more stable and reach longer mean lengths than heterogeneous brain microtubules. The 3-fold increase in mean microtubule length from 3.9±0.3 mm to 10.7±0.6 mm for α1B/βI+βIVb microtubules is achieved mainly through a combination of catastrophe suppression and polymerization enhancement (Figure 2D).

Darkfield imaging allows acquisition at high frame rates that enables the determination of depolymerization rates with high accuracy. These measurements show that α1B/βI+βIVb microtubules depolymerize 33% faster than brain microtubules (Figure 2B). Interestingly, the depolymerization rate of α1B/βI+βIVb microtubules is faster than that of α1A/βIII microtubules

(38.9±2.3 μm/min and 30.5±1.3 μm/min for α1B/βI+βIVb and α1A/βIII microtubules, respectively). This indicates that microtubules with different isoform compositions have the potential to generate different end depolymerization forces that could be harnessed to move cargo in the cell, such as chromosomes during cell division (152).

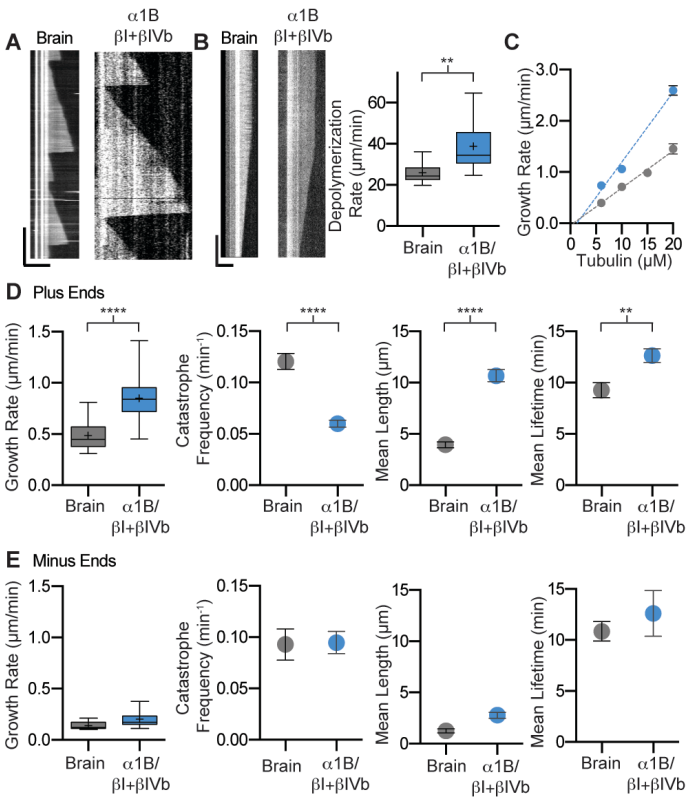

Figure 2: Dynamics of brain and α1B/βI+βIVb microtubules

A) Kymographs showing typical microtubule growth for brain and α1B/βI+βIVb tubulin at 6 μM. *Horizontal* and *vertical scale bars,* 5 μm and 5 min, respectively**.** B) *Left panel*, kymographs showing a typical depolymerization event for brain and α1B/βI+βIVb microtubules. *Horizontal* and *vertical scale bar,* 5 μm and 2 s, respectively. *Right panel*, Tukey plot showing plus-end depolymerization rates at 6 μM tubulin; *n* = 12 and 27 events for brain and α1B/βI+βIVb microtubules, respectively. C) Plus-end growth rates as a function of varying tubulin concentration for brain (gray) and α1B/βI+βIVb microtubules (blue). D) Plus-end dynamics of brain (gray) and α1B/βI+βIVb (blue) microtubules at 6 μM tubulin. *From left to right,* box-whisker plot (whiskers indicate minimum and maximum) showing plus-end growth rates for brain and α1B/βI+βIVb microtubules; n = 38 and 191 events for brain and α1B/βI+βIVb tubulin, respectively. Plus-end catastrophe frequencies; n = 20 and 69 microtubules for brain and α1B/βI+βIVb tubulin, respectively. Plus-end microtubule mean lengths; n = 49 and 102 events for brain and α1B/βI+βIVb tubulin, respectively. Plus-end microtubule mean lifetimes; n = 49 and 102 events for brain and α1B/βI+βIVb tubulin, respectively. E) Minus-end dynamics of brain and for brain and α1B/βI+βIVb tubulin at 6 μM tubulin. *From left to right,* box-whisker plot (whiskers indicate minimum and maximum) showing minus-end growth rates for brain and α1B/βI+βIVb tubulin; n = 12 and 84 events for brain and α1B/βI+βIVb tubulin, respectively. Minus-end catastrophe frequencies; n = 10 and 33 microtubules for brain and α1B/βI+βIVb tubulin, respectively. Minus-end microtubule mean lengths; n = 9 and 10 events for brain and α1B/βI+βIVb, respectively. Minus-end microtubule mean lifetimes; n = 9 and 10 events for brain and α1B/βI+βIVb, respectively. **, *** and ****, *p*-values <0.01, < 0.001 and < 0.0001, respectively determined by unpaired *t*-test.

4.2 Å Cryo-EM Structure of Unmodified α1B/βI+βIVb Microtubules

To gain insight into its assembly properties we determined the structure of α1B/βI+βIVb microtubules in the presence of the non-hydrolyzable GTP-analog, GMPCPP, using cryo-electron microscopy and single-particle reconstruction (Figure 3A). The overall resolution of the reconstruction is ~4.2Å (Figure S2A, gold-standard noise-substitution test; Fourier shell correlation 0.143 criterion (129)); however, assessment of local resolution suggests that much of the tubulin falls within a higher resolution range (~3.5Å in more buried regions to ~4.5Å in the most surface exposed regions; Figure S2). At this resolution the pitch of helices, b-strand separation and side chain densities were apparent and occupancy of nucleotide triphosphate could be seen at both the E-site and N-site in βI+βIVb and α1B-tubulin, respectively (Figures 3A and 3B). The structures of microtubules formed from α1B/βI+βIVb and brain tubulin (previously determined, PDB, 3JAT) are similar. No significant differences were detected at either lateral or longitudinal interfaces between tubulin dimers at this resolution. The dimer repeat distance in GMPCPP α1B/βI+βIVb microtubules (83.4Å±0.1Å) was only slightly longer than that in GMPCPP brain microtubules (83.1±0.0Å), consistent with the presence of an 'extended' lattice in microtubules polymerized from this nucleotide analogue (131, 146). Despite only one isoform being present for a-tubulin and two for b-tubulin, with no discernable post-translational modifications (Figure 1) the C-terminal tails and acetylation loop are unresolved in our reconstruction presumably due to the flexibility of these regions in the absence of effectors as also seen in previous reconstructions of both heterogenous brain microtubules and single-isoform recombinant microtubules (74, 131, 144).

Dynamic microtubules polymerized in standard BRB80 with GTP showed similar protofilament distributions for both brain and α1B/βI+βIVb microtubules, with ~67% containing

14 and ~33% 13 protofilaments (Figures S2C and S2D). The ends of dynamic growing microtubules transition from the straight lattice characteristic of the stable polymer to a curved and tapered region where protofilaments are missing (150, 170). This feature was clear in micrographs of both polymerizing brain and α1B/βI+βIVb tubulin (Figure 3C). The length of the tapered region in dynamic α1B/βI+βIVb and brain microtubules was measured. A wide distribution from very short (<10nm) to rare, but very long (>100nm) end regions was found for both (Fig. 3D). Although the distributions show a large degree of overlap, α1B/βI+βIVb microtubule tapered ends were significantly shorter than those of brain microtubules (Figure 3D; 30.3±3.3nm vs 54.4±7.2nm for a1B/bI+bIVb and brain, respectively). In addition, the variance of the tapered ends lengths was lower within the α1B/βI+βIVb sample than the brain tubulin sample with the frequency distribution of α1B/βI+βIVb microtubules more skewed towards shorter microtubule ends and that of brain microtubules towards longer microtubule ends (Figure 3E). Previous studies proposed that tapered microtubule tips are more likely to catastrophe than blunt microtubule tips (171). Therefore, it is possible that the longer tapered tips for brain microtubules cause the higher catastrophe frequency observed when compared to α1B/βI+βIVb microtubules. The less tapered end architecture of the α1B/βI+βIVb microtubules can also reflect a higher probability of successful incorporation of the more homogenous α1B/βI+βIVb dimers in the microtubule lattice compared to brain tubulin where the highly heterogenous mixture of the dimers can lead to defects in the lattice and the pause in growth of some protofilaments, thus the more extreme tapered structures.

In dynamic microtubule preparations viewed by cryo-EM a proportion of tubulin 'peeling' from depolymerizing microtubule ends closes into rings containing longitudinally associated and curved tubulin dimers (150). We observed tubulin rings in micrographs of both

dynamic α1B/βI+βIVb and brain tubulin preparations (Figure 3F). Even though shapes, sizes and orientations of rings in 2D cryo-EM images projections vary, the longest wall-to-wall distance in the rings provides a measure of overall protofilament curvature. Thus, ring diameters for both sets of dynamic microtubules were measured with α1B/βI+βIVb rings being significantly larger on average (41.0±0.2nm) than brain tubulin rings (37.3±0.5nm) (Figure 3G). Thus, the average tubulin curvature per dimer length (8.2nm) of α1B/βI+βIVb is 22.8° compared to 25.1° for brain tubulin (Figure 3G). Tubulin dimers need to straighten upon incorporation into the microtubule lattice (47, 172, 173). Our data suggests that the energy penalty for straightening the α1B/βI+βIVb dimers during microtubule incorporation is lower, consistent with the higher polymerization rate of these microtubules.

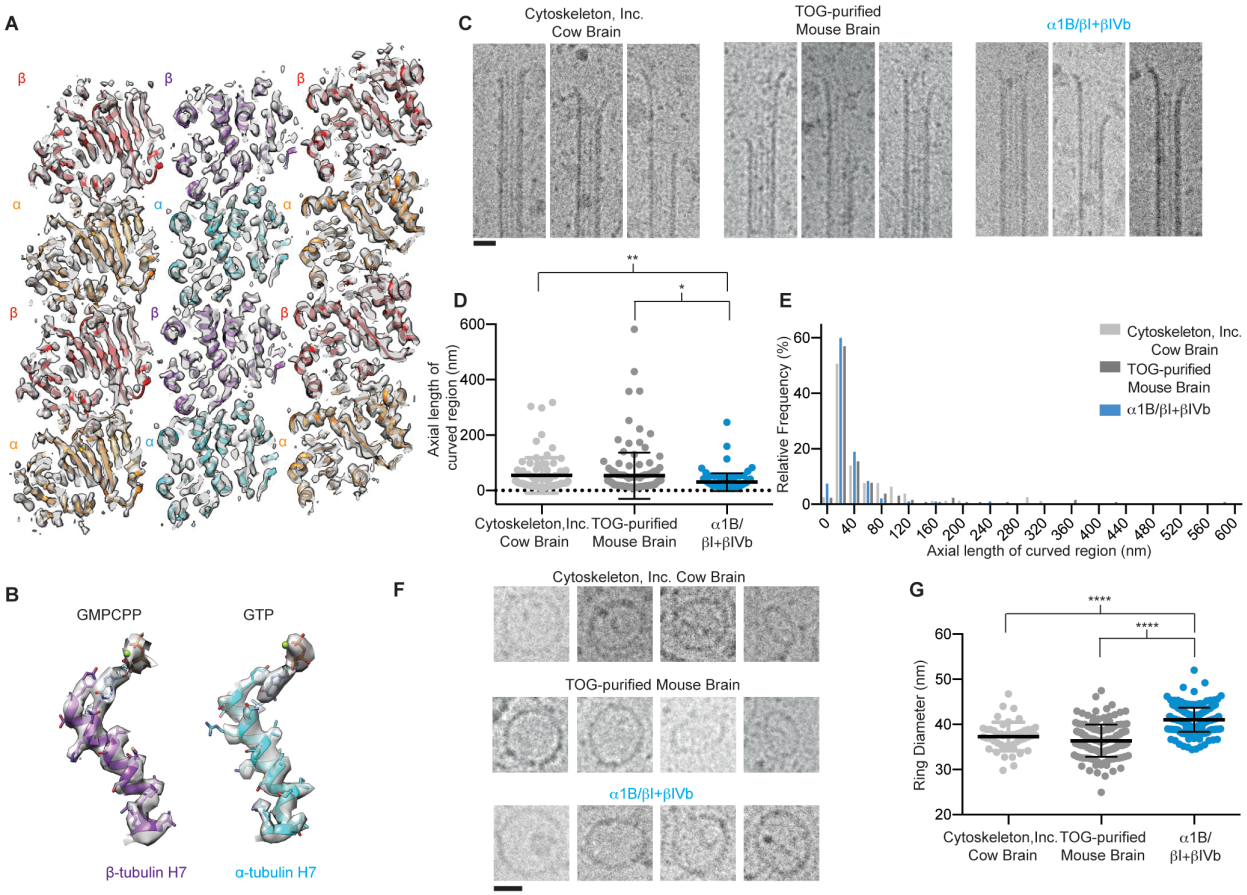

Figure 3: Cryo-electron microscopy of α1B/βI+βIVb microtubules

A) A cross section of the cryo-EM map (gray density) and model of GMPCPP human α1B/βI+βIVb microtubules (three protofilaments shown). A central protofilament (Pf2) makes lateral contacts with adjacent protofilaments (Pf1 and Pf3); α-tubulin, orange, β-tubulin, red (Pf1, Pf3); α-tubulin, cyan; β-tubulin, purple (Pf2). B) β-tubulin helix H7 and GMPCPP (left, purple) and α-tubulin helix H7 and GTP (right, cyan) and their corresponding experimental densities (gray density). C) Gallery of polymerizing brain and α1B/βI+βIVb microtubule ends. Similar architectures are observed, including short and long taper/curved region lengths. (D) Quantification of the length of the curved/tapered region for bovine and mouse brain and α1B/βI+βIVb microtubule ends. * and ** *p*-values <0.05 and < 0.01, respectively determined by Mann-Whitney test.E) Histogram showing curved/tapered region length frequency of α1B/βI+βIVb microtubule ends. F) Gallery of tubulin rings in dynamic preparations of brain (top) and α1B/βI+βIVb microtubules (bottom) showing rings of different diameters and orientations. G) Quantification of maximum ring diameter from brain and α1B/βI+βIVb dynamic microtubule preparations. p-values < 0.0001 respectively determined by Mann-Whitney test

Figure 3 contributed by Dr. Joseph Atherton & Dr. Carolyn Moores

The Lengths of EB1 Comets Are the Same on α1B/βI+βIVb and Brain Microtubules

Polymerizing microtubules are protected from depolymerization by a GTP-cap at the end of growing microtubules generated by a lag between the GTP hydrolysis rate of tubulin in the microtubule lattice and microtubule elongation. Once the stabilizing cap is "lost", the microtubule transitions from growth to shrinkage (18, 46). Because of α1B/βI+βIVb microtubules catastrophe less than brain microtubules, we hypothesized that there might be a difference in the stabilizing GTP cap size between growing α1B/βI+βIVb and brain microtubules. The EB1 family of proteins is thought to preferentially bind to the growing microtubule end by sensing the GTP (or GDP-Pi) in the cap structure (174-176). Therefore, the size of the EB1 binding region can be used as a read-out of the GTP cap size (174). We measured EB1-GFP comet lengths at different growth speeds for brain and α1B/βI+βIVb microtubules (Figure 4). The EB1-GFP comet length increases with increasing microtubule growth speeds for brain tubulin as expected based on earlier studies (174). This was also observed for α1B/βI+βIVb microtubules (Figures 4A and 4B). Interestingly, when brain and α1B/βI+βIVb microtubules are compared at the same growth speeds, the EB1-GFP comet lengths are statistically indistinguishable (Figure 4C), suggesting that there is no significant difference in the GTP cap size between brain and α1B/βI+βIVb microtubules. These results indicate that the lower catastrophe frequency and faster growth rates of the α1B/βI+βIVb microtubules are due mostly to the large differences between the tubulin on-rates. We cannot rule out a small difference in GTPase rates not detectable in these assays.

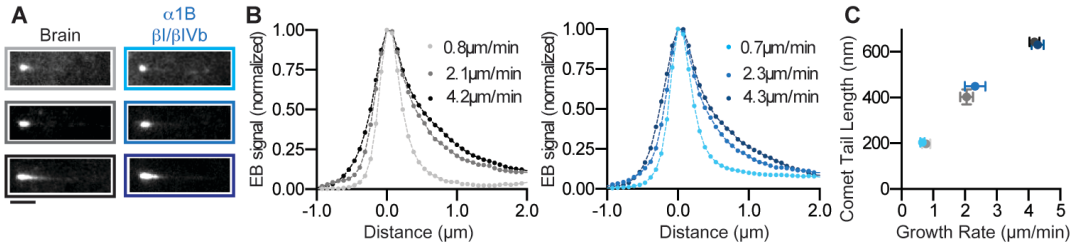

Figure 4: EB1-GFP comet analysis on brain and α1B/βI+βIVb microtubules
A) TIRF microscopy images of EB1-GFP comets at the ends of growing brain microtubules (left) and α1B/βI+βIVb (right) microtubules at different growth speeds. *From top to bottom,* brain microtubule growth speeds are 0.8μm/min, 2.1μm/min and 4.2μm/min. *From top to bottom* α1B/βI+βIVb microtubule growth speeds are 0.7μm/min, 2.3μm/min and 4.3μm/min. *Scale bar*, 2μm. B) Averaged fluorescence intensity profiles of EB1-GFP comets at different growth speeds of brain microtubules (left) and α1B/βI+βIVb (right). C) EB1-GFP comet tail lengths as a function of microtubule growth speeds for brain (gray) and α1B/βI+βIVb (blue) microtubules. Comet tail lengths were obtained by single exponential fits to the averaged intensity profiles (Materials and Methods).

Figure 4 data analysis software was written by Dr. Jeffrey Spector and performed image analysis with my assistance.

Modulation of α1B/βI+βIVb Tubulin Dynamics by a Neuronal Isoform

βIII, a neuronal specific tubulin isoform, is overexpressed in various tumors and has been identified as a strong prognosticator of poor clinical outcomes (140). Its mRNA levels can increase as much as 43- and 71-fold in breast and lung cancers, respectively when compared to mRNA levels in non-tumoral tissues (117). bIII constitutes 25% of tubulin purified from brain tissue (58), but is not found in any non-neuronal tissue except upon transformation (117). In order to understand the effects of neuronal tubulin on microtubule dynamics in non-neuronal cells, we characterized the dynamic parameters of α1B/βI+βIVb tubulin in the presence of increasing amounts of neuronal α1A/βIII tubulin (Figure 5). We expressed and purified recombinant α1A/βIII tubulin through a double-selection strategy using an affinity-tag on both a- and b-tubulin. This tubulin is >99.9% homogenous, modification-free and free of contamination from endogenous insect tubulins and assembly-competent (74). We titrated recombinant neuronal α1A/βIII tubulin into non-neuronal α1B/βI+βIVb tubulin and measured microtubule dynamics parameters. These show that microtubule dynamic parameters can be tuned by the proportion between these two types of tubulins. Equimolar amounts of non-neuronal α1B/βI+βIVb and neuronal α1A/βIII results in plus-end growth rates comparable to those of α1A/βIII tubulin alone (Figure 5A) while plus-end catastrophe frequencies are similar to those of neuronal α1A/βIII only when 3-fold molar excess of α1A/βIII tubulin is added. α1A/βIII tubulin does not polymerize on its own at the concentrations used. We do not detect any statistical significant differences in minus-end dynamics. Therefore, the intrinsic microtubule dynamic properties can be tuned by the titration of different tubulin isoforms. Moreover, these experiments indicate that the over-expression of the α1A/βIII tubulin in tumors can significantly alter global microtubule dynamics, with the differences observed being comparable to those

elicited by microtubule associated proteins such as XMAP215 (116) or MCAK (177). A destabilizing effect of neuronal βIII tubulin was also observed recently when mixed with recombinant βII tubulin in the presence of an unknown a-tubulin composition that included insect α-tubulin (178) as well as in earlier experiments with brain microtubules depleted of βIII tubulin by immunoaffinity chromatography (120).

In conclusion, the majority of *in vitro* dynamics studies performed use heterogenous scrambled brain microtubules with isoform composition and post-translational modifications that are not representative of the many cell types found in our bodies as well as the majority of cell lines used for cell biological investigations. Recent work using *S. cerevisiae* tubulin showed strikingly different activities of the tip tracking protein Stu2p when compared to heterogeneous brain microtubules (153), indicating the importance of studying the effects of regulators with the physiologically relevant tubulin substrate.

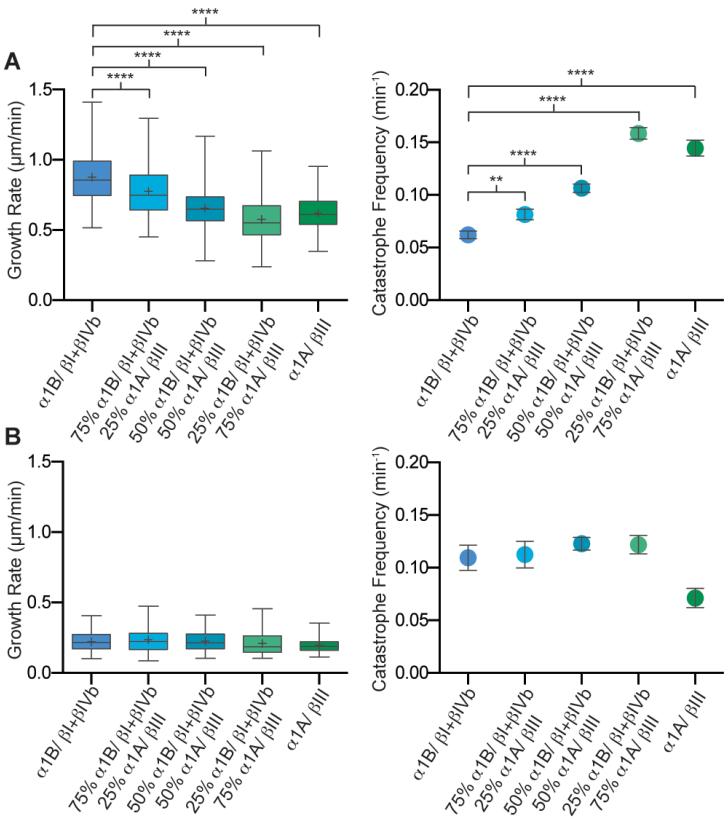

Figure 5: Modulation of α1B/βI+βIVb tubulin dynamics by addition of α1A/βIII tubulin
A) *Left panel*, box-whisker plot (whiskers indicate minimum and maximum) showing plus-end growth rates at 6μM tubulin; n = 191, 258, 432, 377 and 203 events for α1B/βI+βIVb, 75% α1B/βI+βIVb 25% α1A/βIII, 50% α1B/βI+βIVb 50% α1A/βIII, 25% α1B/βI+βIVb 75% α1A/βIII and α1A/βIII tubulin, respectively. *Right panel*, plus-end catastrophe frequencies; n = 69, 77, 113, 94 and 85 microtubules for α1B/βI+βIVb, 75% α1B/βI+βIVb 25% α1A/βIII, 50% α1B/βI+βIVb 50% α1A/βIII, 25% α1B/βI+βIVb 75% α1A/βIII and α1A/βIII tubulin, respectively. B) *Left panel*, box-whisker plot (whiskers indicate minimum and maximum) showing minus-end growth rates at 6μM tubulin; n = 84, 66, 206, 91 and 93 events for α1B/βI+βIVb, 75% α1B/βI+βIVb 25% α1A/βIII, 50% α1B/βI+βIVb 50% α1A/βIII, 25% α1B/βI+βIVb 75% α1A/βIII and α1A/βIII tubulin, respectively. *Right panel*, minus-end catastrophe frequencies; n = 33, 34, 59, 30 and 40 microtubules for α1B/βI+βIVb, 75% α1B/βI+βIVb 25% α1A/βIII, 50% α1B/βI+βIVb 50% α1A/βIII, 25% α1B/βI+βIVb 75% α1A/βIII and α1A/βIII tubulin, respectively.

Discussion

Here, we present for the first time the cryo-EM structure and *in vitro* dynamics parameters for unmodified α1B/βI+βIVb tubulin purified from a human embryonic kidney cell line. We show that α1B/βI+βIVb microtubules have dramatically different dynamic parameters than those of brain microtubules characterized by faster growth rates and lower catastrophe frequencies. These differences are comparable in magnitude to those elicited by microtubule associated proteins (116, 177). Moreover, we discovered that the faster growing α1B/βI+βIVb microtubules have less tapered microtubule tip structures that could explain the faster growth rates and lower catastrophe frequencies that we measure for these microtubules. Furthermore, we demonstrate that the dynamics of non-neuronal α1B/βI+βIVb microtubules can be modulated by the addition of a neuronal tubulin isoform that has slower growth rates and higher catastrophe frequencies. Thus, in addition to the potential isoform specific recruitment of microtubule regulators, different microtubule dynamics microtubules in cells can be elicited by modulating the relative expression levels of tubulin isoforms.

Experimental Contributions:

I purified the TOG-affinity based tubulin. Dr. Agnieszka Szyk purified the recombinant tubulin and I assisted with the purification. Both Dr. Jeffrey Spector and I performed the *in vitro* microtubule dynamics and analyzed the dynamics data. Dr. Joseph Atherton from Dr. Carolyn Moores' lab determined the EM structure. Any figures I did not contribute, I have highlighted throughout this chapter.

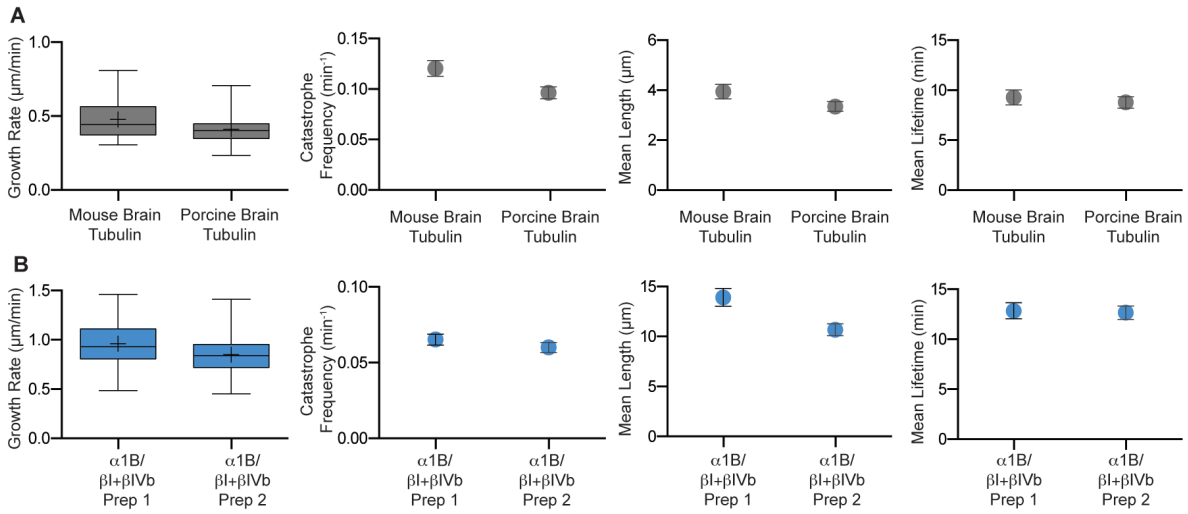

Supplementary Figure 1: Consistent dynamic parameters for α1B/βI+βIVb and brain tubulin from different purifications.

A) Consistent dynamic parameters for α1B/βI+βIVb tubulin from different purifications. *From left to right:* Box-whisker plot (whiskers indicate minimum and maximum) showing plus-end growth rates at 6μM tubulin from two different tubulin preparations; n = 246 and 191 events for purification 1 and purification 2, respectively. Plus-end catastrophe frequencies; n = 90 and 69 microtubules. Plus-end microtubule lengths; n = 74 and 102 events. Plus-end microtubule lifetimes; n = 74 and 102 events for purification 1 and purification 2, respectively. B). Dynamic parameters of mouse brain tubulin purified *via* the TOG affinity approach and commercial brain tubulin (Cytoskeleton Inc.). *From left to right:* Box-whisker plot (whiskers indicate minimum and maximum) showing plus-end growth rates at 6μM tubulin from the two different tubulin preparations; n = 38 and 101 events for mouse brain tubulin and commercial porcine tubulin, respectively. Plus-end catastrophe frequencies; n = 20 and 32 microtubules. Plus-end microtubule lengths; n = 49 and 76 events. Plus-end microtubule lifetimes; n = 49 and 76 events for mouse brain tubulin and commercial porcine tubulin, respectively.

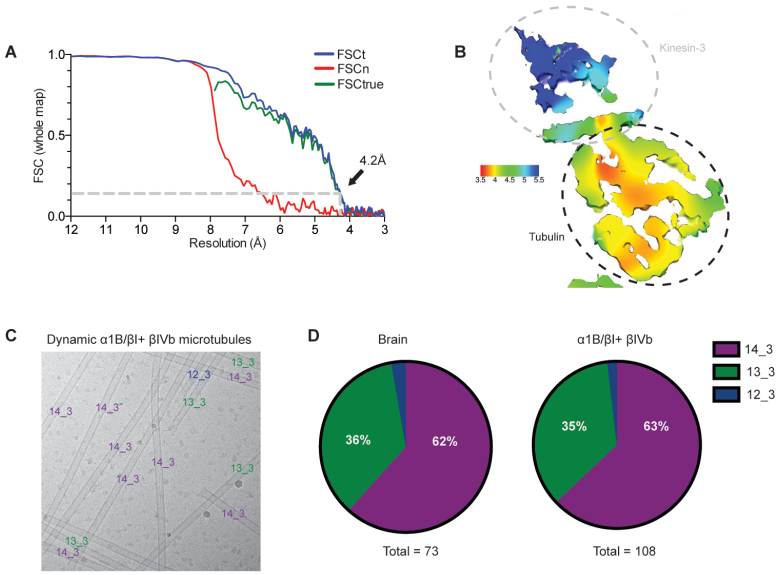

Supplementary Figure 2: Resolution estimates and protofilament number analysis of α1B/βI+βIVb microtubules.

A) Utilizing the gold-standard noise substitution method (129) the FSCtrue curve gives an overall resolution estimate of 4.2Å for the reconstruction α1B/βI+βIVb GMPCPP microtubules bound to kinesin-3. B) Using the Bsoft program blocres (147) local resolution estimates were calculated and used to color the unfiltered whole reconstruction density. Red density corresponds to 3.5 Å resolution, with a continuum of colors indicating the resolution gradient, ending with blue at 5.5 Å resolution. Tubulin is at a higher resolution, ranging from ~3.5 Å in central regions to ~4.5 Å in more flexible peripheral surface-exposed regions. Kinesin-3, used as a fiducial marker for alignment purposes, is at lower resolution (resolution of ~5.5 Å) and is excluded from display items. C) Raw image of dynamic α1B/βI+βIVb microtubules. Microtubules are individually labeled with their protofilament number (from 12-14) and start number (3) according to analysis of their Moire patterns (179). D) Quantification of protofilament number distributions for dynamic brain or α1B/βI+βIVb microtubules polymerized under identical conditions.

Supplementary Figure 2 contributed by Dr. Joseph Atherton & Dr. Carolyn Moores

CHAPTER 4: Severing enzymes amplify microtubule arrays through GTP-tubulin incorporation

This chapter is re-produced from:
Vemu, A.*, Szczesna E.*, Zehr, E.A., Spector, J.O., Grigorieff, N., Deaconescu, A.M., and Roll-Mecak, A. (2018) Severing enzymes amplify microtubule arrays through GTP-tubulin incorporation. *Science*.
*contributed equally

Abstract

Spastin and katanin sever and destabilize microtubules. Paradoxically, despite their destructive activity they increase microtubule mass in vivo. Here we combine single-molecule fluorescence total internal reflection and electron microscopy to show that the elemental step in microtubule-severing was the generation of nanoscale damage throughout the microtubule by active extraction of tubulin heterodimers. These damage sites were repaired spontaneously by GTP-tubulin incorporation rejuvenating and stabilizing the microtubule shaft. Consequently, spastin and katanin increased microtubule rescue rates. Furthermore, newly severed ends emerged with a high-density of GTP-tubulin that protected them against depolymerization. The stabilization of the newly severed plus-ends and the higher rescue frequency synergized to amplify microtubule number and mass. Thus, severing enzymes regulate microtubule architecture and dynamics by promoting GTP-tubulin incorporation within the microtubule shaft.

Introduction

The plasticity of the microtubule cytoskeleton follows from multiple levels of regulation through microtubule-end polymerization and depolymerization, crosslinking, and microtubule severing. Microtubule severing generates internal breaks in microtubules. It is mediated by three enzymes of the AAA (ATPases associated with various cellular activities) ATPase family – katanin, spastin and fidgetin (reviewed in *(80)*) that are widely conserved in animals and plants. They are critical for the generation and maintenance of complex non-centrosomal microtubule arrays in neurons (107, 180-182) and the plant cortex (103, 183, 184), and regulate meiotic and mitotic spindle morphology and length (93, 98, 185, 186), cilia biogenesis (83, 187), centriole duplication (83, 84), cytokinesis (188, 189) , axonal growth (190), wound healing (191) and plant phototropism (103, 184) . Both spastin and katanin are associated with debilitating diseases. Spastin is mutated in hereditary spastic paraplegias, neurodegenerative disorders characterized by lower extremity weakness due to axonopathy (reviewed in *(192)*). Katanin mutations cause microcephaly, seizures and severe developmental defects (83, 84, 193). Disease mutations impair microtubule severing (89, 92).

Paradoxically, in many of these systems, the loss of the microtubule-severing enzyme leads to a decrease in microtubule mass (reviewed in *(192)*). Spastin loss causes sparse disorganized microtubule arrays at *Drosophila* synaptic boutons (107) , and impaired axonal outgrowth and sparse microtubule arrays in zebrafish axons (108) . Similarly, katanin loss leads to sparse cortical microtubule arrays in *Arabidopsis* (103, 194), while in *C. elegans* meiotic spindles it results in loss of microtubule mass and number (104). It was hypothesized that the increase in microtubule number and mass results from templated nucleation from the severed ends *(105, 106)*. This is an attractive mechanism for rapidly generating microtubule mass,

especially in the absence of centrosome-based nucleation as in neurons or meiotic spindles. This severing-dependent microtubule amplification has been directly observed in plant cortical microtubule arrays (103). However, for this amplification to operate, the GDP-tubulin lattice exposed through severing would have to be stabilized because GDP-microtubules depolymerize spontaneously in the absence of a stabilizing GTP-cap (18, 45, 109, 110). We wanted to study this paradox and combined time-resolved transmission electron microscopy (TEM) and total internal reflection fluorescence (TIRF) microscopy to study the effects of severing enzymes spastin and katanin on microtubule structure and dynamics in vitro.

Material and Methods

Protein expression and purification

Drosophila melanogaster full-length spastin was purified by affinity chromatography and ion exchange as previously described (195). *Caenorhabditis elegans* His-tagged katanin Mei1/Mei2 (93) was purified by Ni-affinity chromatography. The affinity tag was removed by Tobacco Etch Virus protease and the protein was further purified on an ion exchange MonoS column (GE Healthcare) as previously described (87). Peak fractions were concentrated, buffer exchanged into 20 mM Hepes 7.0, 300 mM KCl, 10 mM $MgCl_2$ and 1 mM TCEP and flash frozen in small aliquots in liquid nitrogen. *Homo sapiens* EB1-GFP was expressed and purified as previously described *(196)*. Human α1Aβ III tubulin with an engineered FLAG-tag at the β-tubulin C-terminus was expressed using baculovirus and purified as described previously (74).

Transmission electron microscopy of microtubule severing reactions

Taxol-stabilized GDP microtubules were prepared by polymerizing 10 µl of 100 µM glycerol-free porcine tubulin (Cytoskeleton Inc., Denver, CO) in 80 mM K-PIPES pH 6.8, 1 mM $MgCl_2$, 1 mM EGTA, 10 % DMSO, 1 mM GTP for 1 hour in 37 °C water bath. Taxol was added to 20 µM final concentration and the reaction was incubated on the bench top for 1-2 hours. Microtubules were loaded on 60 % glycerol cushion (BRB80, 60 % (v/v) glycerol and 20 µM taxol) at 37 °C using a pipette tip with the tip cut off. Non-polymerized tubulin was removed by centrifugation in a TLA100 rotor at 35,000 rpm for 15 min at 37 °C. The pellet was gently re-suspended to 2.5 µM of tubulin in BRB80, supplemented with 20 µM taxol and 1mM GTP at 37 °C using a pipette tip with the tip cut off.

For GDP microtubules, all polymerization and severing reactions were performed at 37 °C. 20 µl of 100 µM glycerol-free porcine tubulin (Cytoskeleton Inc.) was polymerized in 10 %

DMSO, 1 mM GTP and 10 mM $MgCl_2$ for 1 hour at 37 °C water bath. The microtubules were passed through 60 % glycerol cushion (BRB80, 60 % (v/v) glycerol and 1mM GTP) using a TLA100 rotor at 35,000 rpm for 15 min to remove non-polymerized tubulin. The pellet was washed twice using 50 µl buffer (BRB80, 10 % DMSO, 1 mM GTP) and gently re-suspended to 30 µM in the same buffer using a pipette tip with the tip cut off.

GMPCPP microtubules were prepared by polymerizing 20 µl of 100 µM glycerol-free porcine tubulin (Cytoskeleton Inc.) in 1mM GMPCPP in BRB80 (80 mM PIPES-KOH pH6.8, 1mM $MgCl_2$, 1mM EGTA, 1mM DTT) on ice for 5 min and then in a water bath at 37 °C for 1 hour. Non-polymerized tubulin was removed by centrifugation in a TLA100 rotor at 126,000 x g for 5 min at 37 °C. The pellet was washed twice with 50 µl of BRB80 at 37 °C and re-suspended in 50 µl of ice-cold BRB80. The reaction was kept on ice for 30 min and periodically mixed up and down to fully depolymerize microtubules. GMPCPP was added to 1 mM and the polymerization reaction was transferred to 37 °C for 2-4 hrs or overnight. Non-polymerized tubulin was removed by centrifugation and washed as described above. The microtubule pellet was gently re-suspended to 2.5 µM of tubulin in BRB80 using a pipette tip with the tip cut off.

We found that performing severing reactions in the tube followed by pipetting onto electron microscopy grids resulted in microtubule breakage. We therefore first carried out severing reactions on the electron microscopy grid. Briefly, 2ml microtubule solution (at 1 to 3 µM) in BRB80 (80mM PIPES pH 6.8, 1 mM MgCl2, 1 mM EGTA) was applied to a glow-discharged Cu grid, followed by pipetting of 2µl ATP solution (10mM ATP in BRB80 supplemented with 20mM taxol, for taxol stabilized microtubules) and 2µl spastin (at 100 nM). The reaction was allowed to proceed on grid for one minute or as specified, after which the liquid was wicked off with calcium-free filter paper, and the grid was stained with 0.75% (w/v)

uranyl formate, and air-dried. Images were collected on a FEI Morgagni 286 electron microscope operated at 80kV and equipped with AMT lens-coupled 1k x 1k CCD camera. For the solution severing reaction time courses, 20 µl of GMPCPP or taxol-stabilized microtubules in BRB80 buffer at 2.5 mM or 0.5mM were applied to parafilm followed by addition of 20 µl of 50 nM spastin or 200 nM katanin in 20 mM HEPES pH 7.5, 300 mM KCl, 10 mM $MgCl_2$, 1mM TCEP and 1mM ATP to a final concentration of 25 nM spastin and 100 nM for katanin. For the solution severing reaction time courses of non-stabilized GDP microtubules, 20 µl of 30 mM GDP microtubules in the presence of 10% DMSO were incubated with 2 µl of 20 nM katanin. Buffer without severing enzymes was added to microtubules as a negative control. The severing reactions were incubated for 30 sec, 2 or 5 mins and carbon-coated grids (Carbon Film only on 400 mesh, Ted Pella, Inc.) were dipped in the reactions. Excess liquid was blotted using filter paper. Grids were washed three times with 40 µl BRB80, stained with 0.75 % (w/v) uranyl formate and air-dried. Images were collected on a T12 Technai electron microscope (FEI) equipped with a 2k x2k Gatan US1000 CCD camera. Images were collected at nominal magnifications of 550x, 13,000x or 30,000x corresponding to pixel sizes of 84 Å/pix, 3.55 Å/pix, or 1.54 Å/pix, respectively.

TIRF based assays of tubulin incorporation into stabilized microtubules damaged by spastin and katanin

Double-cycled, GMPCPP-stabilized microtubules (151) were polymerized from 2 mg/ml porcine brain tubulin (Cytoskeleton). First polymerization was 1 h, the second polymerization step was at least 4 h to obtain long microtubules. Then microtubules were centrifuged, resuspended in warm BRB80 (80 mM K-PIPES pH 6.8, 1 mM $MgCl_2$, 1 mM EGTA) and stored at 37°C or RT and used within a day. The same results were obtained regardless of whether the storage temperature

was 37°C or RT. Taxol-stabilized microtubules (195) were polymerized from 5 mg/ml porcine brain tubulin containing 1% biotinylated and 20% HiLyte647-labeled tubulin (Cytoskeleton) in BRB80 with 10% DMSO, 0.5 mM GTP and 10 mM $MgCl_2$. After 1 h incubation at 37°C, 20 μM Taxol was added and the mixture was further incubated ON. Microtubules were then centrifuged through a 60% glycerol cushion for 12 min at 109,000 g, 35°C. The microtubule pellet was washed with warm BRB80 supplemented with 14.3 mM 2-mercaptoethanol and 20 μM Taxol, and resuspended gently in the same buffer.

Chambers for TIRF microscopy were assembled as previously described (195). Double-cycled GMPCPP microtubules containing 1% biotinylated tubulin and 20% HiLyte647-labeled tubulin (or unlabeled tubulin for the DIC assays) assembled as above were immobilized in the chamber with 2 mg/ml Neutravidin (Thermo Fisher Scientific) and imaged by TIRF or DIC microscopy in severing buffer (BRB80 buffer with 2 mg/ml casein, 14.3 mM 2-mercaptoethanol, 2.5% glycerol, 50 mM KCl, 2.5 mM $MgCl_2$, 1 mM ATP, 1% Pluronic F127 (Life Technologies) and oxygen scavengers). To introduce and detect nanoscale damage in microtubules (Fig. 2), immobilized microtubules were then incubated with 10 nM spastin or 2 nM katanin in severing buffer for 35 s or 90 s respectively. Microtubules in control experiments were incubated without severing enzyme. The enzyme mixture was then replaced with 1 μM HiLyte488-labeled tubulin (Cytoskeleton), 1 mM ADP, 0.5 mM GTP, 1% F127 Pluronic, 2.5 mg/ml casein in BRB80 and left to incubate for 5 min. The tubulin containing solution was then washed out with 45 μl of BRB80 supplemented with oxygen scavengers, 1.5 mg/ml casein, 10 mM 2-mercaptoethanol and 1% F127 Pluronic. Microtubules and HiLyte488-labeled tubulin were imaged by TIRF. Multiple fields of view were imaged. The same assay was performed for taxol-stabilized microtubules, but in this case the repair step was performed with 0.1 mM soluble tubulin to prevent microtubule

nucleation in the presence of taxol. For time course experiments, the same protocol was used except that microtubules were incubated with 2 nM spastin (fig. S3) or 2 nM katanin (fig. S4) for 35-120 sec. Control microtubules were incubated without severing enzyme for 120 sec. 1 μM HiLyte488-labeled tubulin was used for the repair step. For repair with 1 μM recombinant human tubulin (fig. S6), nanodamaged microtubules were incubated for 5 min with recombinant tubulin. Unincorporated tubulin was washed away and tubulin incorporated into microtubules was detected by anti-FLAG M2 antibodies (Sigma Aldrich, diluted 1:500) and goat anti-mouse antibodies conjugated with Alexa Fluor 488 (Invitrogen, diluted 1:1000). All assays were performed at room temperature. Details regarding image acquisition and analysis are described in the subsection below.

Image acquisition and analysis of tubulin incorporation in GMPCPP- and taxol-stabilized microtubules by TIRF microscopy

Images were acquired using a Nikon Ti-E microscope equipped with a 100x 1.49 NA oil objective and a TI-TIRF adapter (Nikon). The 488 excitation laser (Coherent Inc.) was set at 20 mW and the 647 nm laser (Coherent Inc) was set to 2 mW before being coupled into the Ti-TIRF optical fiber (Nikon). Two-color simultaneous imaging was performed using a TuCAM (Andor) device that splits the emission on to two separate EMCCD cameras (Andor iXon 897). The excitation and emission were split by a quad band dichroic (Semrock) and the emission was further split by an FF640 filter (Semrock) and further filtered with a FF01-550/88 (Semrock) for the 488 channel and a FF01-642/LP (Semrock) for the 640 channel. The Tucam imaging system introduces an extra 2X magnification yielding a final pixel size of 77 nm. The images from the two cameras were aligned by first imaging a grid of spots (Nanogrid MiralomaTech) on each camera and using the GridAligner plug-in for ImageJ.

DIC illumination was provided by a SOLA-SE-II (Lumencor) coupled to the microscope by a liquid light guide. A standard set of polarizer and analyzer (Nikon 100 X-II High NA/Oil) prisms were used and the image was captured on a CoolSNAP (Photometrics) camera. The final pixel size for DIC images was 65 nm. Raw DIC images were processed using an FFT bandpass filter. DIC images were scaled and transformed to overlay with fluorescent images by imaging fluorescent microtubules in both channels for image registration. The entire imaging setup was controlled by Micro-Manager (197).

For data shown in figs. S3 and S4, images were analyzed using scripts in ImageJ and MATLAB. First, the offset between 640 and 488 channels was corrected with the GridAligner plugin. Then microtubules were selected with 7 px-wide line selection and line scans were generated. These line scans were imported into a MATLAB script that identified the peaks in the 488 channel and recorded the number, intensity and full-width-at-half-maximum (FWHM) of the repair sites. The FWHM for a diffraction-limited spot was obtained using 100 nm TetraSpeck beads (Thermo Fischer Scientific). Data were exported to PRISM software for graphing.

Transmission electron microscopy of microtubules repaired with recombinant tubulin

GMPCPP microtubules at 1 μM concentration in 1x BRB80 were applied to parafilm in a humidity chamber and incubated with 20 nM spastin in microtubule-severing buffer (20 mM HEPES pH 7.5, 300 mM KCl, 10 mM $MgCl_2$, 1 mM TCEP and 0.5 mM ATP). Buffer containing 0.5 mM ATPγS instead of ATP was used as a control. Severing was allowed to proceed for 30 seconds followed by addition of 0.6 μM soluble FLAG-tagged single-isoform recombinant neuronal human a1AbIII tubulin to repair the microtubule lattice in the presence of 1 mM GTP and 5mM ADP to inactivate the enzyme. The repair reaction was carried out for 5 min. Microtubules were then stabilized by the addition of 5 volumes of 0.2% glutaraldehyde in

1xBRB80 (80mM PIPES, 1mM $MgCl_2$, 1mM EGTA). After 3 minutes, crosslinking was quenched by the addition of Tris-HCl pH 7.5 to 20 mM final concentration and crosslinked microtubules were transferred into a 10 ml centrifuge tube (Beckman Coulter). The microtubule severing and healing procedure was repeated three more times, reactions were pooled into the same centrifuge tube and microtubules were then spun down in a MLA-80 rotor at 100,000 x g for 15 min at 30 °C. The microtubule pellet was gently washed with 200 µl of 1x BRB80 at 37 °C twice and re-suspended in 50 µl of warm 1x BRB80. 5 µl of 6.7 µM of monoclonal mouse-raised anti-FLAG M2 antibody (Sigma Aldrich) and 5 µl of 11.45 µM of goat anti-mouse antibody conjugated to 4 nm spherical gold nanoparticles, C11-4-TGAMG-50, (Nanopartz) were added to microtubules to label repaired sites. Antibody labeling was allowed to proceed for 5 min and the reaction was mixed with 10 volumes of 30 % glycerol in 1x BRB80. Microtubules in 30% glycerol were loaded on 1x BRB80 cushion containing 40% glycerol and spun down onto glow-discharged carbon-coated grids (Carbon Film only on 400 mesh, Ted Pella, Inc.) at 4,200 x g for 20 min at 30 °C. Excess liquid was blotted using filter paper. Grids were washed three times with 30 µl of BRB80, stained with 0.75 % (w/v) uranyl formate and air-dried. Images were collected on a T12 Technai electron microscope (FEI) equipped with a 2k x 2k Gatan US1000 CCD camera. Images were collected at nominal magnifications of 6,800x and 18,500x corresponding to pixel sizes of 6.8 Å/pix, 2.5 Å/pix, respectively. Images in fig. S7F were collected on a TF20 electron microscope (FEI) equipped with a K2 camera (Gatan). Images were collected at 50,000x magnification and 9,600x magnifications corresponding to pixel sizes of 0.73 Å/pix and 3.65 Å/pix, respectively.

Live imaging of severing and tubulin incorporation into nanodamaged GMPCPP-microtubules and GMPCPP-capped GDP-microtubules.

To observe microtubule severing and tubulin incorporation at damage sites simultaneously (**Fig. 3** and figs. S5A-C), GMPCPP-stabilized double-cycled microtubules labeled with 20% HiLyte647-tubulin were immobilized in imaging chambers. Image acquisition was started using 100 ms continuous exposure in the 647 and 488 channels simultaneously and the chamber was perfused with severing buffer containing 0.5 mM GTP, 20 nM spastin and 0, 0.1 or 2 μM HiLyte488-labeled tubulin. Severing rates were calculated by manual counting of severing events (microtubule breaks) as a function of time. Tubulin incorporation sites were readily visible in the 488 channel. To observe the live incorporation of single tubulin dimers into microtubules damaged by spastin (**Figs. 3F, G**), double-cycled GMPCPP microtubules composed of 20% HiLyte647-labeled and 1% biotinylated tubulin were immobilized in imaging chambers as above. The chamber was then perfused with severing buffer and images of microtubules were acquired. Microtubules were then incubated for 30 sec with 20 nM spastin in severing buffer. Image acquisition was started during the spastin incubation step and a solution containing fluorescently labeled tubulin (50 nM Alexa488-labeled tubulin (PurSolutions LLC, USA) in BRB80 with 2 mg/ml casein, 14.3 mM 2-mercaptoethanol, 50 mM KCl, 2.5 mM $MgCl_2$, 1 mM ADP, 0.5 mM GTP, 1% Pluronic F127 and oxygen scavengers) was flushed in. Images were acquired for 5 min at 10 Hz in the 488 nm channel. After tubulin perfusion, the 640 laser was turned off to prevent photobleaching or microtubule photodamage. Images of fluorescent tubulin molecules landing on the microtubule were analyzed using a 7x7 pixel box and the intensity of tubulin molecules incorporated into the microtubule was calibrated against the intensity of single tubulin dimers obtained by immobilizing 0.5 nM Alexa488 tubulin on glass with an anti-β tubulin antibody (SAP.4G5, Sigma Aldrich) and imaging under the same conditions.

For imaging of non-stabilized microtubules GDP microtubules with a GMPCPP cap, sea urchin axonemes purified as described (198) were non-specifically adhered to the coverslip and 15 mM containing 20% HiLyte647 tubulin and GTP added to start microtubule growth from the axonemes. After the desired microtubule length was achieved (10-20 mm), the solution was exchanged quickly to introduce HiLyte488 tubulin (20%) and 0.5 mM GMPCPP. After the growth of the GMPCPP cap, tubulin and nucleotide were washed out and spastin (5 nM) was introduced in the chamber with 1 mM ATP in the absence or presence of soluble tubulin at 2 mM (500 nM HiLyte488 tubulin + 1.5 mM unlabeled tubulin) or 5 mM (500 nM HiLyte488 tubulin + 4.5 mM unlabeled tubulin) and 0.5 mM GTP. Polymerization and imaging were performed at 30ºC.

Microtubule dynamics measurements and EB1 recognition of lattice-incorporated GTP-tubulin

TIRF microscopy chambers were prepared as described above. 10% HiLyte647-labeled microtubules were polymerized at 30°C at 10 μM tubulin. 25 nM spastin or katanin and 10 μM porcine brain tubulin containing 10% HyLite647-labeled tubulin was perfused into the chamber in severing assay buffer (50 mM KCl, 1% F127 Pluronic, 0.2 mg/ml casein, 6.2 mM 2-mercaptoethanol, 1.5% glycerol, 0.1% methylcellulose 4000cP and oxygen scavengers in 1xBRB80) with 0.5 mM GTP and 1 mM ATP) together with 50 or 75 nM EB1-GFP for katanin and spastin, respectively. Images were acquired in the 647 and 488 channels simultaneously at 2 Hz. Microtubule rescues are defined as transition of microtubules from shrinkage to growth. Rescue frequency was calculated as the number of rescues divided by the time spent depolymerizing. Catastrophes are defined as the transition of microtubules from growth to shrinkage. Catastrophe frequency was calculated as the number of catastrophes divided by the

time spent in the polymerization state. The EB1 puncta and the microtubule rescue site were considered co-localized when the distance between the EB1 spot and the end of the depolymerizing microtubule was less than two pixels. The cutoff for an EB1 puncta was defined as having a mean intensity in a 5x5 pixel box that is at least 3 standard deviations above the mean background EB1 lattice intensity. Background EB1 lattice intensity was determined from control chambers without severing enzymes. Background EB1 lattice intensity was the same in the absence of severing enzymes or the presence of severing enzymes but in the absence of ATP. For statistical significance calculation, rescue site analysis was also performed using synthetic data generated by shifting the position of the EB1 spots by 7 pixels on the microtubule (alternatively, both towards the plus and the minus ends).

For the GTP-tubulin and EB1-GFP co-localization experiments shown in **Fig. 6E**, microtubule extensions were grown in the absence of fluorescent tubulin for 8 minutes at 30°C at 12 μM porcine brain tubulin (Cytoskeleton) in severing assay buffer. 20 nM spastin, 50nM EB1-GFP and 12μM porcine brain tubulin containing 10% HyLite647-labeled tubulin was perfused into the chamber in severing assay buffer. Image acquisition was started during perfusion in the 640 and 488 channels simultaneously at 5 Hz. The offset between the 640 and 488 channels was corrected using a nanogrid (Nanogrid Miraloma Tech) and the GridAligner plug-in in ImageJ.

Laser ablation of microtubules with spastin or katanin generated GMPCPP-islands

GMPCPP-stabilized unmodified microtubule seeds were immobilized on glass. To pre-grow microtubules, 16μM tubulin containing 12.5% HiLyte647-labeled tubulin with 1mM GTP was perfused into the chamber and incubated for 10 minutes at 30°C. Microtubules were then capped using 6μM tubulin with 10% HiLyte 647 and 0.5mM GMPCPP. The chamber was washed after 2 minutes with severing assay buffer without GTP and then incubated with 4nM spastin, 6μM

tubulin containing 25% HiLyte-labeled 488 tubulin in the presence of 200μM GMPCPP in severing assay buffer (50 mM KCl, 1% F127 Pluronic, 0.2 mg/ml casein, 6.2 mM 2-mercaptoethanol, 2.5% glycerol, 0.1% methylcellulose 4000cP and oxygen scavengers in 1xBRB80) with or without 1mM ATP for 3 minutes. The chamber was washed with buffer containing severing assay buffer. Microtubules were ablated with a 405nm laser at 40% power using the iLas laser illuminator (BioVision). Images in the 488 and 647 channels were acquired sequentially with 100 ms exposure. For the rescue frequency measurements, 15% HiLyte647-labeled tubulin at 7μM in severing assay buffer containing 1mM GTP was perfused into the chamber. For the katanin experiments, the chamber was washed after microtubule capping with severing assay buffer without GTP and then incubated with 20nM katanin and 8μM tubulin containing 25% HiLyte-labeled 488 tubulin in the presence of 200μM GMPCPP in severing assay buffer with or without ATP for 45 sec. Microtubule depolymerization rates through the GMPCPP islands were determined by dividing the length of the island to the time it takes to depolymerize through it.

Laser ablation of dynamic microtubules with enzyme-generated GTP islands

TIRF microscopy chambers were prepared as described above. HiLyte647-labeled microtubule extensions were polymerized for 8 minutes at 30°C at 12 μM porcine brain tubulin (Cytoskeleton) containing 20% HiLyte647-labeled tubulin in severing assay buffer. 25 nM spastin or katanin, 50nM EB1-GFP and 12μM porcine brain tubulin containing 20% HyLite647-labeled tubulin was perfused into the chamber in severing assay buffer with ATP or ATPγS. Microtubules were ablated using a DeltaVision OMX™ with the 405nm laser at 100% power for 1 sec or with a 405nm laser at 40% power using an iLas laser illuminator (BioVision). Images were acquired in the 647 and 488 channels at 5 Hz.

Live imaging of tubulin incorporation and severing into dynamic microtubules

Chambers for TIRF microscopy were prepared as described above. GMPCPP-stabilized, unmodified microtubules containing 2% biotinylated tubulin were immobilized with 0.1 mg/ml NeutrAvidin (Thermo Fisher Scientific). Microtubule extensions were polymerized for 12 minutes at 30°C at 12 μM porcine brain tubulin (Cytoskeleton) containing 10% HiLyte647 tubulin in severing assay buffer (50 mM KCl, 1% F127 Pluronic, 1 mM ATP, 1 mM GTP, 0.2 mg/ml casein, 6.2 mM 2-mercaptoethanol, 1.5% glycerol, 0.1% methylcellulose 4000cP and oxygen scavengers in 1xBRB80). Then, 25 nM katanin or spastin with 12 μM porcine brain tubulin containing 10% HyLite488-labeled tubulin was perfused into the chamber in severing assay buffer. Images were acquired with 488 and 640 lasers simultaneously at 2 Hz at 100 ms exposure. The incorporation of the HiLyte488 tubulin was immediately visible upon perfusion only at microtubule tips in the control and along the microtubules and the dynamic tips in the enzyme and ATP conditions. Total polymer mass was obtained by measuring the background corrected total integrated fluorescence in both the 488 and 640 channels. The laser ablation controls were performed at the same enzyme and tubulin concentrations but with 1mM ATPγS. Microtubules were ablated with a 405nm laser at 40% power using an iLas laser illuminator (BioVision).

Quantification and Data Analysis

N numbers and statistical tests are reported for all experiments in figure legends. All experiments were performed multiple times and only representative images are shown. ImageJ was used for image analysis. Prism (Graphpad) was used for graphing and statistical analysis.

Results

Severing enzymes nanodamage microtubules

Because light microscopy-based severing assays fail to capture ultrastructural features of severing intermediates due to resolution limitations, we used negative-stain TEM to capture and image spastin-mediated microtubule severing intermediates in vitro using purified, recombinant spastin. To minimize severing intermediate breakage, we performed severing reactions directly on EM grids. These revealed a high density of "bites" into the protofilament structure (Figure 1) that resulted in the removal of tubulin dimers. Severing reactions performed with taxol-stabilized microtubules in the tube and then transferred to EM grids by pipetting produced many short microtubules with blunt ends (Figure S1A), similar to those previously reported in vitro with katanin (199) indicating that the fragile nanodamaged severing intermediates are lost during pipetting. Thus, in our on-grid severing setup, we were able to capture intermediates that were otherwise disrupted by shear forces introduced by pipetting. Upon prolonged incubation (>5min), severing was driven to completion on the EM grid, with severe destruction of the microtubule structure indicating that the intermediates observed were on-pathway (Figure S1B). The nanoscale damage sites were observed with GDP microtubules regardless of whether they were stabilized with taxol or not (Figures 1A, B) or polymerized with the non-hydrolyzable analog GMPCPP (Figure 1C). The nanodamage we observed in vitro is reminiscent of that observed by electron tomography in freeze-substituted *C. elegans* meiotic spindles (104). The same extraction of tubulin dimers and protofilament fraying was observed if reactions were performed in solution and then microtubules were deposited on an EM grid without pipetting to avoid shear (Figure 1D; Materials and Methods). In control reactions without the enzyme the integrity of the lattice was preserved, (Figures S1C and S1D), while in the spastin treated

samples nanodamage sites were detected every ~2.2 mm (Figure S1D). Time-course experiments revealed a gradual increase in nanoscale damage as well as number of shorter microtubules (Figure 1E). We extended our TEM analyses to the microtubule-severing enzyme katanin (Figures 1F, 1G and S1E-G). As with spastin, TEM revealed that katanin microtubule severing also proceeds through progressive extraction of tubulin dimers out of the microtubule.

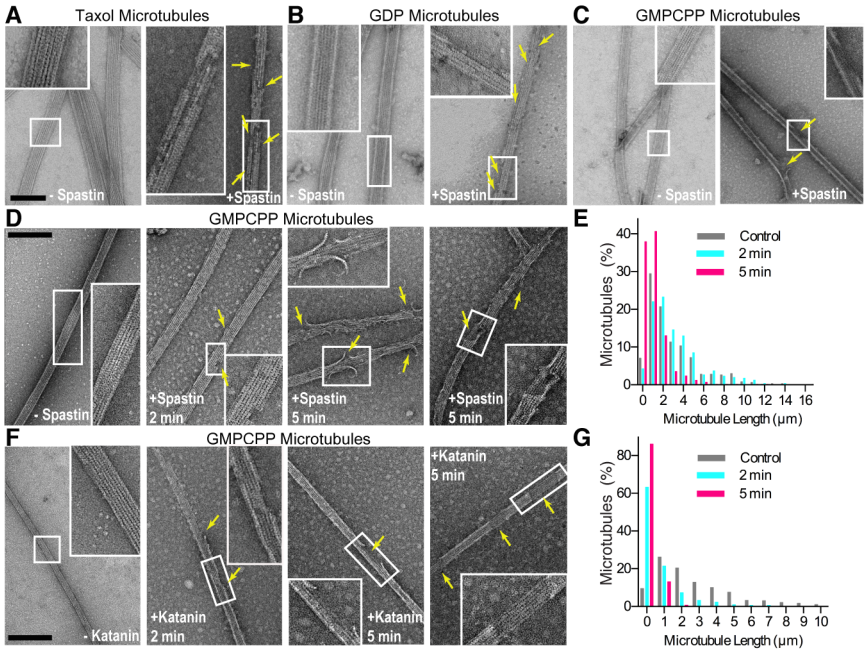

Figure 1: Spastin and katanin extract tubulin out of the microtubule
A–C) Microtubules in the absence or presence of spastin. The reaction proceeded on-grid for one minute and was imaged using negative stain TEM (Materials and Methods). Boxed regions shown at 2X magnification in insets. Scale bar, 50 nm. Microtubules imaged at 30,000x magnification. Arrows indicate nanoscale damage sites. D) Fields of GMPCPP microtubules incubated with buffer or 25nM spastin. Severing proceeded in solution and reactions were passively deposited on EM grids, negatively stained and visualized by TEM (Materials and Methods). Arrows indicate nanoscale damage. Microtubules imaged at 13,000x magnification; boxed regions, 30,000x magnification. Scale bar, 50 nm. E) Microtubule length distribution after spastin incubation; cyan, control; dark and light grey, 2 and 5 min incubation, respectively. F) Fields of GMPCPP microtubules incubated with buffer or 100 nM katanin imaged as in (D). Scale bar, 50 nm. G) Microtubule length distribution after katanin incubation; cyan, control; dark and light grey, 2 and 5 min incubation, respectively.

Figure 1 contributed by Dr. Elena Zehr & Dr. Alexandra Deaconescu

Tubulin incorporation repairs nanodamage

Our TEM analysis showed that GMPCPP or taxol-stabilized microtubules or non-stabilized microtubules, do not sever even when peppered with spastin and katanin induced nanodamage and do not catastrophically depolymerize upon removal of the initial tubulin subunits. This raised the possibility that this damage could be repaired by incorporation of tubulin subunits from the soluble pool, as recently observed with mechanically damaged or photodamaged microtubules (200, 201). To test this hypothesis, we preassembled HiLyte647 fluorescently-labeled GMPCPP microtubules and incubated them with spastin (or katanin) and ATP to initiate severing (Materials and Methods). Under these conditions, we observed rare severing events (Figure 2). Upon perfusion of soluble HiLyte488-labeled tubulin and GTP we observed tubulin incorporation in discrete patches along microtubules. These were numerous, far exceeding the number of severing events. Mock-treated microtubules showed no incorporation of tubulin into microtubules (Figures 2A-C). The tubulin concentration used was below the critical concentration for tubulin polymerization. Similar results were obtained with taxol-stabilized microtubules (Figure S2). Because photodamage can induce lattice defects in fluorescently labeled microtubules (201), we also performed experiments with unlabeled microtubules visualized by differential interference contrast (DIC) microscopy and also observed incorporation of tubulin in spastin-treated microtubules, but not in controls (Figure 2D).

In time-course experiments both the number of repaired nanoscale damage sites and mean fluorescence along repaired microtubules increased over time (Figures S3A, S3B, S4A, S4B). The size of the repair sites (full-width-at-half-maximum, FWHM, Figures S3C, S4C) was initially diffraction-limited and shifted toward larger values at longer incubation times, indicating an expansion of the damage as detected by soluble GTP-tubulin incorporation. Frequent

nanoscale damage events were visible when severing events were extremely sparse: as early as 35 s, the density of spastin-induced nanoscale damage sites was 0.35±0.01 mm^{-1}, compared to 0.0008±0.0004 mm^{-1} for severing events (Figures S3A, S3D). Thus, nanoscale damage precedes a macroscopic severing event. Once a sufficient number of tubulin dimers was removed from the lattice, the microtubule unraveled and a macroscopic severing event was visible. Consistent with this, we observed an abrupt increase in mesoscale severing at 120 and 90s for spastin and katanin, respectively (Figures S3D, S4D).

Next, we probed the effect of soluble tubulin on spastin microtubule severing by performing severing assays in the presence of fluorescently-labeled soluble tubulin (Figure S5). This allowed us to detect microtubule nanoscale damage and severing simultaneously. Spastin-induced severing was not significantly affected with 100 nM tubulin even though we observed incorporation of HiLyte-488 labeled tubulin into microtubules (Figure 3A and S5; Materials and Methods). However, severing was considerably reduced in the presence of 2 mM soluble tubulin (Figure 3A), and in this case, tubulin fluorescence intensity at repair sites was also significantly higher (Figure 3B). Thus, the tubulin extraction activity of the enzyme was not significantly inhibited by soluble tubulin as proposed previously for katanin (202), but the rate of tubulin incorporation at nanodamage sites increased with tubulin concentration and slowed down the progression to a macroscopic severing event. This higher tubulin incorporation at damage sites delays (and can even prevent) the completion of a severing event. Consistent with this, the time between the incorporation of HiLyte488-tubulin at a nanoscale damage site and the completion of a severing event was longer in the presence of 2 mM tubulin compared to 100 nM (Figure 3C). Thus, while almost all nanoscale damage sites detectable under our experimental conditions proceeded to complete severing within 65s after tubulin incorporation in the presence of 100 nM

soluble tubulin, only 47% did so at 2 mM tubulin (Figure 3D). We also monitored live the addition of single fluorescently-labeled tubulin dimers by TIRF microscopy (Figure 3E; Materials and Methods). Fluorescence intensity analyses revealed that repair proceeded through the incorporation of mainly tubulin heterodimers and not the addition of larger tubulin polymers or aggregates because the fluorescence intensity distribution of incorporated tubulin was similar to the one of single tubulin subunits immobilized to glass (Figure 3F).

Severing enzymes introduce GTP-tubulin islands

To rule out repair as an artifact of working with stabilized microtubules (either taxol or GMPCPP-stabilized), we extended our experiments to non-stabilized GDP-microtubules. We polymerized GDP-microtubules from axonemes and stabilized their ends with a GMPCPP cap to avoid spontaneous depolymerization (Materials and Methods). We then introduced spastin in the absence or presence of fluorescently-labeled soluble GTP-tubulin. Within 50 s of introducing 5 nM spastin and 5 mM soluble tubulin (tubulin concentrations in vivo are 5-20 mM (203, 204) we observed incorporation of tubulin as puncta along microtubules (Figure 3G). At these enzyme and tubulin concentrations, most tubulin incorporation sites did not progress to a severing event, and the severing rate was considerably lower than in the absence of soluble tubulin (Figure 3H). However, tubulin incorporation always preceded microtubule-severing. No repair sites were observed in the absence of spastin. In the absence of soluble tubulin, GDP-microtubules disassembled 2.2 times faster than GMPCPP-stabilized microtubules (Figure 3H), likely because of the tighter lattice interactions of the latter. Thus, the local balance between active tubulin removal catalyzed by the enzyme and passive tubulin incorporation determines whether a nanodamage site progresses to a mesoscale severing event or fails to do so because of the repair with GTP-tubulin from the soluble pool.

We also visualized the lattice-incorporated tubulin at higher resolution using TEM. We generated recombinant human α1A/βIII tubulin with an engineered FLAG-tag at the β-tubulin C-terminus (74). We then used this recombinant tubulin to repair brain microtubules nanodamaged by spastin. The presence of the FLAG-tag on the recombinant tubulin allowed its specific detection both in fluorescence and TEM images using fluorescent or gold-conjugated secondary antibodies against anti-FLAG antibodies (Materials and Methods). Fluorescence microscopy revealed that the recombinant tubulin robustly incorporates along microtubules in the presence of spastin and ATP. No incorporation was detected with spastin and ATPγS (Figure S6). TEM showed the discrete, productive incorporation of recombinant α1AβIII tubulin in islands along microtubules and the absence of tubulin aggregates at nanodamage sites (Figure S7). The anti-FLAG primary and secondary gold-conjugated antibody are specific for the recombinant tubulin as brain microtubules showed only background antibody decoration (Figure S7D). In the absence of recombinant soluble tubulin in the reaction, microtubules were robustly nanodamaged under these conditions (Figure S7E). Moreover, neither recombinant tubulin incorporation nor association with the microtubule lattice were observed by fluorescence and TEM assays with the slow-hydrolyzable analog ATPγS (Figures S7A and C). Thus, soluble tubulin incorporated productively into the microtubule lattice at nanodamage sites created by spastin in an ATP hydrolysis-dependent manner.

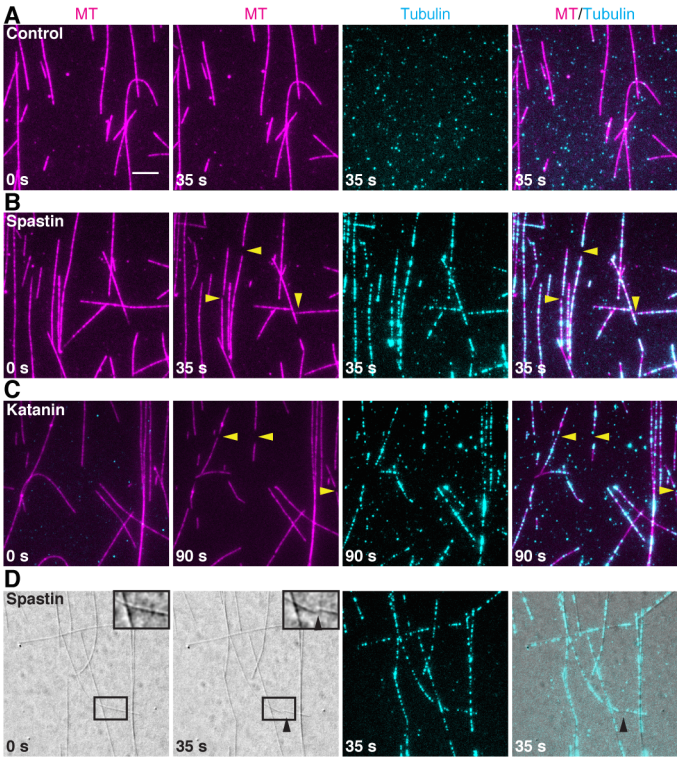

Figure 2: Spastin and katanin catalyzed nanoscale damage is repaired by spontaneous tubulin incorporation.
A, B) HiLyte647-labeled GMPCPP microtubules (magenta) incubated with buffer (A) or 10 nM spastin for 35 s (B) followed by incubation with 1 μM HiLyte488-labeled GTP-tubulin (cyan) and washing of excess tubulin (Materials and Methods); Arrows designate severing events. C) HiLyte647-labeled GMPCPP microtubules (magenta) incubated with 2 nM katanin for 90 s followed by incubation with 1 μM HiLyte488-labeled GTP-tubulin (cyan) and washing of excess tubulin (Materials and Methods). Arrows designate severing events. D) DIC imaged unlabeled GMPCPP microtubules incubated with 2 nM spastin followed by incubation with 1 μM HiLyte488-labeled GTP-tubulin (cyan) and washing of excess tubulin (Materials and Methods). Insets show severing events. Scale bar, 5 μm.

Figure 2 contributed by Dr. Ewa Szczesna

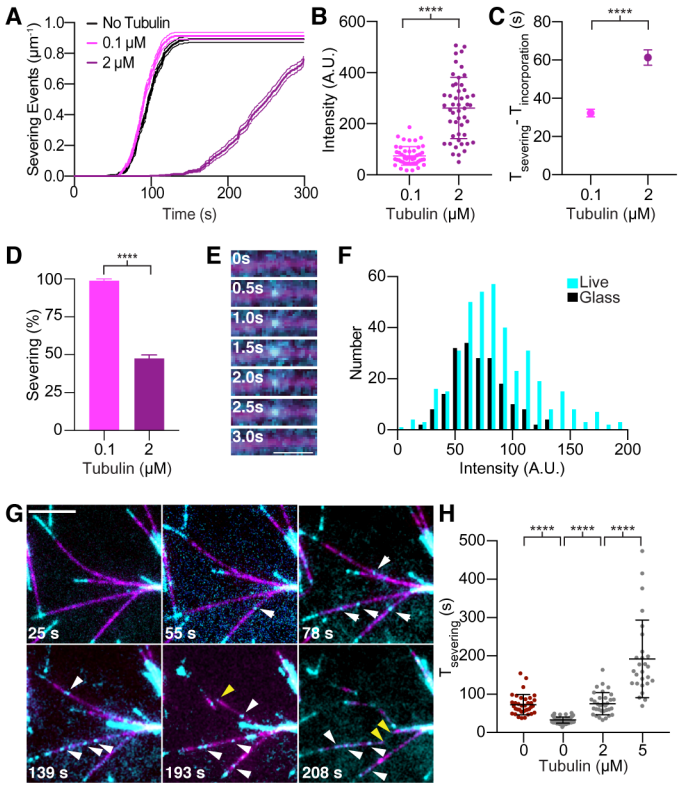

Figure 3: Incorporation of soluble tubulin into spastin-induced nanoscale damage sites inhibits microtubule severing

A) Severing rates in the presence of soluble tubulin (n= 31, 28 and 36 microtubules for no tubulin, 100 nm and 2 mM tubulin, respectively from multiple chambers). Error bars, s.e.m. B) Intensity distribution of fluorescent tubulin puncta incorporated at spastin-induced nanodamage sites; n=50 and 49 from multiple chambers for 100 nM and 2 μM tubulin, respectively. Bars, mean and s.d. C) Repair at damage sites delays severing (n=81 and 83 severing events from multiple chambers for 100 nM and 2mM tubulin, respectively). D) Fraction of GMPCPP microtubules severed by 20 nM spastin within 45 s of initial tubulin incorporation in the presence of 100nM and 2mM HiLyte488 soluble tubulin; Error bars, s.e.m. in (C) and (D). E) Live imaging of Alexa488 GTP-tubulin (cyan) incorporation into HiLyte647 GMPCPP microtubules (magenta) after spastin induced damage. Scale bar, 1.5 mm. F) Fluorescence intensity distribution of Alexa488-labeled tubulin (labeling ratio ~1.0) immobilized on glass (black) or incorporated into spastin induced nanodamage sites (cyan); n=188 and 398 for glass immobilized and microtubule incorporated particles, respectively. G) Spastin-induced nanodamage and spontaneous tubulin repair of GDP microtubules (magenta) grown from axonemes and stabilized with a GMPCPP cap (bright cyan); spastin (5 nM) and 5 mM soluble HiLyte488 GTP-tubulin (cyan). White arrows, tubulin incorporation sites, yellow arrows, severing events. Scale bar, 5 μm. H) Average completion time of a severing event after spastin perfusion. GMPCPP microtubules (brown), GMPCPP capped GDP microtubules (black, purple) in the absence or presence of soluble tubulin; n=36, 63, 34 and 27 microtubules from multiple chambers for GMPCPP, GMPCPP capped GDP microtubules with 2 μM and 5 μM soluble GTP-tubulin, respectively. Bars, mean and s.d.; **** p-value of < 0.0001 determined by two-tailed t-test for (B), (C) and (H).

Figure 3 contributed by Dr. Ewa Szczesna & Dr. Jeffrey Spector

Severing enzymes promote rescues

Because spastin and katanin catalyze GTP-tubulin incorporation along microtubules, we next examined their effects on microtubule dynamics. It has been recognized for 30 years that tubulin incorporation into a growing microtubule stimulates hydrolysis of the bound GTP. The resulting GDP-tubulin lattice is unstable, but is protected from depolymerization by a layer of GTP-tubulin. This "GTP-cap" at the microtubule end results from a lag between the GTP hydrolysis rate on the incorporated tubulin and microtubule growth speed (18, 45-48). More recently, islands of GTP-tubulin were detected along microtubules in cells and correlated with rescue (200, 205), the transition from depolymerization to growth, one of the parameters of microtubule dynamic instability. As with stabilized GMPCPP and GDP GMPCPP-capped microtubules, the newly perfused GTP-tubulin rapidly incorporated along the GDP-microtubule lattice of dynamic microtubules in the presence of spastin and katanin with ATP, unlike in the control without ATP where only addition at microtubule ends was visible (Figures 4A-D). We characterized microtubule dynamics in the presence of spastin or katanin at physiological concentrations (25 nM; spastin and katanin concentrations in HeLa cells are 46 nM and 28 nM, respectively (204)). At these enzyme concentrations, we observed robust microtubule severing and internal GTP-tubulin incorporation. Both spastin and katanin increased rescue frequencies ~ thirteen and nine-fold, respectively (0.5 ± 0.2 min^{-1} for control versus 6.6 ± 1.6 min^{-1} and 4.5 ± 0.7 min^{-1} for spastin and katanin, respectively; Figure 4E). While 61% of depolymerization events rescued in the presence of spastin or katanin, only 13% rescued in the control (Figure 4F). Consistent with their promotion of tubulin exchange along the microtubule shaft, neither spastin nor katanin had a significant effect on rates of microtubule growth and catastrophe (Figures 4G, H). This is in contrast to other rescue promoting factors like CLASPs, for example, which promote rescue by

increasing the on-rate of tubulin dimers at microtubule ends and thus decrease catastrophe and increase growth rates (206) or conventional MAPs like MAP2 which promote rescue by stabilizing the microtubule lattice (207).

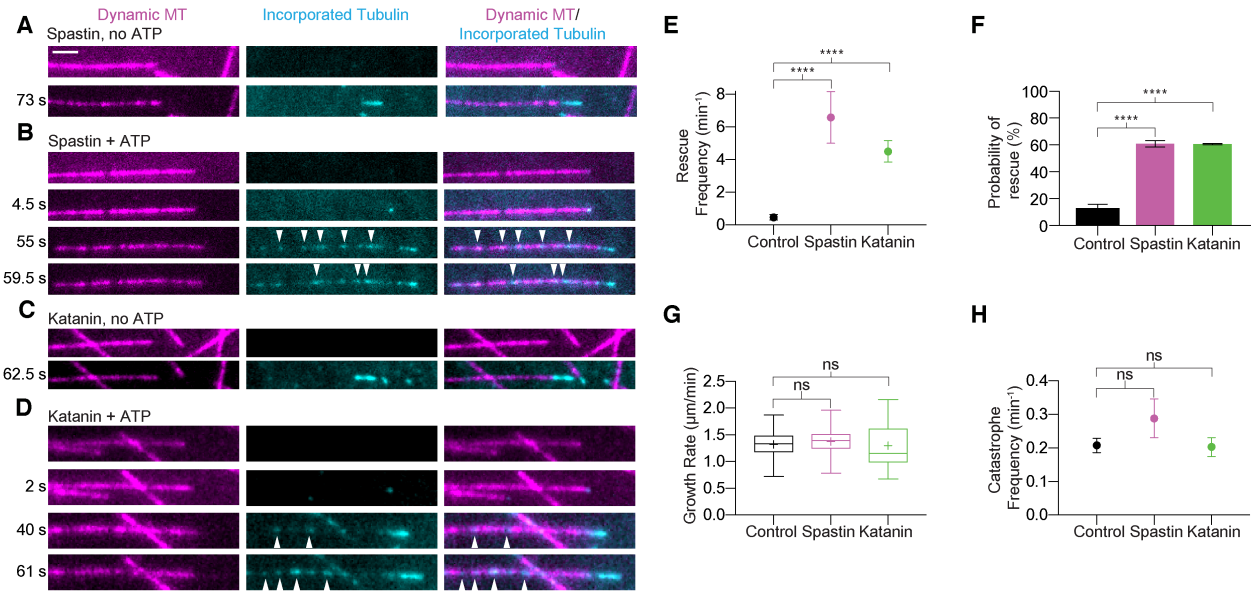

Figure 4: Spastin and katanin promote GTP-tubulin island formation and increase rescues
A, B) Time course of a dynamic 10% HiLyte647-labeled microtubule (magenta) at 10 mM tubulin in the presence of 25nM spastin without (A) or with ATP (B) showing HiLyte488-labeled tubulin incorporation (cyan) at the microtubule tip (A) or incorporation along the microtubule in addition to the tip (B). First micrograph for each condition was recorded just before the perfusion of 10 mM 10% HiLyte488-labeled tubulin into the chamber. Scale bar, 2μm. C, D) Time course of a dynamic 10% HiLyte647-labeled microtubule (magenta) at 10 mM tubulin in the presence of 25nM katanin without (C) or with ATP (D) showing HiLyte488-labeled tubulin incorporation (cyan) at the microtubule tip (C) or incorporation along the microtubule in addition to the tip (D). First micrograph for each condition was recorded just before the perfusion of 10 mM 10% HiLyte488-labeled tubulin into the chamber. Scale bar, 2μm. E) Rescue frequency at 10 mM tubulin in the absence or presence of 25 nM spastin and 25 nM katanin and ATP; n = 47, 45, and 61 microtubules from multiple chambers for control without enzyme, spastin and katanin, respectively. ****, p-value of < 0.0001 determined by the Mann-Whitney test; error bars, s.e.m. throughout. F) Probability of rescue of a depolymerizing microtubule in the absence or presence of spastin and katanin with ATP; n = 68, 57, 78 depolymerization events for control, spastin and katanin, respectively. ****, p-value of < 0.0001 determined by two-tailed t-test. G, H) Growth rates (G) and catastrophe frequency (H) in the absence or presence of spastin and katanin and ATP; n = 56, 37 and 34 growth events for control, spastin and katanin, respectively in (G) and n = 62, 70, and 71 microtubules for control, spastin and katanin, respectively in (H).

Severing enzyme-mediated GMPCPP-tubulin islands promote microtubule rescue

In our dynamics assays, tubulin is continually extracted by the enzyme, while at the same time, the lattice is healed with newly incorporated GTP-tubulin that gradually converts into GDP-tubulin. To decouple these processes and establish directly whether the GTP-tubulin islands introduced by these enzymes can act as microtubule rescue sites, we introduced non-hydrolyzable GTP-tubulin islands in the microtubule. For this, we first nanodamaged with spastin or katanin a GMPCPP-capped GDP microtubule and healed it with GMPCPP-tubulin, removed the enzyme and GMPCPP tubulin from the chamber, and initiated microtubule depolymerization through laser ablation close to the GMPCPP-cap (Figure 5; Materials and Methods). No GMPCPP-tubulin incorporation was detected in the control performed in the presence of enzyme but no ATP. These microtubules depolymerized all the way to the seed upon ablation (Figure 5B). In contrast, microtubules with GMPCPP-tubulin islands incorporated along their lengths through the ATP hydrolysis-dependent activity of spastin or katanin were stabilized against depolymerization at the location of the island (Figure 5C), despite the absence of soluble tubulin in the chamber: 75% and 76% paused when they encountered a GMPCPP island introduced by spastin or katanin, respectively (Figures 5D, S8A, B and C). Those that depolymerized through the island showed a decrease in the depolymerization speed (Figures 5E and S8D). Moreover, fluorescence intensity analysis revealed that GMPCPP-islands that paused depolymerization were statistically significantly brighter than those that did not (Figures 5F and S8E). Next, we wanted to establish whether these GMPCPP-islands were competent to support microtubule regrowth. For this, we performed the above experiment, but during the last step we introduced 7 μM soluble GTP-tubulin into the chamber (Figures 5A, G and H). While at these tubulin concentrations rescue events were very rare in the control, we saw a higher probability

of rescue of microtubules with spastin-incorporated GMPCPP islands (Figure 5I). When the GMPCPP-island did not support a rescue, it did however slow down depolymerization (Figure 5J). Moreover, fluorescence intensity analysis revealed that GMPCPP-islands that supported rescues were significantly brighter than those that did not (Figure 5K). Thus, microtubule dynamics measurements and experiments with GMPCPP-tubulin islands indicate that GTP-islands introduced in a microtubule severing enzyme-dependent manner promote microtubule rescue and that there is a minimal local GTP-tubulin density required to robustly support rescue at that site. Because the microtubule rescues when the balance shifts from net tubulin loss to net tubulin addition, it is likely that the correlation between the size of the GTP-tubulin island and rescue probability will vary with tubulin concentration or the presence of MAPs. These would increase tubulin on-rates and as a result smaller GTP-tubulin-islands might still be effective as rescue sites at higher tubulin concentrations when the tubulin on-rate is higher.

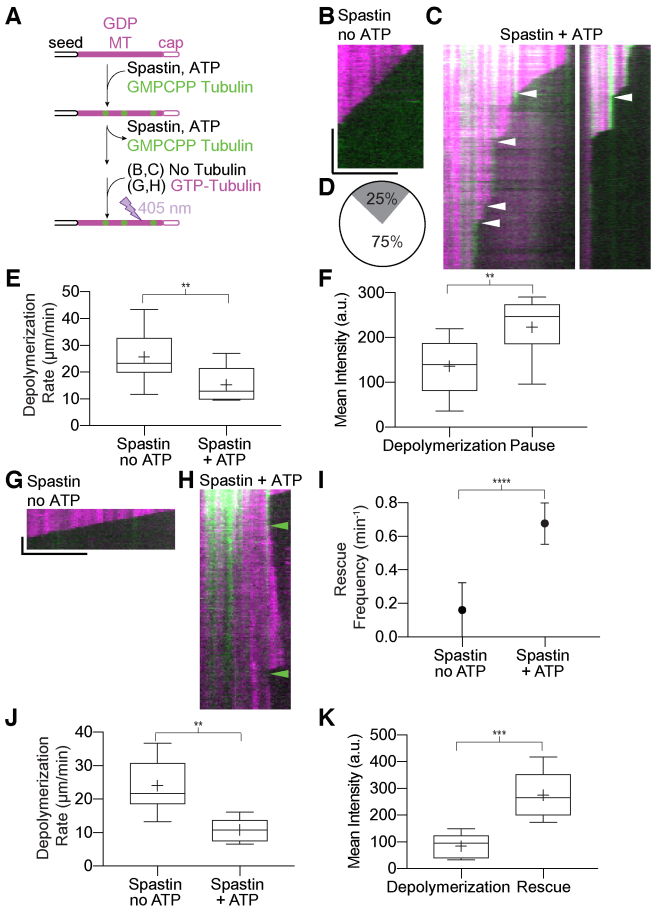

Figure 5: Enzyme generated GMPCPP-islands protect against depolymerization and act as rescue sites

A) Experiment schematic. GDP microtubules (solid magenta) were polymerized from seeds (black) and capped with GMPCPP-tubulin (magenta outline). Spastin, ATP and GMPCPP-tubulin (green) were added and washed out of the chamber. Microtubules were laser-ablated in the absence (B-F) or presence of GTP-tubulin (G-K) (Materials and Methods). B) Kymograph of a depolymerizing laser-ablated microtubule (magenta) pre-incubated with spastin, no ATP. C) Kymographs of depolymerizing laser-ablated microtubules pausing at GMPCPP-tubulin islands (green) introduced by spastin, 1mM ATP. White arrows, pauses. Horizontal scale bars, 5μm; vertical, 10 sec. D) Pie chart shows proportion of depolymerization events that paused at GMPCPP-islands (white) or did not (grey); n = 44. E) Depolymerization rates of microtubules without GMPCPP-islands pre-incubated with spastin, no ATP or through GMPCPP-islands introduced by spastin, 1mM ATP; n = 17 and 7 microtubules for no ATP and ATP, respectively. F) Intensity of GMPCPP-islands through which microtubules depolymerized or paused; n = 9 and 14, respectively. G, H) Kymographs of laser-ablated microtubules in the presence of 7μM soluble GTP-tubulin after pre-incubation with spastin no ATP showing complete depolymerization (G) or rescue (green arrows) at a GMPCPP-island introduced by spastin, ATP (H). Horizontal scale bar, 5μm; vertical, 20 sec. I) Rescue frequency of laser-ablated microtubules incubated with spastin, with or without ATP; n = 23 and 24 microtubules, respectively. J) Depolymerization rates in the presence of 7μM GTP-tubulin of microtubules pre-incubated with spastin, no ATP or through GMPCPP-islands introduced by spastin, ATP; n = 9 and 6 microtubules, respectively. K) Intensity of GMPCPP-islands that did not stop depolymerization (n=6) or at which microtubules rescued in the spastin, ATP condition (n = 9). **, ***, p-values of < 0.01 and 0.001 respectively determined by the Mann-Whitney test. Error bars, s.e.m. throughout.

Severing enzyme-generated GTP-islands recruit EB1

The GTP state of tubulin is recognized by MAPs belonging to the end binding (EB) protein family. EB1 preferentially binds to growing microtubule ends by sensing the GTP (or GDP-Pi) state of tubulin (208, 209). Consistent with the creation of GTP-tubulin islands, in the presence of spastin or katanin and ATP, we observed EB1 not only at the growing ends as in the control, but also as distinct puncta along microtubules (Figures 6A-D). These are reminiscent of the EB3 puncta observed at sites of tubulin repair after laser-induced damage (200). 89% of the newly-incorporated GTP-tubulin islands co-localized with EB1 (Figures 6E and F). These EB1 puncta were transient, consistent with the dynamic removal and incorporation of new tubulin into the lattice and the hydrolysis of the GTP within the lattice after the tubulin is incorporated (Figures 6A, C, and S9). Consistent with a protective effect of the GTP-islands, microtubule dynamics assays in the presence of spastin and EB1 revealed that 74% of rescues were associated with the presence of EB1 at the rescue site (Figure S10A). This number is significantly higher than the prediction given by the random superposition of EB1 puncta and rescue events (74% versus 14%, $p < 0.0001$ by Fisher test; Materials and Methods). Similarly, 63% of rescues in the presence of katanin occurred at the site of an EB1 spot (Figure S10B) compared to zero when the distribution was randomized ($p < 0.00001$ by Fisher test, Materials and Methods). Laser ablation of microtubules peppered with EB1 puncta also revealed a dramatic increase in rescue frequency. While 100% of ablation induced depolymerization events rescued within 4s, only 15% did so in the presence of spastin and ATPγS (Figures 6G and H). Similar results were obtained with katanin (Figure 6I). Thus, the ATP-dependent action of the enzyme that promotes tubulin exchange within the lattice is required for the observed increase in rescue frequency.

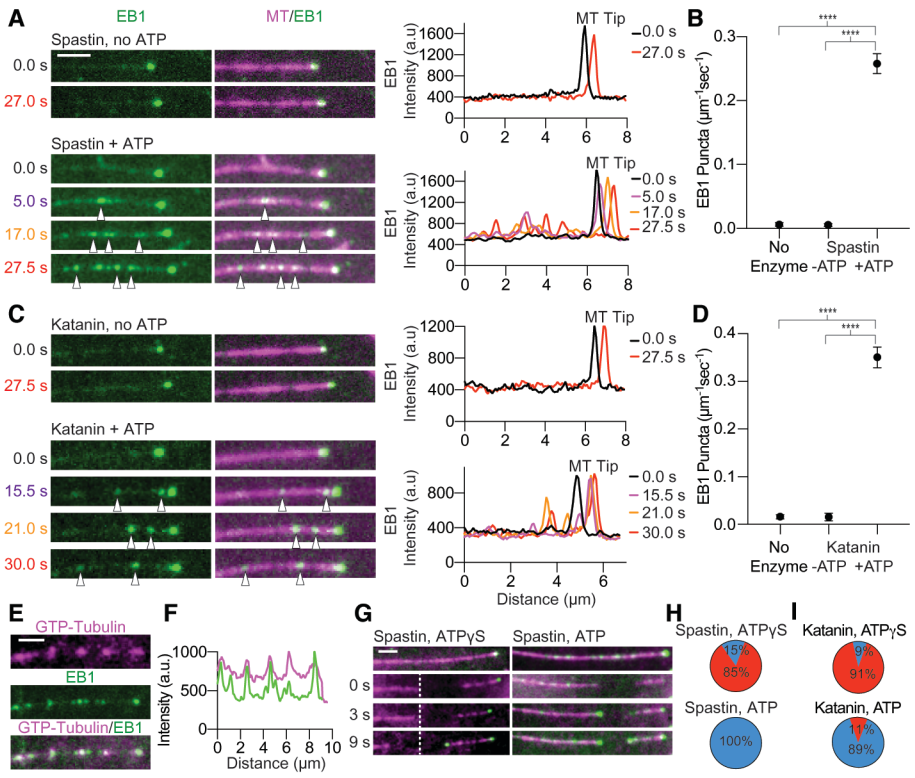

Figure 6: Spastin and katanin generated GTP-tubulin islands recruit EB1
A) Time course of EB1-GFP (green) on a dynamic microtubule (magenta) in the presence of 20nM spastin without or with ATP. Scale bar, 2 μm. Line scans on the right show EB1-GFP intensity profiles along the microtubule at indicated times. Intensity profiles start on the microtubule lattice and end at the microtubule tip. B) Density of EB1-GFP puncta on microtubules incubated without spastin or with spastin without and with ATP; error bars, s.e.m. (C) Time course of EB1-GFP on a dynamic microtubule in the presence of 25nM katanin without and with ATP. Intensity profiles as in (A). D) Density of EB1-GFP puncta on microtubules incubated without katanin or with katanin without or with ATP; error bars, s.e.m. E) Co-localization of newly incorporated GTP-tubulin (magenta, top panel) and EB1-GFP (green, middle panel) in the presence of spastin and ATP. Bottom panel, overlay. Images acquired immediately after perfusing enzyme and EB1-GFP into chamber. Scale bar, 2μm. F) Fluorescence intensity of incorporated tubulin (magenta) and EB1-GFP (green) along the microtubule lattice in (E) showing their co-localization. 89% of tubulin islands co-localize with EB1-GFP (n = 38 puncta from 22 microtubules from multiple chambers measured immediately after perfusion of 10% HyLite647-tubulin). G) Time course of laser-ablated dynamic microtubules (magenta) incubated with 25 nM spastin, ATPgS (left) or spastin, ATP (right) in the presence of 50 nM EB1-GFP (green) (Materials and Methods). The dotted line marks the ablated region and start of depolymerization. Scale bar, 2 μm. H, I) Fates of plus-ends generated through laser-ablation of microtubules incubated with spastin (H) or katanin (I) with ATPgS or ATP; % of plus-ends that depolymerized (red) or rescued (blue) within 4 s after ablation; n = 13 and 13 microtubules for spastin ATPγS and ATP, respectively, from multiple chambers; n = 54 and 9 microtubules for katanin ATPγS and ATP, respectively, from multiple chambers.

Figure 6A contributed by Dr. Ewa Szczesna. Figures 6B & D were contributed by Dr. Jeffrey Spector with data collected by Dr. Ewa Szczesna and me.

Severing amplifies microtubule mass and number

The GDP-tubulin lattice is unstable and when exposed by laser ablation rapidly depolymerized at the plus ends even in the presence of soluble tubulin (Figure 7A) consistent with classic experiments performed with laser ablated or mechanically cut microtubules (109-114). Surprisingly, at 12μM tubulin the majority of new plus-ends generated by spastin or katanin were stable and rapidly reinitiated growth (Figure 7B, C). In contrast, in the absence of either enzyme or in the presence of spastin or katanin and ATPγS new plus-ends generated through laser ablation rapidly depolymerized (Figures 7A, 6H, 6I). This indicates that it is not the passive binding of the protein that stabilizes the new plus-ends against spontaneous depolymerization but the ATP-dependent incorporation of GTP-tubulin at severing sites. The minus-ends were stable regardless of whether they were generated through enzyme action or laser ablation, consistent with classic earlier experiments using laser ablation (109, 110). Thus, when the local tubulin extraction by spastin or katanin outpaces the rate of tubulin incorporation, a severing event occurs and the newly-severed microtubule ends emerge with a high density of GTP-tubulin that is protective (Figures 7B, C). Moreover, the plus-ends that depolymerize immediately after severing resume growth after a lower net loss of polymer mass (Figures S8F, G). Thus, the increase in microtubule number with each severing event (Figures 7D, E) together with the higher rescue frequency synergize to produce a rapid amplification of total microtubule number and mass (Figures 7F-J).

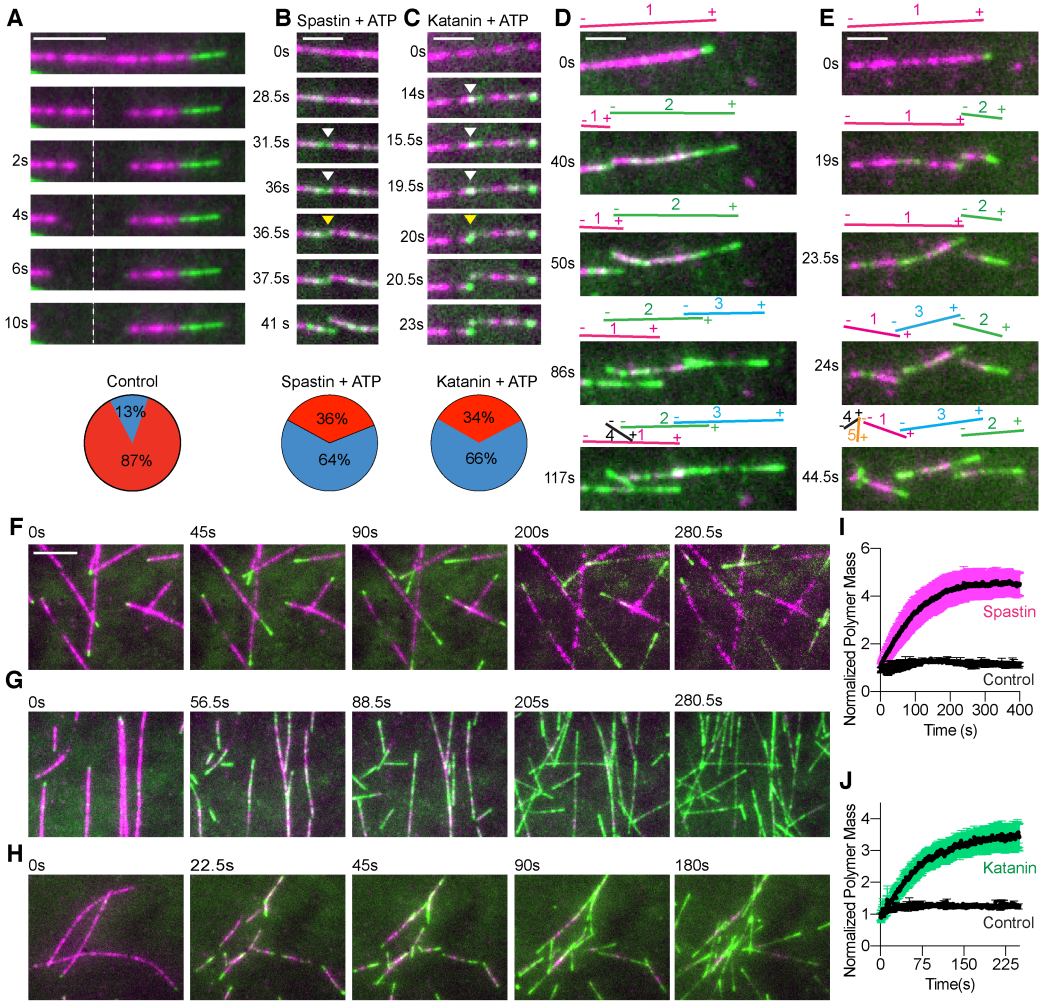

Figure 7: Severing enzyme-based microtubule number and mass amplification
A) Plus-ends generated through laser ablation depolymerize. Blue, % of plus-ends that are stable; red, % that depolymerize; n = 32 microtubules from multiple chambers. Scale bar, 5μm. B, C) Spastin (B) or katanin (C) severed ends emerge with newly incorporated GTP-tubulin and are stable. Blue, % of plus-ends that are stable; red, % that depolymerize; n= 96 and 94 for spastin and katanin, respectively from multiple chambers. Scale bar, 2μm. D, E) Time lapse showing consecutive spastin (D) or katanin (E) induced severing events on a microtubule. Microtubule (magenta), incorporated tubulin (green). Scale bar, 2μm. F) Time lapse showing microtubule dynamics at 12mM tubulin in the absence of severing enzyme. Green, newly incorporated tubulin at the growing ends. The last two frames are bleach corrected. Scale bar, 5μm. G, H) Time lapse showing microtubule number and mass amplification through spastin (G) and katanin (H) severing. Green, newly incorporated HiLyte-488 tubulin perfused into the chambers together with the severing enzymes. I, J) Microtubule mass as a function of time; n = 4, 5 and 4 chambers for control, spastin and katanin, respectively; error bars, s.e.m.

Figures 7I & J the quantitation was performed by Dr. Jeffrey Spector with my assistance on data that I gathered.

Discussion

The classical view of microtubule dynamics has been that tubulin dimer exchange occurs exclusively at microtubule ends through polymerization and depolymerization (18). By visualizing at the ultrastructural level a severing reaction, we show that spastin and katanin extract tubulin subunits from the microtubule (Figure 1) and that this ATP hydrolysis-dependent tubulin removal is counteracted by spontaneous lattice incorporation of soluble GTP-tubulin (Figures 2, 3, 4, S5, S6 and S7). The nanodamaged microtubules do not immediately unravel, but are long-lived enough to have a chance to heal through the productive incorporation of tubulin into the lattice. Because longitudinal lattice contacts are stronger than lateral ones (47), we speculate that tubulin dimer loss from the microtubule wall has a longitudinal, along the protofilament bias. This would give the microtubule a chance to heal before it is severed across and generate GTP-tubulin islands that consists of several tubulin dimers in the longitudinal direction. The geometry of the nanodamage sites and the mechanism of tubulin incorporation and conformational changes at these sites will be an exciting and fundamental question for future exploration.

This mechanism of lattice repair can explain the earlier observation of inhibition of katanin severing by soluble tubulin (77). The ragged, Swiss cheese-nature of the nanodamaged microtubules is conducive to healing, as the incoming tubulin dimers can make stabilizing lateral interactions. Thus, depending on the local rates of the severing enzyme-catalyzed tubulin removal and the spontaneous incorporation of new GTP-tubulin into the lattice, the action of a microtubule-severing enzyme results in a severing event where the newly-emerging ends have a high density of GTP-tubulin or a microtubule that preserves integrity but acquires a GTP-island

at the site of enzyme action. The higher GTP density at the newly severed ends can also act to quickly recruit cellular regulators that can modulate the fate of the newly generated end.

While microtubule repair after defects introduced through laser-induced photodamage (200) or mechanical stress has been reported *in vitro* (201) , our study identifies a family of enzymes as biological agents that promote the ATP-dependent incorporation of GTP-tubulin islands into microtubules. Microtubule repair has a high incidence *in vivo* at microtubule crossovers or bundles (200) where microtubule-severing enzymes act (94, 103, 184, 189). Our findings thus suggest that the high incidence of repair at these sites might not be due exclusively to mechanical damage (200), but also the action of microtubule-severing enzymes. Since spastin and katanin preferentially target glutamylated microtubules (38, 187, 210), they could also selectively rejuvenate through GTP-tubulin incorporation ageing microtubules with accumulated glutamylation marks. GTP-tubulin islands were reported along axonal microtubules (211), a neuronal compartment where severing enzyme act, raising the intriguing possibility that severing enzymes could also be used as quality control and maintenance factors in hyperstable microtubule arrays like those in axons, centrioles and cilia where spastin and katanin are important for their biogenesis and maintenance (83, 107, 181, 187) and where they could serve to remove and replace old, possibly damaged tubulin subunits without affecting overall microtubule organization. It will be thus interesting to establish how impaired lattice repair contributes to the disease phenotypes seen in patients with spastin and katanin mutations

Our study shows that severing enzyme-catalyzed incorporation of GTP-tubulin along microtubules has two physiological consequences: it increases the frequency at which microtubules rescue (Figures 4, 5 and 6) and stabilizes against depolymerization newly severed plus-ends that emerge with a high density of GTP-tubulin (Figure 7). Thus, microtubule

dynamics can be modulated not only by factors that affect tubulin incorporation at microtubule ends, but by severing enzymes that promote the exchange of tubulin subunits within the microtubule shaft. The synergy between the increased rescue rates and the stabilization of the newly-severed ends leads to microtubule amplification in the absence of a nucleating factor, explaining why, paradoxically, the loss of spastin and katanin results in loss of microtubule mass in many systems (104, 105, 107, 108). Such a mechanism of polymer amplification has parallels to the actin cytoskeleton where severed filaments are used for templated actin polymerization ((106, 212); reviewed in (213)). When severing enzymes are expressed at high levels or are positively regulated, tubulin extraction outpaces repair and the microtubule array disassembles. Cells likely modulate severing activity and the rate of tubulin lattice incorporation through the action MAPs to elicit these two different outcomes. This regulation will be a fascinating area of future exploration.

Experimental Contributions:

I performed the TIRF experiments with the dynamic microtubules and laser ablation. Dr. Ewa Szczesna performed assays with stabilized and dynamic microtubules. Drs. Ewa Szczesna, Jeff Spector, and I analyzed the data. Dr. Elena Zehr performed all of the EM experiments and Dr. Alexandra Deaconescu performed the initial EM with spastin. Katanin and EB1-GFP were purified by Dr. Agnieszka Szyk. Spastin was purified by Drs. Agnieszka Szyk and Ewa Szczesna. Dr. Agnieszka Szyk also purified the recombinant tubulin with my assistance. Throughout the chapter, contributions are listed for data I did not collect or analyze.

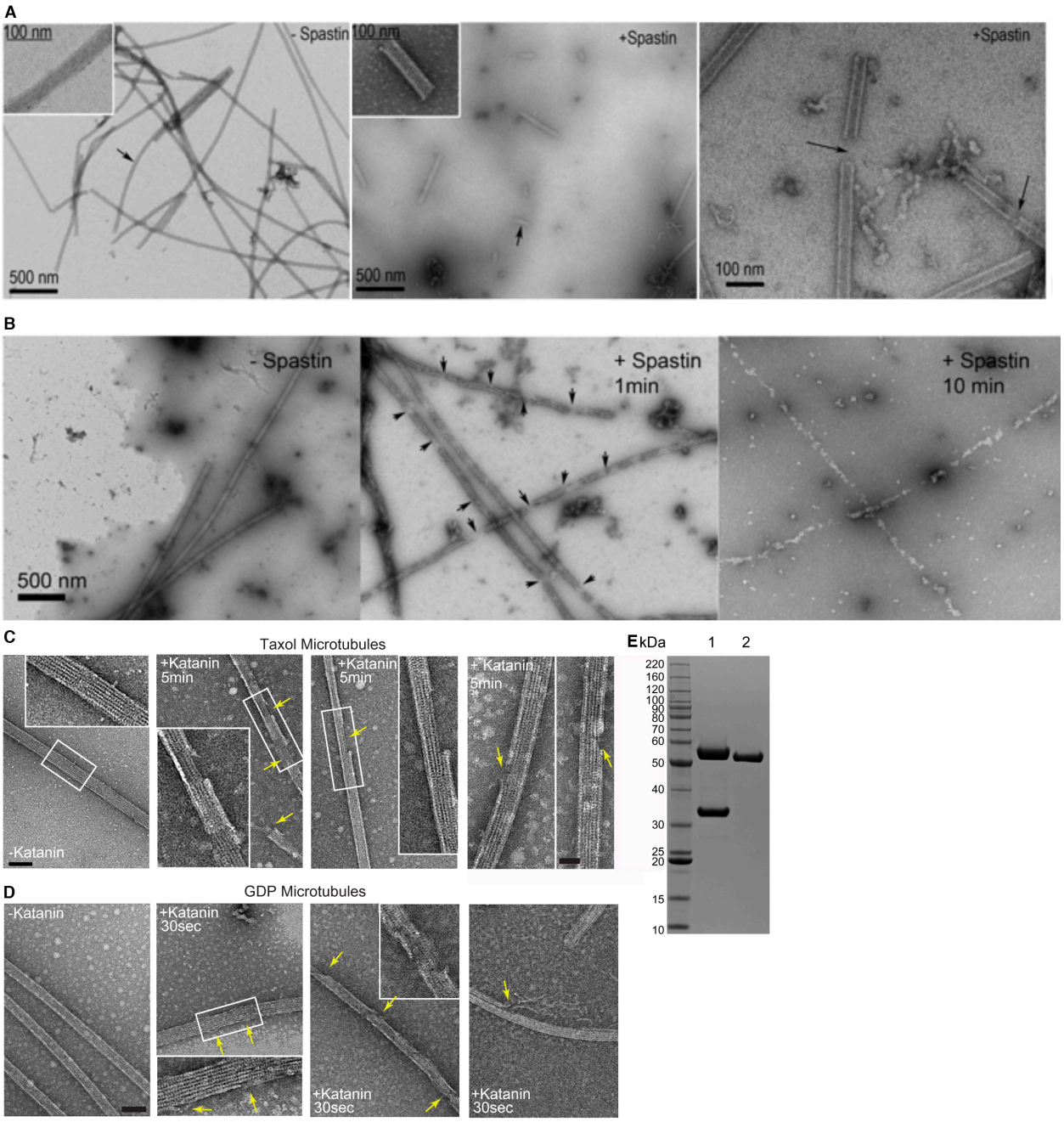

Figure S1: Transmission electron microscopy of spastin and katanin catalyzed microtubule-severing reactions

A) Fields of taxol-stabilized microtubules in control buffer or after incubation with spastin in solution and pipetted onto EM grid. Microtubules imaged at 14,000x magnification. B) Fields of taxol-stabilized microtubules in control buffer and in the presence of spastin negatively stained after 1 or 10 min of on-grid incubation. Black arrows indicate severing sites. After prolonged incubation with spastin (right), the protofilament structure of the microtubule is completely gone, and a proteinaceous residue is left on the grid. (C-D) Fields of taxol stabilized GDP microtubules (C) and GDP microtubules (D) incubated with buffer as control or katanin and ATP. Reactions were passively deposited on EM grids, negatively stained and visualized by TEM (Materials and Methods). Arrows indicate nanodamage sites; Scale bar, 50 nm.

Microtubules imaged at 13,000x magnification; boxed regions imaged at 30,000x magnification. (E) SDS gel showing bacterially expressed and purified katanin p60:p80 (lane 1) and spastin (lane 2) used in this study (Materials and Methods); 5 and 2.5 mg loaded for katanin and spastin, respectively.

Supplementary Figure 1 contributed by Dr. Elena Zehr

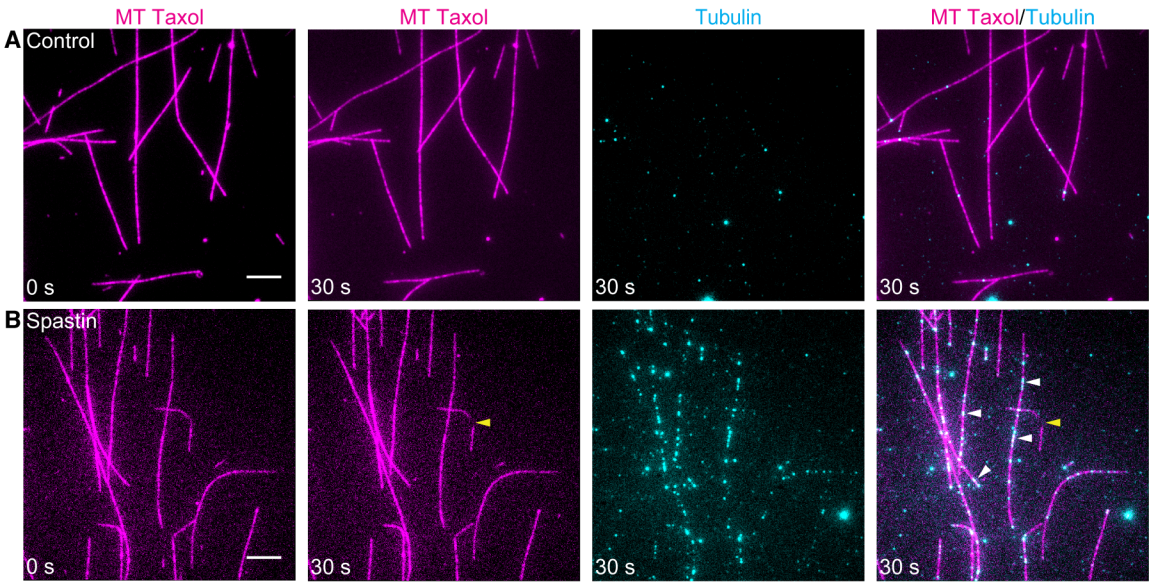

Figure S2: Soluble tubulin incorporates into taxol-stabilized microtubules after spastin-induced nanoscale damage

(A, B) Soluble tubulin incorporates into taxol-stabilized microtubules after spastin-induced nanoscale damage. HiLyte647-labeled taxol stabilized microtubules (magenta) incubated with buffer (A) or spastin (B) followed by incubation with 100 nM HiLyte488-labeled tubulin (cyan). The repair step was performed with 100 nM soluble tubulin to prevent microtubule nucleation in the presence of taxol. After 30 s incubation with spastin abundant tubulin incorporation is observed along the entire microtubule with few complete severing events detected (yellow arrows). Scale bar, 5 μm.

Supplementary Figure 2 contributed by Dr. Ewa Szczesna

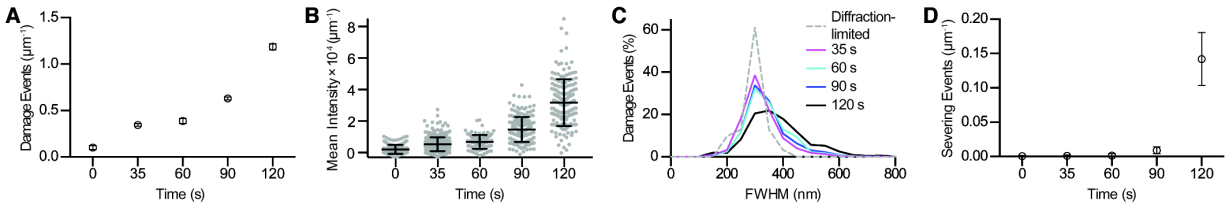

Figure S3: Progressive spastin mediated nanoscale damage precedes the onset of microtubule severing

A) Density of incorporated HiLyte488-labeled tubulin puncta along microtubules as a function of spastin incubation time; n = 188, 316, 100, 319 and 149 microtubules from multiple chambers for 0, 35, 60, 90 and 120s, respectively. B) Fluorescence intensity of incorporated HiLyte488-labeled tubulin puncta along microtubules as a function of spastin incubation time; n = 216, 385, 100, 201 and 161 from multiple chambers for 0, 35, 60, 90 and 120s, respectively. Error bars indicate s.d. C) Distribution of full-width-at-half-maximum (FWHM) of nanoscale damage sites as a function of spastin incubation time (n=1245, 398, 2457 and 971 events for 35, 60, 90 and 120 s respectively). The dashed line shows FWHM for 100 nm TetraSpeck microspheres (Thermo Fisher Scientific). D) Severing events (microtubule breaks) as a function of time (n=216, 385, 100, 161 and 201 microtubules for control, 35, 60, 90, and 120 s respectively for data in panels A, B and D). Error bars, s.e.m. **, p values < 0.01; ****, p values < 0.0001 determined by two tailed t-test with Welch correction.

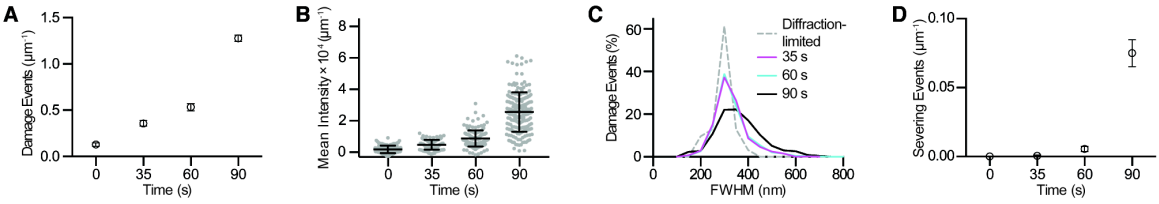

Figure S4: Progressive katanin mediated microtubule nanoscale damage precedes the onset of severing

A) Density of incorporated HiLyte488-labeled tubulin puncta along microtubules as a function of katanin incubation time; n = 57, 56, 45 and 91 microtubules from multiple chambers for 0, 35, 60, and 90s, respectively. B) HiLyte488 fluorescence intensity of incorporated HiLyte488-labeled tubulin puncta as a function of katanin incubation time; n = 144, 112, 177 and 192 for 0, 35, 60, and 90s, respectively. Error bars indicate s.d. C) Distribution of full-width-at-half-maximum (FWHM) of nanoscale damage sites as a function of katanin incubation time (n=519, 1246 and 1813 events for 35, 60 and 90 s respectively). The dashed line shows FWHM for 100 nm TetraSpeck microspheres (Thermo Fisher Scientific). D) Severing events (microtubule breaks) as a function of time (n=144, 112, 177 and 192 microtubules for control, 35, 60 and 90 s respectively for data in panels (A), (B) and (D), respectively. Error bars, s.e.m.; ***, p values < 0.001, ****, p values < 0.0001 determined by *!.

Supplementary Figures 3& 4 contributed by Dr. Ewa Szczesna & Dr. Jeffrey Spector

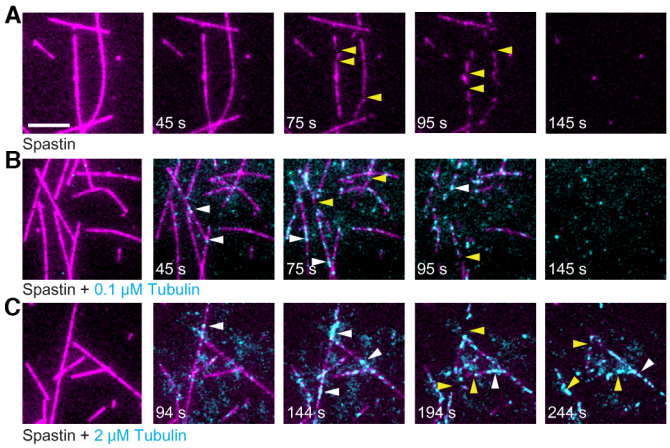

Figure S5: Incorporation of soluble tubulin into spastin-induced nanoscale damage sites inhibits microtubule severing

A-C) Spastin induced microtubule severing in the absence of tubulin (A) or presence of 100 nM (B) and 2 μM soluble HiLyte488-labeled tubulin (C). Microtubules (magenta), incorporated HiLyte488-labeled tubulin (cyan). White arrows indicate tubulin incorporation sites, yellow arrows, mesoscale severing events. Scale bar, 5 μm.

Supplementary Figure 5 contributed by Dr. Ewa Szczesna

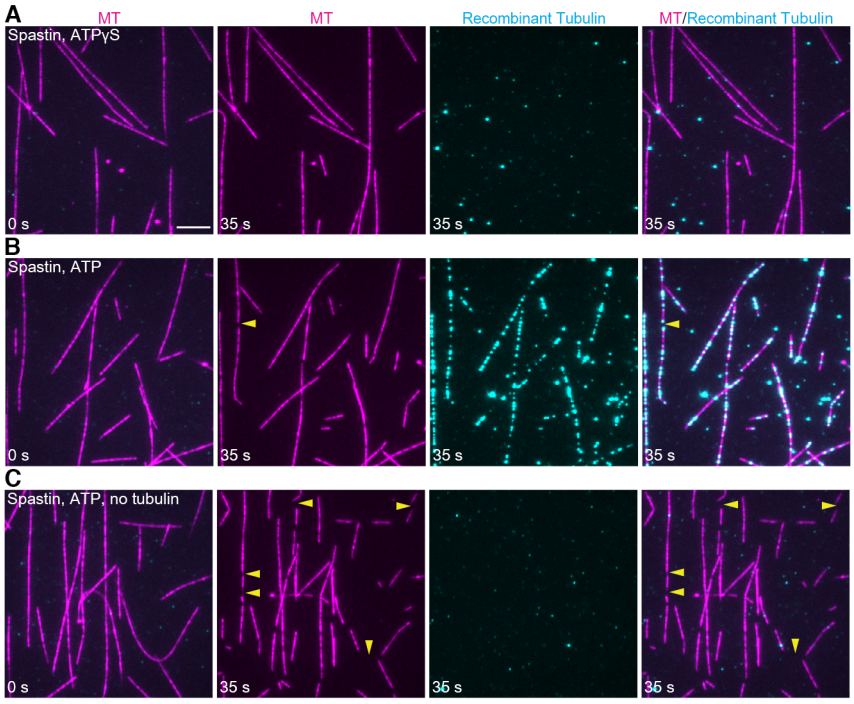

Figure S6: Recombinant FLAG-tagged tubulin incorporates into spastin nanodamaged microtubules

A–C) HiLyte647-labeled GMCPP brain microtubules (magenta) incubated with 10 nM spastin followed by incubation with 1 μM recombinant human α1A/βIII tubulin with a C-terminal FLAG tag on βIII-tubulin (Materials and Methods). The recombinant tubulin was detected by anti-FLAG antibodies and secondary Alexa488-labeled antibodies (cyan). Free tubulin does not incorporate into microtubules incubated with spastin and the non-hydrolyzable ATP analog ATPγS (A), while after 35 s incubation with spastin and ATP robust tubulin incorporation is observed along the entire length of the microtubule (B). Detection by the anti-FLAG antibodies is specific as there is no signal on spastin nanodamaged microtubules not incubated with recombinant tubulin (C). Yellow arrows indicate mesoscale severing events. Scale bar, 5 mm.

Supplementary Figure 6 contributed by Dr. Ewa Szczesna

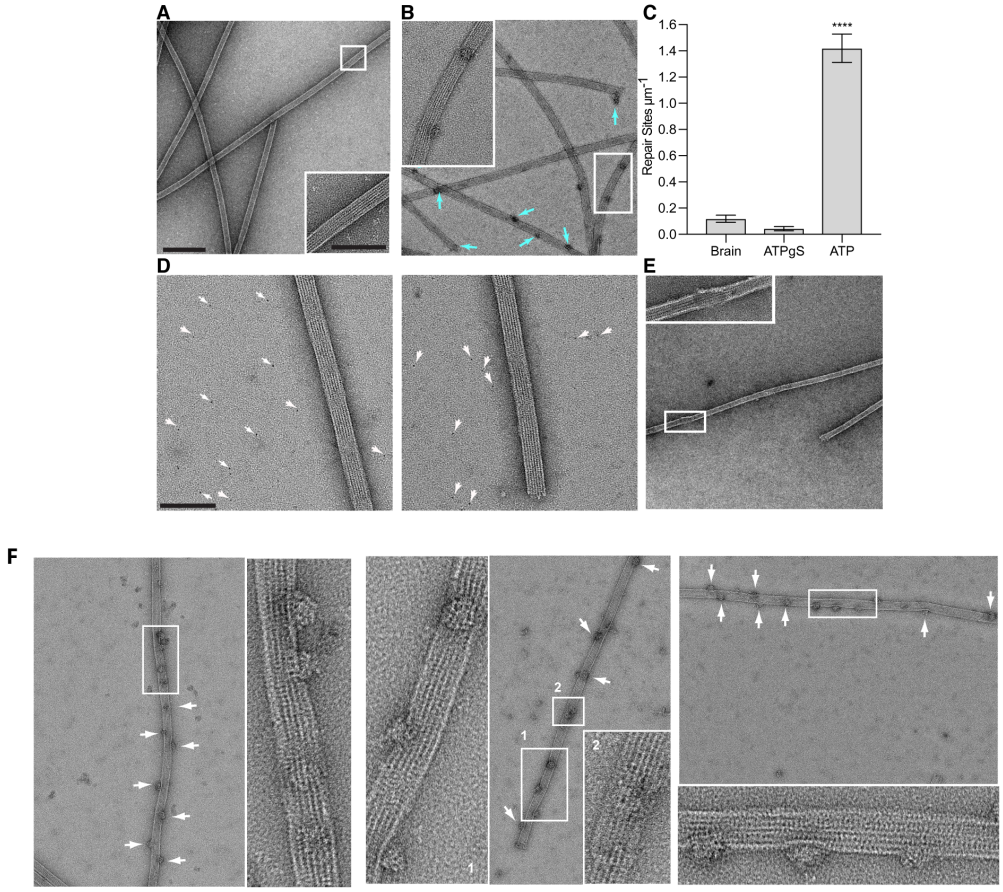

Figure S7: TEM shows tubulin incorporates productively into microtubules at nanoscale damage sites.

A, B) Fields of GMPCPP brain microtubules nanodamaged with spastin and repaired with FLAG-tagged recombinant human α1A/βIII tubulin negatively stained and visualized by TEM. Microtubules were incubated with spastin in solution for 30 sec in the presence of ATPγS (A) or ATP (B) and then repaired for 5 min by addition of soluble recombinant FLAG-tagged tubulin. Repair sites labeled with gold-conjugated anti-FLAG secondary antibodies are indicated by cyan arrows. Microtubules were imaged at 6,800x, scale bar 250 nm, and 18,500x, scale bar 100 nm, (*insets*) on a T12 Technai electron microscope (FEI) equipped with a 2k x 2k Gatan US1000 CCD camera. C) Number of gold conjugated anti-FLAG antibodies detected on brain microtubules and brain microtubules incubated with spastin and recombinant tubulin in the presence of ATPγS or ATP. 278 images and 93.7 µm of microtubule lattice were analyzed for brain microtubules, 300 images and 188.4 µm of microtubule lattice for the ATPγS condition and 339 images and 252.9 µm of microtubule lattice analyzed for the ATP condition. Error bars, s.e.m. ****, p values < 0.0001 determined by two-tailed t test. D) Immunogold-conjugated secondary antibodies and anti-FLAG antibodies, highlighted by white arrows, do not decorate brain microtubules. Scale bar 100nm. Microtubules imaged at 18,500x magnification, scale bar 100 nm. E) Unrepaired microtubules that were nanodamaged by spastin and not incubated with soluble recombinant tubulin. Microtubules imaged at 6,800x and 18,500x (insets) magnification. F) Nanodamage sites repaired with recombinant tubulin visualized at a magnification of 9,600, scale bar 200 nm; 50,000 for the insets, scale bar 50 nm on a TF20 (FEI) with a K2 camera (Gatan).

Supplementary Figure 7 contributed by Dr. Elena Zehr

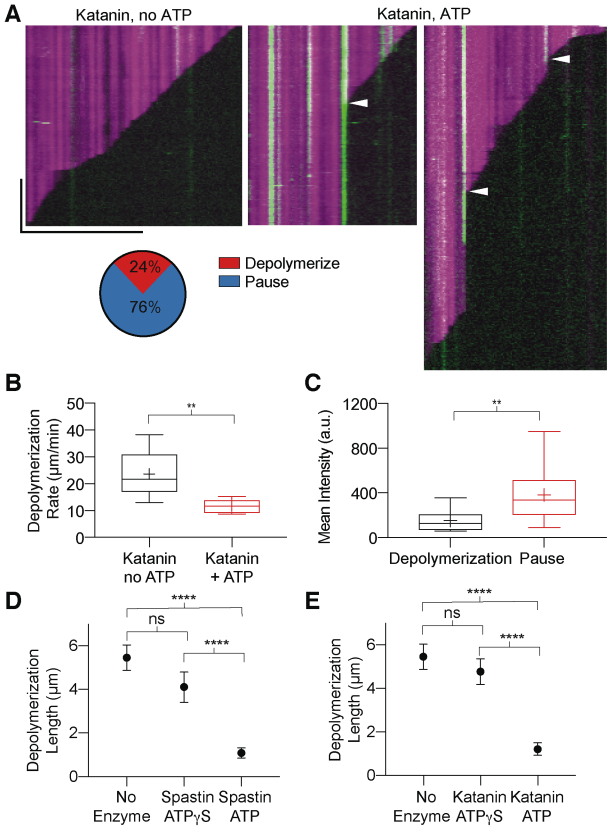

Figure S8: Katanin generated GMPCPP-islands protect against depolymerization
A) Representative kymographs of laser ablated microtubules (magenta) depolymerizing when incubated with katanin, no ATP with no visible GMCPP-tubulin incorporation (green) (left panel) or pausing at sites of GMPCPP-tubulin islands introduced by katanin in the presence of ATP (middle and right panels). White arrows designate pause sites. Horizontal scale bar, 5μm and vertical scale bar, 10 sec. Pie chart shows distribution of GMPCPP tubulin islands where microtubules paused (blue) or continued depolymerization (red) after laser-induced depolymerization; n = 37 GMPCPP tubulin islands from 21 microtubules from multiple chambers. B) Depolymerization rates of microtubules incubated with katanin, no ATP or through GMPCPP islands for microtubules incubated with katanin, ATP; n = 22 microtubules and 6 microtubules with GMPCPP islands for katanin, no ATP and katanin, ATP, respectively. C) Mean intensity of GMPCPP islands through which microtubules depolymerized or paused in the katanin, ATP condition; n = 11 and 23 for depolymerization and pauses, respectively. ** represents $p < 0.01$ determined by the Mann-Whitney test. D, E) Average polymer mass lost per severing-induced depolymerization event at 12 μM tubulin in the absence of any enzyme or in the presence of spastin or katanin with 1 mM ATPγS or ATP; n = 24 for no enzyme; n = 12 and 38 for spastin and katanin with ATPγS, respectively; n= 25 and 27 for spastin or katanin with ATP, respectively, all from multiple chambers. Severing was triggered through laser ablation in the no enzyme or spastin and katanin with ATPγS conditions.

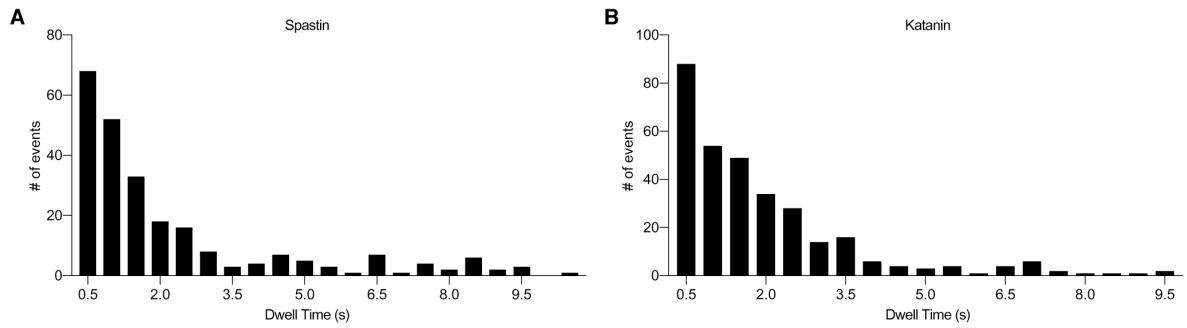

Fig. S9. Residence times of EB1-GFP lattice puncta
(**A**) Dwell times of EB1-GFP puncta on dynamic microtubules at 10 mM tubulin in the presence of 25 nM spastin and 1mM ATP; n=244. (**B**) Dwell times of EB1-GFP puncta on dynamic microtubules at 10 mM tubulin in the presence of 25 nM katanin and 1mM ATP, n=318.

Supplementary Figure 9 analyzed and made by Dr. Jeffrey Spector with data gathered by me and Dr. Ewa Szczesna

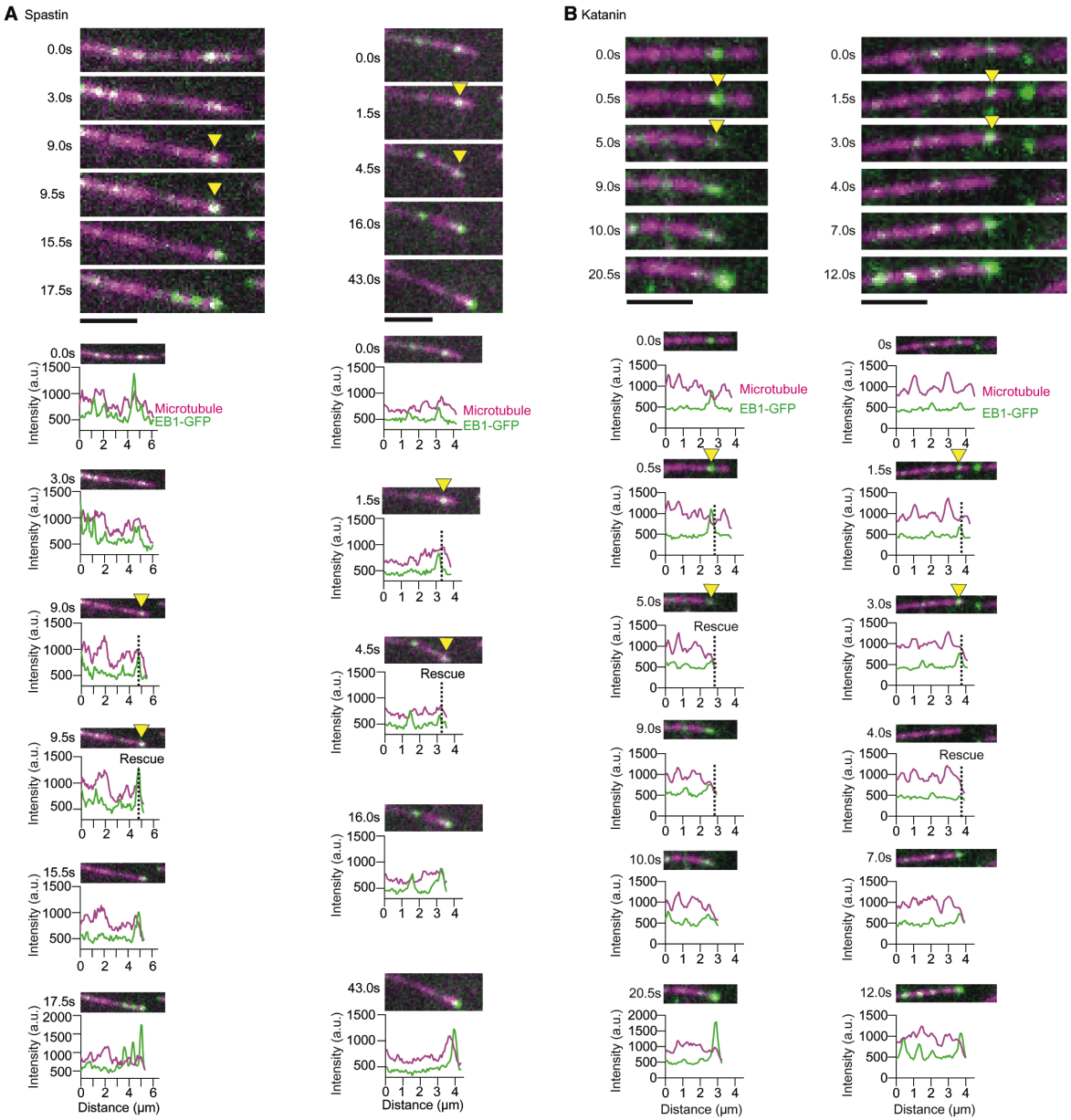

Figure S10: Microtubule rescue at lattice EB1-GFP puncta
A) Representative time courses (top panels) of two depolymerizing microtubules (magenta) that rescue at a lattice EB1-GFP site (green) in the presence of spastin and ATP. Fluorescence line scans (bottom panels) along these microtubules showing EB1-GFP and tubulin intensities. Rescue sites are highlighted by yellow arrows and a dotted line. Scale bar, 2 μm. B) Representative time courses (top panels) of two depolymerizing microtubules (magenta) that rescue at a lattice EB1-GFP site (green) in the presence of katanin and ATP. Fluorescence line scans (bottom panels) along these microtubules showing EB1-GFP and tubulin intensities. Rescue sites are highlighted by yellow arrows and a dotted line. Scale bar, 2 μm.

Figure S10A contributed by Dr. Ewa Szczesna

CHAPTER 5: Concluding Remarks

Microtubules are dynamic cytoskeletal polymers that cycle through periods of growth and shrinkage, a phenomenon known as dynamic instability. This dynamic instability is essential for basic cellular functions such as cell division, differentiation, and motility. Not surprisingly, the microtubule cytoskeleton is highly regulated intrinsically by diverse tubulin isotypes and post-translational modifications and extrinsically by microtubule effectors. Misregulation of the microtubule cytoskeleton leads to severe neurodegenerative diseases, cancer, and cardiovascular disease.

In textbooks, microtubules are depicted as homogenous structures composed of repeating αβ tubulin heterodimers, but these heterodimers differ in sequence and are decorated with chemically diverse post-translational modifications (39, 40). Studies have established that tubulin isotypes and post-translational modifications are stereotyped. For example, βVI tubulin is found only in hematopoietic cells (214), βIII tubulin is found only in neuronal cells (58), βV tubulin is found in muscle cells (215). Glutamylated, detyrosinated, and acetylated tubulin is found on stable microtubules while dynamic microtubules are tyrosinated (40). *In vivo*, studies have shown cell types with different tubulin species have different dynamics (216, 217). However, we still do not know if these differences are due to changes in intrinsic microtubule dynamic properties or due to microtubule effector recruitment. *In vitro*, studies have shown that tubulin purified from various tissue sources have different microtubule dynamics (65, 68-70). However, in these studies the tubulin species are not well defined, i.e. there are unknown α-tubulin isotypes and the post-translational modification state of the tubulin is unknown.

Understanding the relationship between tubulin sequence and dynamics has been a longstanding question in the microtubule field because of this lack of well-defined tubulin

species. This is because the majority of in vitro microtubule studies have been performed with tubulin purified from brain tissue (66). Brain tubulin is heterogeneous with multiple tubulin isotypes as well and post-translational modifications. Therefore, brain tubulin is not a good tool to study how a single tubulin isoform or post-translational modification affects microtubule dynamics (67).

I have been able to successfully purify unmodified tubulin in two different ways: 1) Using the baculovirus expression systems (71), our lab has been able to successfully purify a single tubulin isotype, human neuronal unmodified α1A/βIII tubulin, free of any insect tubulin contaminants and 2) using the tubulin-affinity method (162), I have been able to purify tubulin in mg amounts suited for in vitro microtubule dynamics assays from tsA201 cells that contain unmodified α1B/βI+βIVb tubulin. Using these two well-defined tubulin species, I performed in vitro microtubule dynamics assays. I found that α1B/βI+βIVb grow twice as fast and catastrophe half as much when compared to heterogenous brain tubulin, showing that different tubulin compositions can have drastically different dynamic properties. I also found that the addition of α1A/βIII tubulin tuned α1B/βI+βIVb tubulin dynamics proportionally. Therefore, by modulating the relative expression levels of tubulin isotypes, cells can tune microtubule dynamics, which could explain the differences in dynamics in cells when tubulin compositions change during tumorigenesis.

The ability to purify tubulin recombinantly will finally give us the opportunity to understand the relationship between tubulin sequence, structure and dynamics. How do the different tubulin isotypes differ in dynamics, structure, and microtubule effector and motor recruitment? What tubulin residues are essential for tuning tubulin GTPase activity? How do the tubulin mutations found in patients change microtubule dynamics or MAP recruitment? These

questions are just the tip of the iceberg to uncovering exciting insights in how amino acid changes in tubulin can tune microtubule function.

Being able to purify unmodified tubulin and then modify the naïve tubulin with various "flavors" of post-translational modifications will allow us to systematically dissect how tubulin glutamylation, glycylation, acetylation, and detyrosination affect microtubule dynamics (73). Stable microtubules are marked with polyglutamylation and acetylation (218, 219). However, it is unclear whether these modifications confer stability directly or indirectly through the recruitment of MAPs. The ability to now make a single post-translationally modified species in vitro will allow us to understand the direct effects on microtubule dynamics. Controlled post-translational modifications of tubulin will also allow us to understand how cellular effectors respond to specific modifications. How do modifications change microtubule motor run lengths? Do microtubule motors or MAPs prefer binding to microtubules with a specific modification? All of these questions are exciting areas of exploration to further understand how tubulin diversity can change intrinsic microtubule dynamic properties and MAP recruitment.

Another way microtubule dynamics are tuned is by extrinsic factors. These extrinsic factors range from microtubule polymerases, which increase the tubulin on-rate to microtubule depolymerases, which promote microtubule catastrophes (20, 21). While we have an understanding of how these proteins affect microtubule dynamics, we do not understand how severing enzymes, spastin, katanin, and fidgetin affect microtubule dynamics. This is because the majority of the studies have used stabilized microtubules to study severing enzymes. Severing enzymes cause internal breaks in the microtubule in an ATP dependent manner. These enzymes are essential for the generation and maintenance of essential for microtubule arrays in neurons,

meiosis and mitosis, and the plant cortex (79, 80). Severing enzymes role in regulating microtubule dynamics has remained mysterious.

Together with a post-doc, Dr. Ewa Szczesna, in the lab, we found that severing enzymes do not simply break and destroy microtubules, but they catalyze the rejuvenation of microtubule with new tubulin throughout the microtubule shaft (220). This was very surprising to us because of the classical view of microtubule dynamics. It has been long thought that tubulin exchange solely happens at microtubule ends. GTP-tubulin is incorporated at the microtubule ends and eventually, the GTP is hydrolyzed to GDP. The unstable GDP microtubule lattice is unstable and is protected from depolymerizing by a GTP-tubulin cap. When the GTP-tubulin cap erodes, the GDP-tubulin is exposed and the microtubule depolymerizes i.e. undergoes catastrophe. Interestingly, we found that in the presence of severing enzymes, spastin and katanin, and soluble GTP-tubulin, the GTP tubulin not only gets incorporated at the microtubule tips, but along the microtubule lattice. Our study showed that severing enzymes pull out tubulin dimers from the microtubule shaft and these nano-damaged sites are repaired by soluble GTP-tubulin. We found these severing-mediated GTP-tubulin islands along the microtubule shaft had two very unexpected consequences: 1) the newly severed ends emerged with a high density of GTP-tubulin which stabilized the end against depolymerization and 2) these GTP-tubulin rich areas are hotspots for microtubule rescues therefore increasing microtubule rescue frequency in the presence of severing enzymes. The combination of these two processes leads to microtubule mass and number amplification. Therefore, we have shown that severing enzymes alone can amplify microtubules in a simplified *in vitro* system, without any additional factors.

When is this phenomenon beneficial? This is a useful mechanism for amplifying microtubule mass in the absence of a microtubule nucleator such as in acentrosomal microtule

arrays found in spindles, plant cortical arrays, and axonal microtubule arrays far from the microtubule nucleating center (192). Furthermore, our study can explain the paradoxical findings in vivo where loss of these severing enzymes in systems such as neurons, plants, and spindles leads to a loss in microtubule mass (105, 106).

The finding that severing enzymes introduce GTP-islands along the microtubule shaft brings interesting questions of how cells can regulate this process. One way severing enzymes is regulated is through tubulin post-translational modifications. Our lab and other labs have shown that spastin and katanin preferentially sever glutamylated microtubules (38, 187, 210). Glutamylation is found on stable microtubule arrays that have a slow turnover rate such as those found in cilia, axons, centrioles (19, 40). In these arrays, glutamylated tubulin dimers could be selectively removed by severing enzymes and "fresh" unmodified GTP-tubulin could be used to replace the removed dimers. Therefore, severing enzymes can act as microtubule array rejuvenators where dimers are removed and replaced, without completely destroying the microtubule arrays. Another way by which severing mediated to GTP-tubulin healing and microtubule amplification can be tuned is by other microtubule effectors. Cells have an arsenal of polymerases, depolymerases, or rescue promoting factors to tune tubulin on and off rates. What is the interplay between these factors and severing enzymes? How do they change microtubule amplification?

Our work also raises interesting questions regarding the microtubule damage and heals sites. What is the geometry of the damage sites? How many tubulin dimers are removed from these sites? Are the enzymes processively removing tubulin dimers from the lattice? What is the minimum number of GTP-tubulin incorporated into the microtubule lattice to promote microtubule rescue? Does the geometry of the GTP-tubulin incorporate matter to promote

rescue? All of these exciting questions will help us unlock how these fascinating molecular machines have the ability to rejuvenate and amplify microtubule arrays.

Recently, the Howard lab reported that spastin promotes microtubule number and mass amplification in two ways: 1) spastin severs microtubules in an ATP-dependent manner and 2) the newly severed ends depolymerize immediately after severing, but transition to growth (i.e. rescue) due to the passive binding of spastin along the microtubule lattice (221). The paper claims that the passive binding of the enzyme alone and not GTP-tubulin incorporation causes microtubule amplification. However, in this study, GTP-tubulin incorporation after spastin-mediated nano-damage is not shown (221). Moreover, the study reports that severing occurs within 2 minutes, which is slower compared to our study where we observe severing within 30 seconds of enzyme addition. So, if the rate of tubulin extraction is slow, the holes that the enzyme is making at any given time would also be smaller, therefore, the GTP-tubulin islands could potentially be small and not support the emergence of stable microtubule ends or microtubule rescue.

Furthermore, in our assays, we show that the GTP-tubulin is being correctly incorporated into the severing enzyme generated nano-damage sites by using EB1 as a marker. EB1 binds and recognizes GTP/GDP-Pi tubulin (176). In our assays, EB1 transiently binds to the microtubule lattice, indicative of the GTP bound to tubulin hydrolyzing to GDP. In the severing assays from the Howard paper, there is no indication of proper GTP-tubulin incorporation. Therefore, without validation of proper GTP-tubulin incorporation, the contribution of tubulin incorporation and its effects cannot be accessed.

Finally, in our assays, at 12μM tubulin, the microtubule growth rate (i.e. tubulin on-rate)

is approximately twice as fast as the growth rate reported in the Howard study. Therefore, if the rate of GTP-tubulin incorporation is slower in the Howard study, it is possible that the GTP-tubulin islands cannot support stable ends or rescue.

In summary, my graduate studies have shed light on how tubulin diversity can tune microtubule dynamics and has also revealed an unexpected finding that microtubule dynamics can be regulated through tubulin exchange along the microtubule shaft. I hope that these outcomes will contribute to the exploration of the interplay between intrinsic and extrinsic microtubule dynamic regulation, which is essential for the fidelity of basic cellular processes.

LITERATURE CITED

1. Slautterback DB (1963) Cytoplasmic Microtubules. I. Hydra. *J. Cell Biol.* 18:367-388.
2. Ledbetter MC,Porter KR (1963) A "Microtubule" in Plant Cell Fine Structure. *J. Cell Biol.* 19(1):239-250.
3. Mathur J,Hulskamp M (2002) Microtubules and microfilaments in cell morphogenesis in higher plants. *Curr. Biol.* 12(19):R669-676.
4. Cyr RJ (1994) Microtubules in plant morphogenesis: role of the cortical array. *Annu Rev Cell Biol* 10:153-180.
5. Sakakibara A, Ando R, Sapir T, Tanaka T (2013) Microtubule dynamics in neuronal morphogenesis. *Open Biol* 3(7):130061.
6. Etienne-Manneville S (2013) Microtubules in cell migration. *Annu. Rev. Cell. Dev. Biol.* 29:471-499.
7. Bouchet BP,Akhmanova A (2017) Microtubules in 3D cell motility. *J. Cell Sci.* 130(1):39-50.
8. Franker MA,Hoogenraad CC (2013) Microtubule-based transport - basic mechanisms, traffic rules and role in neurological pathogenesis. *J. Cell Sci.* 126(Pt 11):2319-2329.
9. Ross JL (2012) The impacts of molecular motor traffic jams. *Proc Natl Acad Sci U S A* 109(16):5911-5912.
10. Meunier S,Vernos I (2012) Microtubule assembly during mitosis - from distinct origins to distinct functions? *J. Cell Sci.* 125(Pt 12):2805-2814.
11. Forth S,Kapoor TM (2017) The mechanics of microtubule networks in cell division. *J. Cell Biol.* 216(6):1525-1531.
12. Lasser M, Tiber J, Lowery LA (2018) The Role of the Microtubule Cytoskeleton in Neurodevelopmental Disorders. *Front Cell Neurosci* 12:165.
13. Caporizzo MA, Chen CY, Prosser BL (2019) Cardiac microtubules in health and heart disease. *Exp Biol Med (Maywood)* 244(15):1255-1272.
14. Clark JA, Yeaman EJ, Blizzard CA, Chuckowree JA, Dickson TC (2016) A Case for Microtubule Vulnerability in Amyotrophic Lateral Sclerosis: Altered Dynamics During Disease. *Front Cell Neurosci* 10:204.
15. Pellegrini L, Wetzel A, Granno S, Heaton G, Harvey K (2017) Back to the tubule: microtubule dynamics in Parkinson's disease. *Cell. Mol. Life Sci.* 74(3):409-434.
16. Dumontet C,Jordan MA (2010) Microtubule-binding agents: a dynamic field of cancer therapeutics. *Nat. Rev. Drug Discov.* 9(10):790-803.
17. Chatterji BP, Jindal B, Srivastava S, Panda D (2011) Microtubules as antifungal and antiparasitic drug targets. *Expert Opin Ther Pat* 21(2):167-186.
18. Mitchison T,Kirschner M (1984) Dynamic instability of microtubule growth. *Nature* 312:237-242.
19. Roll-Mecak A (2019) How cells exploit tubulin diversity to build functional cellular microtubule mosaics. *Curr. Opin. Cell Biol.* 56:102-108.
20. Alfaro-Aco R,Petry S (2015) Building the Microtubule Cytoskeleton Piece by Piece. *J. Biol. Chem.* 290(28):17154-17162.

21. Akhmanova A,Steinmetz MO (2010) Microtubule+ TIPs at a glance. *J. Cell Sci.* 123(20):3415-3419.
22. Nogales E, Whittaker M, Milligan RA, Downing KH (1999) High-resolution model of the microtubule. *Cell* 96(1):79-88.
23. Nogales E, Wolf SG, Downing KH (1998) Structure of the alpha beta tubulin dimer by electron crystallography. *Nature* 391(6663):199-203.
24. Amos L,Klug A (1974) Arrangement of subunits in flagellar microtubules. *J. Cell Sci.* 14(3):523-549.
25. Mitchison TJ (1993) Localization of an exchangeable GTP binding site at the plus end of microtubules. *Science* 261(5124):1044-1047.
26. Hirose Y,Takiguchi T (1995) Microtubule changes in hematologic malignant cells treated with paclitaxel and comparison with vincristine cytotoxicity. *Blood Cells Mol Dis* 21(2):119-130.
27. Fan J, Griffiths AD, Lockhart A, Cross RA, Amos LA (1996) Microtubule minus ends can be labelled with a phage display antibody specific to alpha-tubulin. *J. Mol. Biol.* 259(3):325-330.
28. Allen C,Borisy GG (1974) Structural polarity and directional growth of microtubules of Chlamydomonas flagella. *J. Mol. Biol.* 90(2):381-402.
29. Evans L, Mitchison T, Kirschner M (1985) Influence of the centrosome on the structure of nucleated microtubules. *J. Cell Biol.* 100(4):1185-1191.
30. Desai A,Mitchison TJ (1997) Microtubule polymerization dynamics. *Annu. Rev. Cell. Dev. Biol.* 13:83-117.
31. Chaaban S,Brouhard GJ (2017) A microtubule bestiary: structural diversity in tubulin polymers. *Mol. Biol. Cell* 28(22):2924-2931.
32. Fukushige T*, et al.* (1999) MEC-12, an alpha-tubulin required for touch sensitivity in C. elegans. *J. Cell Sci.* 112 (Pt 3):395-403.
33. Savage C*, et al.* (1989) mec-7 is a beta-tubulin gene required for the production of 15-protofilament microtubules in Caenorhabditis elegans. *Genes Dev.* 3(6):870-881.
34. Prezel E*, et al.* (2018) Tau can switch microtubule network organizations: from random networks to dynamic and stable bundles. *Mol. Biol. Cell* 29(2):154-165.
35. Lowe J, Li H, Downing KH, Nogales E (2001) Refined structure of alpha beta-tubulin at 3.5 A resolution. *J. Mol. Biol.* 313(5):1045-1057.
36. Garnham CP,Roll-Mecak A (2012) The chemical complexity of cellular microtubules: Tubulin post-translational modification enzymes and their roles in tuning microtubule functions. *Cytoskeleton* 69(7):442-463.
37. Cross D, Dominguez J, Maccioni RB, Avila J (1991) MAP-1 and MAP-2 binding sites at the C-terminus of beta-tubulin. Studies with synthetic tubulin peptides. *Biochemistry* 30(17):4362-4366.
38. Valenstein ML,Roll-Mecak A (2016) Graded control of microtubule severing by tubulin glutamylation. *Cell* 164(5):911-921.
39. Roll-Mecak A (2015) Intrinsically disordered tubulin tails: complex tuners of microtubule functions? *Semin. Cell Dev. Biol.*, (Elsevier), pp 11-19.
40. Yu I, Garnham CP, Roll-Mecak A (2015) Writing and reading the tubulin code. *J. Biol. Chem.* 290(28):17163-17172.
41. Weisenberg RC, Borisy GG, Taylor EW (1968) The colchicine-binding protein of mammalian brain and its relation to microtubules. *Biochemistry* 7(12):4466-4479.

42. Spiegelman BM, Penningroth SM, Kirschner MW (1977) Turnover of tubulin and the N site GTP in Chinese hamster ovary cells. *Cell* 12(3):587-600.
43. David-Pfeuty T, Erickson HP, Pantaloni D (1977) Guanosinetriphosphatase activity of tubulin associated with microtubule assembly. *Proc Natl Acad Sci U S A* 74(12):5372-5376.
44. MacNeal RK,Purich DL (1978) Stoichiometry and role of GTP hydrolysis in bovine neurotubule assembly. *J. Biol. Chem.* 253(13):4683-4687.
45. Carlier MF,Pantaloni D (1981) Kinetic analysis of guanosine 5'-triphosphate hydrolysis associated with tubulin polymerization. *Biochemistry* 20(7):1918-1924.
46. Carlier M-F (1982) Guanosine-5′-triphosphate hydrolysis and tubulin polymerization. *Mol. Cell. Biochem.* 47(2):97-113.
47. VanBuren V, Odde DJ, Cassimeris L (2002) Estimates of lateral and longitudinal bond energies within the microtubule lattice. *Proc Natl Acad Sci U S A* 99(9):6035-6040.
48. Carlier MF, Didry D, Pantaloni D (1987) Microtubule elongation and guanosine 5'-triphosphate hydrolysis. Role of guanine nucleotides in microtubule dynamics. *Biochemistry* 26(14):4428-4437.
49. Verhey KJ,Gaertig J (2007) The tubulin code. *Cell cycle* 6(17):2152-2160.
50. Jenuwein T,Allis CD (2001) Translating the histone code. *Science* 293(5532):1074-1080.
51. Luduena RF (1998) Multiple forms of tubulin: different gene products and covalent modifications. *Int. Rev. Cytol.* 178:207-275.
52. Neff NF, Thomas JH, Grisafi P, Botstein D (1983) Isolation of the beta-tubulin gene from yeast and demonstration of its essential function in vivo. *Cell* 33(1):211-219.
53. Schatz PJ, Pillus L, Grisafi P, Solomon F, Botstein D (1986) Two functional alpha-tubulin genes of the yeast Saccharomyces cerevisiae encode divergent proteins. *Mol. Cell. Biol.* 6(11):3711-3721.
54. Theurkauf WE, Baum H, Bo J, Wensink PC (1986) Tissue-specific and constitutive alpha-tubulin genes of Drosophila melanogaster code for structurally distinct proteins. *Proc Natl Acad Sci U S A* 83(22):8477-8481.
55. Hoyle HD,Raff EC (1990) Two Drosophila beta tubulin isoforms are not functionally equivalent. *J. Cell Biol.* 111(3):1009-1026.
56. Raff EC, *et al.* (1982) Regulation of tubulin gene expression during embryogenesis in Drosophila melanogaster. *Cell* 28(1):33-40.
57. Bhattacharya R,Cabral F (2004) A ubiquitous beta-tubulin disrupts microtubule assembly and inhibits cell proliferation. *Mol. Biol. Cell* 15(7):3123-3131.
58. Banerjee A, *et al.* (1988) A monoclonal antibody against the type II isotype of beta-tubulin. Preparation of isotypically altered tubulin. *J. Biol. Chem.* 263(6):3029-3034.
59. Schwer HD, *et al.* (2001) A lineage-restricted and divergent beta-tubulin isoform is essential for the biogenesis, structure and function of blood platelets. *Curr. Biol.* 11(8):579-586.
60. Chen B, *et al.* (2017) Novel mutations and structural deletions in TUBB8: expanding mutational and phenotypic spectrum of patients with arrest in oocyte maturation, fertilization or early embryonic development. *Hum Reprod* 32(2):457-464.

61. Poirier K*, et al.* (2010) Mutations in the neuronal ss-tubulin subunit TUBB3 result in malformation of cortical development and neuronal migration defects. *Hum. Mol. Genet.* 19(22):4462-4473.
62. Shao Q*, et al.* (2019) Disease-associated mutations in human TUBB3 disturb netrin repulsive signaling. *PLoS One* 14(6):e0218811.
63. Saillour Y*, et al.* (2014) Beta tubulin isoforms are not interchangeable for rescuing impaired radial migration due to Tubb3 knockdown. *Hum. Mol. Genet.* 23(6):1516-1526.
64. Chalfie M,Thomson JN (1982) Structural and functional diversity in the neuronal microtubules of Caenorhabditis elegans. *J. Cell Biol.* 93(1):15-23.
65. Banerjee A, Roach MC, Trcka P, Luduena RF (1990) Increased microtubule assembly in bovine brain tubulin lacking the type III isotype of beta-tubulin. *J. Biol. Chem.* 265(3):1794-1799.
66. Weisenberg RC (1972) Microtubule formation in vitro in solutions containing low calcium concentrations. *Science* 177(4054):1104-1105.
67. Zambito AM, Knipling L, Wolff J (2002) Charge variants of tubulin, tubulin S, membrane-bound and palmitoylated tubulin from brain and pheochromocytoma cells. *Biochimica et Biophysica Acta (BBA)-Proteins and Proteomics* 1601(2):200-207.
68. Newton CN*, et al.* (2002) Intrinsically slow dynamic instability of HeLa cell microtubules in vitro. *J. Biol. Chem.* 277(45):42456-42462.
69. Trinczek B, Marx A, Mandelkow EM, Murphy DB, Mandelkow E (1993) Dynamics of microtubules from erythrocyte marginal bands. *Mol. Biol. Cell* 4(3):323-335.
70. Murphy DB,Wallis KT (1983) Isolation of microtubule protein from chicken erythrocytes and determination of the critical concentration for tubulin polymerization in vitro and in vivo. *J. Biol. Chem.* 258(13):8357-8364.
71. Minoura I, Hachikubo, Y., Yamakita, Y., Takazaki, H., Ayukawa, R., Uchimura, S. & Muto, E. (2013) Overexpression, purification, and functional analysis of recombinant human tubulin dimer. *FEBS Lett.* 587(21):3450-3455.
72. Widlund PO*, et al.* (2012) One-step purification of assembly-competent tubulin from diverse eukaryotic sources. *Mol. Biol. Cell* 23(22):4393-4401.
73. Vemu A, Garnham CP, Lee DY, Roll-Mecak A (2014) Generation of differentially modified microtubules using in vitro enzymatic approaches. *Methods Enzymol.* 540:149-166.
74. Vemu A*, et al.* (2016) Structure and Dynamics of Single-isoform Recombinant Neuronal Human Tubulin. *J. Biol. Chem.* 291(25):12907-12915.
75. Pamula MC, Ti SC, Kapoor TM (2016) The structured core of human beta tubulin confers isotype-specific polymerization properties. *J. Cell Biol.* 213(4):425-433.
76. Vemu A, Atherton J, Spector JO, Moores CA, Roll-Mecak A (2017) Tubulin isoform composition tunes microtubule dynamics. *Mol. Biol. Cell* 28(25):3564-3572.
77. Vale RD (1991) Severing of stable microtubules by a mitotically activated protein in Xenopus egg extracts. *Cell* 64(4):827-839.
78. McNally FJ,Vale RD (1993) Identification of katanin, an ATPase that severs and disassembles stable microtubules. *Cell* 75(3):419-429.
79. McNally FJ,Roll-Mecak A (2018) Microtubule-severing enzymes: From cellular functions to molecular mechanism. *J. Cell Biol.* 217(12):4057-4069.

80. Roll-Mecak A,McNally FJ (2010) Microtubule-severing enzymes. *Curr. Opin. Cell Biol.* 22(1):96-103.
81. Denton KR*, et al.* (2014) Loss of spastin function results in disease-specific axonal defects in human pluripotent stem cell-based models of hereditary spastic paraplegia. *Stem Cells* 32(2):414-423.
82. Kasher PR*, et al.* (2009) Direct evidence for axonal transport defects in a novel mouse model of mutant spastin-induced hereditary spastic paraplegia (HSP) and human HSP patients. *J. Neurochem.* 110(1):34-44.
83. Hu WF*, et al.* (2014) Katanin p80 regulates human cortical development by limiting centriole and cilia number. *Neuron* 84(6):1240-1257.
84. Mishra-Gorur K*, et al.* (2014) Mutations in KATNB1 cause complex cerebral malformations by disrupting asymmetrically dividing neural progenitors. *Neuron* 84(6):1226-1239.
85. Roll-Mecak A,Vale RD (2008) Structural basis of microtubule severing by the hereditary spastic paraplegia protein spastin. *Nature* 451(7176):363-367.
86. Hartman JJ,Vale RD (1999) Microtubule disassembly by ATP-dependent oligomerization of the AAA enzyme katanin. *Science* 286(5440):782-785.
87. Zehr E*, et al.* (2017) Katanin spiral and ring structures shed light on power stroke for microtubule severing. *Nat. Struct. Mol. Biol.* 24(9):717-725.
88. Iwaya N*, et al.* (2010) A common substrate recognition mode conserved between katanin p60 and VPS4 governs microtubule severing and membrane skeleton reorganization. *J. Biol. Chem.* 285(22):16822-16829.
89. Roll-Mecak A,Vale RD (2005) The Drosophila homologue of the hereditary spastic paraplegia protein, spastin, severs and disassembles microtubules. *Curr. Biol.* 15(7):650-655.
90. McNally KP, Bazirgan OA, McNally FJ (2000) Two domains of p80 katanin regulate microtubule severing and spindle pole targeting by p60 katanin. *J. Cell Sci.* 113 (Pt 9):1623-1633.
91. Hartman JJ*, et al.* (1998) Katanin, a microtubule-severing protein, is a novel AAA ATPase that targets to the centrosome using a WD40-containing subunit. *Cell* 93(2):277-287.
92. Jiang K*, et al.* (2017) Microtubule minus-end regulation at spindle poles by an ASPM-katanin complex. *Nat. Cell Biol.* 19(5):480-492.
93. McNally K*, et al.* (2014) Katanin maintains meiotic metaphase chromosome alignment and spindle structure in vivo and has multiple effects on microtubules in vitro. *Mol. Biol. Cell* 25(7):1037-1049.
94. Wang C*, et al.* (2017) KTN80 confers precision to microtubule severing by specific targeting of katanin complexes in plant cells. *EMBO J.* 36(23):3435-3447.
95. McNally FJ, Okawa K, Iwamatsu A, Vale RD (1996) Katanin, the microtubule-severing ATPase, is concentrated at centrosomes. *J. Cell Sci.* 109 (Pt 3):561-567.
96. Gittes F, Mickey B, Nettleton J, Howard J (1993) Flexural rigidity of microtubules and actin filaments measured from thermal fluctuations in shape. *J. Cell Biol.* 120(4):923-934.
97. McNally FJ,Vale RD (1993) Identification of katanin, an ATPase that severs and disassembles stable microtubules. *Cell* 75(3):419-429.

98. Loughlin R, Wilbur JD, McNally FJ, Nedelec FJ, Heald R (2011) Katanin contributes to interspecies spindle length scaling in Xenopus. *Cell* 147(6):1397-1407.
99. Mao C-X*, et al.* (2014) Microtubule-severing protein Katanin regulates neuromuscular junction development and dendritic elaboration in Drosophila. *Development* 141(5):1064-1074.
100. Lee HH, Jan LY, Jan YN (2009) Drosophila IKK-related kinase Ik2 and Katanin p60-like 1 regulate dendrite pruning of sensory neuron during metamorphosis. *Proc Natl Acad Sci U S A* 106(15):6363-6368.
101. Kage E*, et al.* (2005) MBR-1, a novel helix-turn-helix transcription factor, is required for pruning excessive neurites in Caenorhabditis elegans. *Curr. Biol.* 15(17):1554-1559.
102. Riccomagno MM,Kolodkin AL (2015) Sculpting neural circuits by axon and dendrite pruning. *Annu. Rev. Cell. Dev. Biol.* 31:779-805.
103. Lindeboom JJ*, et al.* (2013) A mechanism for reorientation of cortical microtubule arrays driven by microtubule severing. *Science* 342(6163):1245533.
104. Srayko M, O'Toole ET, Hyman AA, Müller-Reichert T (2006) Katanin disrupts the microtubule lattice and increases polymer number in C. elegans meiosis. *Curr. Biol.* 16(19):1944-1949.
105. Roll-Mecak A,Vale RD (2006) Making more microtubules by severing: a common theme of noncentrosomal microtubule arrays? *J. Cell Biol.* 175(6):849-851.
106. Ribbeck K,Mitchison TJ (2006) Meiotic spindle: sculpted by severing. *Curr. Biol.* 16(21):R923-R925.
107. Sherwood NT, Sun Q, Xue M, Zhang B, Zinn K (2004) Drosophila spastin regulates synaptic microtubule networks and is required for normal motor function. *PLoS Biol.* 2(12):e429.
108. Wood JD*, et al.* (2006) The microtubule-severing protein Spastin is essential for axon outgrowth in the zebrafish embryo. *Hum. Mol. Genet.* 15(18):2763-2771.
109. Walker RA, Inoue S, Salmon ED (1989) Asymmetric behavior of severed microtubule ends after ultraviolet-microbeam irradiation of individual microtubules in vitro. *J. Cell Biol.* 108(3):931-937.
110. Tran PT, Walker RA, Salmon ED (1997) A metastable intermediate state of microtubule dynamic instability that differs significantly between plus and minus ends. *J. Cell Biol.* 138(1):105-117.
111. Spurck TP*, et al.* (1990) UV microbeam irradiations of the mitotic spindle. II. Spindle fiber dynamics and force production. *J. Cell Biol.* 111(4):1505-1518.
112. Brugues J, Nuzzo V, Mazur E, Needleman DJ (2012) Nucleation and transport organize microtubules in metaphase spindles. *Cell* 149(3):554-564.
113. Nicklas RB, Lee GM, Rieder CL, Rupp G (1989) Mechanically cut mitotic spindles: clean cuts and stable microtubules. *J. Cell Sci.* 94 (Pt 3):415-423.
114. Tirnauer JS, Salmon ED, Mitchison TJ (2004) Microtubule plus-end dynamics in Xenopus egg extract spindles. *Mol. Biol. Cell* 15(4):1776-1784.
115. Bieling P*, et al.* (2007) Reconstitution of a microtubule plus-end tracking system in vitro. *Nature* 450(7172):1100-1105.
116. Brouhard GJ*, et al.* (2008) XMAP215 is a processive microtubule polymerase. *Cell* 132(1):79-88.

117. Leandro-García LJ*, et al.* (2010) Tumoral and tissue-specific expression of the major human β-tubulin isotypes. *Cytoskeleton* 67(4):214-223.
118. Miller KE,Joshi HC (1996) Tubulin transport in neurons. *J. Cell Biol.* 133(6):1355-1366.
119. Sullivan KF,Cleveland DW (1986) Identification of conserved isotype-defining variable region sequences for four vertebrate beta tubulin polypeptide classes. *Proceedings of the National Academy of Sciences* 83(12):4327-4331.
120. Panda D, Miller, H. P., Banergee, A., Ludena, R. F. & Wilson, L. (1994) Microtubule dynamics in vitro are regulated by the tubulin isotype composition. *Proc Natl Acad Sci* 91:11358-11362.
121. Sirajuddin M, Rice, L. M. & Vale, R. D. (2014) Regulation of microtubule motors by tubulin isotypes and post-translational modifications. *Nat. Cell Bio.* 16:335-344.
122. Atherton J*, et al.* (2014) Conserved mechanisms of microtubule-stimulated ADP release, ATP binding, and force generation in transport kinesins. *Elife* 3:e03680.
123. Kremer JR, Mastronarde DN, McIntosh JR (1996) Computer visualization of three-dimensional image data using IMOD. *J. Struct. Biol.* 116(1):71-76.
124. Abrishami V*, et al.* (2015) Alignment of direct detection device micrographs using a robust Optical Flow approach. *J. Struct. Biol.* 189(3):163-176.
125. de la Rosa-Trevin JM*, et al.* (2013) Xmipp 3.0: an improved software suite for image processing in electron microscopy. *J. Struct. Biol.* 184(2):321-328.
126. Mindell JA,Grigorieff N (2003) Accurate determination of local defocus and specimen tilt in electron microscopy. *J. Struct. Biol.* 142(3):334-347.
127. Ludtke SJ, Baldwin PR, Chiu W (1999) EMAN: semiautomated software for high-resolution single-particle reconstructions. *J. Struct. Biol.* 128(1):82-97.
128. Sindelar CV,Downing KH (2007) The beginning of kinesin's force-generating cycle visualized at 9-A resolution. *J. Cell Biol.* 177(3):377-385.
129. Chen S*, et al.* (2013) High-resolution noise substitution to measure overfitting and validate resolution in 3D structure determination by single particle electron cryomicroscopy. *Ultramicroscopy* 135:24-35.
130. Emsley P, Lohkamp B, Scott WG, Cowtan K (2010) Features and development of Coot. *Acta Crystallogr D Biol Crystallogr* 66(Pt 4):486-501.
131. Zhang R, Alushin GM, Brown A, Nogales E (2015) Mechanistic Origin of Microtubule Dynamic Instability and Its Modulation by EB Proteins. *Cell* 162(4):849-859.
132. Brown A*, et al.* (2015) Tools for macromolecular model building and refinement into electron cryo-microscopy reconstructions. *Acta Crystallogr D Biol Crystallogr* 71(Pt 1):136-153.
133. Pecqueur L*, et al.* (2012) A designed ankyrin repeat protein selected to bind to tubulin caps the microtubule plus end. *Proc Natl Acad Sci U S A* 109(30):12011-12016.
134. Nicholls RA, Long F, Murshudov GN (2012) Low-resolution refinement tools in REFMAC5. *Acta Crystallogr D Biol Crystallogr* 68(Pt 4):404-417.
135. Gell C, Bormuth, V., Brouhard, G. J., Cohen, D. N., Diez, S., Friel, C. T., Helenius, J., Nitzsche, B., Petzold, H., Ribbe, J., Schaffer, E., Stear, J. H., Trushko, A., Varga, V., Widlund, P. O., Zanic, M. & Howard, J. (2010) Microtubule dynamics reconstituted *in vitro* and image by single-molecule fluorescence microscopy. *Methods Cell Biol.* 95:221-245.

136. Szyk A*, et al.* (2014) Molecular basis for age-dependent microtubule acetylation by tubulin acetyltransferase. *Cell* 157(6):1405-1415.
137. Ziółkowska NE,Roll-Mecak A (2013) In vitro microtubule severing assays. *Adhesion Protein Protocols*, (Springer), pp 323-334.
138. Toso RJ, Jordan MA, Farrell KW, Matsumoto B, Wilson L (1993) Kinetic stabilization of microtubule dynamic instability in vitro by vinblastine. *Biochemistry* 32(5):1285-1293.
139. Burgoyne RD, Cambray-Deakin MA, Lewis SA, Sarkar S, Cowan NJ (1988) Differential distribution of beta-tubulin isotypes in cerebellum. *The EMBO journal* 7(8):2311.
140. Kavallaris M (2010) Microtubules and resistance to tubulin-binding agents. *Nature Reviews Cancer* 10(3):194-204.
141. Peris L*, et al.* (2006) Tubulin tyrosination is a major factor affecting the recruitment of CAP-Gly proteins at microtubule plus ends. *J. Cell Biol.* 174(6):839-849.
142. Peris L*, et al.* (2009) Motor-dependent microtubule disassembly driven by tubulin tyrosination. *J. Cell Biol.* 185(7):1159-1166.
143. Vale RD, Coppin CM, Malik F, Kull FJ, Milligan RA (1994) Tubulin GTP hydrolysis influences the structure, mechanical properties, and kinesin-driven transport of microtubules. *J. Biol. Chem.* 269(38):23769-23775.
144. Garnham CP*, et al.* (2015) Multivalent Microtubule Recognition by Tubulin Tyrosine Ligase-like Family Glutamylases. *Cell* 161(5):1112-1123.
145. Alushin GM*, et al.* (2010) The Ndc80 kinetochore complex forms oligomeric arrays along microtubules. *Nature* 467(7317):805-810.
146. Alushin GM*, et al.* (2014) High-resolution microtubule structures reveal the structural transitions in αβ-tubulin upon GTP hydrolysis. *Cell* 157(5):1117-1129.
147. Cardone G, Heymann JB, Steven AC (2013) One number does not fit all: mapping local variations in resolution in cryo-EM reconstructions. *J. Struct. Biol.* 184(2):226-236.
148. Sousa D,Grigorieff N (2007) Ab initio resolution measurement for single particle structures. *J. Struct. Biol.* 157(1):201-210.
149. Horio TH, H. (1986) Visualization of the dynamic instability of individual microtubules by dark-field microscopy. *Nature* 321:605-607.
150. Mandelkow EM, Mandelkow E, Milligan RA (1991) Microtubule dynamics and microtubule caps: a time-resolved cryo-electron microscopy study. *J. Cell Biol.* 114(5):977-991.
151. Gardner MK, Zanic M, Gell C, Bormuth V, Howard J (2011) Depolymerizing kinesins Kip3 and MCAK shape cellular microtubule architecture by differential control of catastrophe. *Cell* 147(5):1092-1103.
152. Grishchuk EL, Molodtsov MI, Ataullakhanov FI, McIntosh JR (2005) Force production by disassembling microtubules. *Nature* 438(7066):384-388.
153. Podolski M, Mahamdeh M, Howard J (2014) Stu2, the budding yeast XMAP215/Dis1 homolog, promotes assembly of yeast microtubules by increasing growth rate and decreasing catastrophe frequency. *J. Biol. Chem.* 289(41):28087-28093.
154. Redeker V (2010) Mass spectrometry analysis of C-terminal posttranslational modifications of tubulins. *Methods in cell biology* 95:77-103.

155. Villasante A*, et al.* (1986) Six mouse alpha-tubulin mRNAs encode five distinct isotypes: testis-specific expression of two sister genes. *Mol. Cell. Biol.* 6(7):2409-2419.
156. Denoulet P, Eddé B, Gros F (1986) Differential expression of several neurospecific β-tubulin mRNAs in the mouse brain during development. *Gene* 50(1-3):289-297.
157. Wang D, Villasante A, Lewis SA, Cowan NJ (1986) The mammalian beta-tubulin repertoire: hematopoietic expression of a novel, heterologous beta-tubulin isotype. *J. Cell Biol.* 103(5):1903-1910.
158. Saillour Y*, et al.* (2014) Beta tubulin isoforms are not interchangeable for rescuing impaired radial migration due to Tubb3 knockdown. *Hum. Mol. Genet.* 23(6):1516-1526.
159. Hoyle HD,Raff EC (1990) Two Drosophila beta tubulin isoforms are not functionally equivalent. *J. Cell Biol.* 111(3):1009-1026.
160. Weisenberg RC, Broisy GG, Taylor EW (1968) Colchicine-binding protein of mammalian brain and its relation to microtubules. *Biochemistry* 7(12):4466-4479.
161. Murphy DB,Wallis KT (1986) Erythrocyte microtubule assembly in vitro. Tubulin oligomers limit the rate of microtubule self-assembly. *J. Biol. Chem.* 261(5):2319-2324.
162. Widlund PO*, et al.* (2012) One-step purification of assembly-competent tubulin from diverse eukaryotic sources. *Mol. Biol. Cell* 23(22):4393-4401.
163. Lopata MA,Cleveland DW (1987) In vivo microtubules are copolymers of available beta-tubulin isotypes: localization of each of six vertebrate beta-tubulin isotypes using polyclonal antibodies elicited by synthetic peptide antigens. *J. Cell Biol.* 105(4):1707-1720.
164. Rao S, Aberg F, Nieves E, Band Horwitz S, Orr GA (2001) Identification by mass spectrometry of a new alpha-tubulin isotype expressed in human breast and lung carcinoma cell lines. *Biochemistry* 40(7):2096-2103.
165. Hiser L*, et al.* (2006) Comparison of beta-tubulin mRNA and protein levels in 12 human cancer cell lines. *Cell Motil. Cytoskeleton* 63(1):41-52.
166. Vemu A, Garnham CP, Lee D-Y, Roll-Mecak A (2014) Generation of differentially modified microtubules using in vitro enzymatic approaches. *Methods Enzymol.* 540:149-166.
167. Castoldi M,Popov AV (2003) Purification of brain tubulin through two cycles of polymerization–depolymerization in a high-molarity buffer. *Protein Expression Purif.* 32(1):83-88.
168. Ray S, Meyhofer E, Milligan RA, Howard J (1993) Kinesin follows the microtubule's protofilament axis. *J. Cell Biol.* 121(5):1083-1093.
169. Schindelin J*, et al.* (2012) Fiji: an open-source platform for biological-image analysis. *Nat. Methods* 9(7):676-682.
170. Chrétien D, Fuller SD, Karsenti E (1995) Structure of growing microtubule ends: two-dimensional sheets close into tubes at variable rates. *J. Cell Biol.* 129(5):1311-1328.
171. Coombes CE, Yamamoto A, Kenzie MR, Odde DJ, Gardner MK (2013) Evolving tip structures can explain age-dependent microtubule catastrophe. *Curr. Biol.* 23(14):1342-1348.

172. Rice LM, Montabana EA, Agard DA (2008) The lattice as allosteric effector: structural studies of alphabeta- and gamma-tubulin clarify the role of GTP in microtubule assembly. *Proc Natl Acad Sci U S A* 105(14):5378-5383.
173. Wang HW,Nogales E (2005) Nucleotide-dependent bending flexibility of tubulin regulates microtubule assembly. *Nature* 435(7044):911-915.
174. Bieling P*, et al.* (2007) Reconstitution of a microtubule plus-end tracking system in vitro. *Nature* 450(7172):1100-1105.
175. Kumar P,Wittmann T (2012) + TIPs: SxIPping along microtubule ends. *Trends Cell Biol.* 22(8):418-428.
176. Maurer SP, Fourniol FJ, Bohner G, Moores CA, Surrey T (2012) EBs recognize a nucleotide-dependent structural cap at growing microtubule ends. *Cell* 149(2):371-382.
177. Walczak CE, Mitchison TJ, Desai A (1996) XKCM1: a Xenopus kinesin-related protein that regulates microtubule dynamics during mitotic spindle assembly. *Cell* 84(1):37-47.
178. Pamula MC, Ti S-C, Kapoor TM (2016) The structured core of human β tubulin confers isotype-specific polymerization properties. *J. Cell Biol.* 213(4):425-433.
179. Wade RH, Chrétien D, Job D (1990) Characterization of microtubule protofilament numbers: how does the surface lattice accommodate? *J. Mol. Biol.* 212(4):775-786.
180. Trotta N, Orso G, Rossetto MG, Daga A, Broadie K (2004) The hereditary spastic paraplegia gene, spastin, regulates microtubule stability to modulate synaptic structure and function. *Curr. Biol.* 14(13):1135-1147.
181. Ahmad FJ, Yu W, McNally FJ, Baas PW (1999) An essential role for katanin in severing microtubules in the neuron. *J. Cell Biol.* 145(2):305-315.
182. Stone MC*, et al.* (2012) Normal spastin gene dosage is specifically required for axon regeneration. *Cell Rep* 2(5):1340-1350.
183. Stoppin-Mellet V, Gaillard J, Vantard M (2006) Katanin's severing activity favors bundling of cortical microtubules in plants. *Plant J.* 46(6):1009-1017.
184. Zhang Q, Fishel E, Bertroche T, Dixit R (2013) Microtubule severing at crossover sites by katanin generates ordered cortical microtubule arrays in Arabidopsis. *Curr. Biol.* 23(21):2191-2195.
185. Zhang D, Rogers GC, Buster DW, Sharp DJ (2007) Three microtubule severing enzymes contribute to the "Pacman-flux" machinery that moves chromosomes. *J. Cell Biol.* 177(2):231-242.
186. McNally K, Audhya A, Oegema K, McNally FJ (2006) Katanin controls mitotic and meiotic spindle length. *J. Cell Biol.* 175(6):881-891.
187. Sharma N*, et al.* (2007) Katanin regulates dynamics of microtubules and biogenesis of motile cilia. *J. Cell Biol.* 178(6):1065-1079.
188. Connell JW, Lindon C, Luzio JP, Reid E (2009) Spastin couples microtubule severing to membrane traffic in completion of cytokinesis and secretion. *Traffic* 10(1):42-56.
189. Guizetti J*, et al.* (2011) Cortical constriction during abscission involves helices of ESCRT-III-dependent filaments. *Science* 331(6024):1616-1620.
190. Karabay A, Yu W, Solowska JM, Baird DH, Baas PW (2004) Axonal growth is sensitive to the levels of katanin, a protein that severs microtubules. *The Journal of neuroscience* 24(25):5778-5788.

191. Charafeddine RA*, et al.* (2015) Fidgetin-Like 2: A Microtubule-Based Regulator of Wound Healing. *J Invest Dermatol* 135(9):2309-2318.
192. Roll-Mecak A,McNally FJ (2010) Microtubule-severing enzymes. *Curr. Opin. Cell Biol.* 22(1):96-103.
193. Yigit G*, et al.* (2016) A syndrome of microcephaly, short stature, polysyndactyly, and dental anomalies caused by a homozygous KATNB1 mutation. *Am. J. Med. Genet. A* 170(3):728-733.
194. Burk DH,Ye ZH (2002) Alteration of oriented deposition of cellulose microfibrils by mutation of a katanin-like microtubule-severing protein. *Plant Cell* 14(9):2145-2160.
195. Ziolkowska NE,Roll-Mecak A (2013) In vitro microtubule severing assays. *Methods Mol Biol* 1046:323-334.
196. Albee AJ,Wiese C (2008) Xenopus TACC3/maskin is not required for microtubule stability but is required for anchoring microtubules at the centrosome. *Mol. Biol. Cell* 19(8):3347-3356.
197. Edelstein AD*, et al.* (2014) Advanced methods of microscope control using muManager software. *J Biol Methods* 1(2).
198. Gibbons IR,Fronk E (1979) A latent adenosine triphosphatase form of dynein 1 from sea urchin sperm flagella. *J. Biol. Chem.* 254(1):187-196.
199. Zhang D*, et al.* (2011) Drosophila katanin is a microtubule depolymerase that regulates cortical-microtubule plus-end interactions and cell migration. *Nat. Cell Biol.* 13(4):361-369.
200. Aumeier C*, et al.* (2016) Self-repair promotes microtubule rescue. *Nat. Cell Biol.* 18(10):1054-1064.
201. Schaedel L*, et al.* (2015) Microtubules self-repair in response to mechanical stress. *Nat Mater* 14(11):1156-1163.
202. Bailey ME, Sackett DL, Ross JL (2015) Katanin Severing and Binding Microtubules Are Inhibited by Tubulin Carboxy Tails. *Biophys. J.* 109(12):2546-2561.
203. Hiller G,Weber K (1978) Radioimmunoassay for tubulin: a quantitative comparison of the tubulin content of different established tissue culture cells and tissues. *Cell* 14(4):795-804.
204. Itzhak DN, Tyanova S, Cox J, Borner GH (2016) Global, quantitative and dynamic mapping of protein subcellular localization. *Elife* 5.
205. Dimitrov A*, et al.* (2008) Detection of GTP-tubulin conformation in vivo reveals a role for GTP remnants in microtubule rescues. *Science* 322(5906):1353-1356.
206. Al-Bassam J*, et al.* (2010) CLASP promotes microtubule rescue by recruiting tubulin dimers to the microtubule. *Dev. Cell* 19(2):245-258.
207. Ichihara K, Kitazawa H, Iguchi Y, Hotani H, Itoh TJ (2001) Visualization of the stop of microtubule depolymerization that occurs at the high-density region of microtubule-associated protein 2 (MAP2). *J. Mol. Biol.* 312(1):107-118.
208. Zanic M, Stear JH, Hyman AA, Howard J (2009) EB1 recognizes the nucleotide state of tubulin in the microtubule lattice. *PLoS One* 4(10):e7585.
209. Maurer SP, Fourniol FJ, Bohner G, Moores CA, Surrey T (2012) EBs recognize a nucleotide-dependent structural cap at growing microtubule ends. *Cell* 149(2):371-382.

210. Lacroix B*, et al.* (2010) Tubulin polyglutamylation stimulates spastin-mediated microtubule severing. *J. Cell Biol.* 189(6):945-954.
211. Nakata T, Niwa S, Okada Y, Perez F, Hirokawa N (2011) Preferential binding of a kinesin-1 motor to GTP-tubulin-rich microtubules underlies polarized vesicle transport. *J. Cell Biol.* 194(2):245-255.
212. Chan AY, Bailly M, Zebda N, Segall JE, Condeelis JS (2000) Role of cofilin in epidermal growth factor-stimulated actin polymerization and lamellipod protrusion. *J. Cell Biol.* 148(3):531-542.
213. DesMarais V, Ghosh M, Eddy R, Condeelis J (2005) Cofilin takes the lead. *J. Cell Sci.* 118(Pt 1):19-26.
214. Wang D, Villasante A, Lewis SA, Cowan NJ (1986) The mammalian beta-tubulin repertoire: hematopoietic expression of a novel, heterologous beta-tubulin isotype. *J. Cell Biol.* 103(5):1903-1910.
215. Randazzo D*, et al.* (2019) Persistent upregulation of the beta-tubulin tubb6, linked to muscle regeneration, is a source of microtubule disorganization in dystrophic muscle. *Hum. Mol. Genet.* 28(7):1117-1135.
216. Wadsworth P,McGrail M (1990) Interphase microtubule dynamics are cell type-specific. *J. Cell Sci.* 95 (Pt 1):23-32.
217. Shelden E,Wadsworth P (1993) Observation and quantification of individual microtubule behavior in vivo: microtubule dynamics are cell-type specific. *J. Cell Biol.* 120(4):935-945.
218. Schulze E,Kirschner M (1987) Dynamic and stable populations of microtubules in cells. *J. Cell Biol.* 104(2):277-288.
219. Webster DR,Borisy GG (1989) Microtubules are acetylated in domains that turn over slowly. *J. Cell Sci.* 92 (Pt 1):57-65.
220. Vemu A*, et al.* (2018) Severing enzymes amplify microtubule arrays through lattice GTP-tubulin incorporation. *Science* 361(6404).
221. Kuo YW, Trottier O, Mahamdeh M, Howard J (2019) Spastin is a dual-function enzyme that severs microtubules and promotes their regrowth to increase the number and mass of microtubules. *Proc Natl Acad Sci U S A* 116(12):5533-5541.

CURRICULUM VITAE

Annapurna Vemu
avemu26@gmail.com

Education

2014-2020 Ph.D., Biology
National Institutes of Health/Johns Hopkins University Graduate Partnership Program
Thesis Title: Regulation of microtubule dynamics by tubulin diversity and severing enzymes

2011-2012 M.S., Chemistry
University of California, San Diego

2007-2011 B.S., Biochemistry/Chemistry
University of California, San Diego

Research Experience

2014-2020 Pre-doctoral Trainee
Cell Biology and Biophysical Unit, National Institute of Neurological Disorders and Stroke, National Institutes of Health

2012-2014 Post-baccalaureate Fellow
Cell Biology and Biophysical Unit, National Institute of Neurological Disorders and Stroke, National Institutes of Health

2009-2012 Research Assistant
University of California San Diego

Honors and Awards

2017 Best Poster at Graduate Student Symposium
2009 Provost Honors, University of California San Diego

Publications

1. Spector JO, **Vemu A**, Roll-Mecak A. In Vitro Microtubule Dynamics Assays Using Dark-Field Microscopy. Methods Mol Biol. 2020;2101:39-51. doi: 10.1007/978-1-0716-0219-5_4. PubMed PMID: 31879897.
2. **Vemu A***, Szczesna E*, Roll-Mecak A. In Vitro Reconstitution Assays of Microtubule Amplification and Lattice Repair by the Microtubule-Severing Enzymes Katanin and Spastin. Methods Mol Biol. 2020;2101:27-38. doi: 10.1007/978-1-0716-0219-5_3. PubMed PMID: 31879896.
3. Atherton J, Luo Y, Xiang S, Yang C, Rai A, Jiang K, Stangier M, **Vemu A**, Cook AD, Wang S, Roll-Mecak A, Steinmetz MO, Akhmanova A, Baldus M, Moores CA. Structural determinants of microtubule minus end preference in CAMSAP CKK

domains. Nat Commun. 2019 Nov 20;10(1):5236. doi: 10.1038/s41467-019-13247-6. PubMed PMID: 31748546; PubMed Central PMCID: PMC6868217.

4. **Vemu A***, Szczesna E*, Zehr EA, Spector JO, Grigorieff N, Deaconescu AM, Roll-Mecak A. Severing enzymes amplify microtubule arrays through lattice GTP-tubulin incorporation. Science. 2018 Aug 24;361(6404). doi: 10.1126/science.aau1504. PubMed PMID: 30139843; PubMed Central PMCID: PMC6510489.
5. **Vemu A**, Atherton J, Spector JO, Moores CA, Roll-Mecak A. Tubulin isoform composition tunes microtubule dynamics. Mol Biol Cell. 2017 Dec 1;28(25):3564-3572. doi: 10.1091/mbc.E17-02-0124. Epub 2017 Oct 11. PubMed PMID: 29021343; PubMed Central PMCID: PMC5706985.
6. **Vemu A***, Atherton J*, Spector JO, Szyk A, Moores CA, Roll-Mecak A. Structure and Dynamics of Single-isoform Recombinant Neuronal Human Tubulin. J Biol Chem. 2016 Jun 17;291(25):12907-15. doi: 10.1074/jbc.C116.731133. Epub 2016 Apr 25. PubMed PMID: 27129203; PubMed Central PMCID: PMC4933209.
7. Garnham CP*, **Vemu A***, Wilson-Kubalek EM*, Yu I, Szyk A, Lander GC, Milligan RA, Roll-Mecak A. Multivalent Microtubule Recognition by Tubulin Tyrosine Ligase-like Family Glutamylases. Cell. 2015 May 21;161(5):1112-1123. doi: 10.1016/j.cell.2015.04.003. Epub 2015 May 7. PubMed PMID: 25959773; PubMed Central PMCID: PMC4465277.
8. **Vemu A***, Garnham CP*, Lee DY, Roll-Mecak A. Generation of differentially modified microtubules using in vitro enzymatic approaches. Methods Enzymol. 2014;540:149-66. doi: 10.1016/B978-0-12-397924-7.00009-1. PubMed PMID: 24630106.
9. Vu D, Huang DB, **Vemu A**, Ghosh G. A structural basis for selective dimerization by NF-κB RelB. J Mol Biol. 2013 Jun 12;425(11):1934-1945. doi: 10.1016/j.jmb.2013.02.020. Epub 2013 Feb 26. PubMed PMID: 23485337.

***** equal contribution

Oral Presentations

1. Severing enzymes amplify microtubule arrays through lattice GTP-tubulin incorporation, Biophysical Society Annual Meeting, 2019.
2. Severing enzymes amplify microtubule arrays through lattice GTP-tubulin incorporation, American Society of Cell Biology Annual Meeting, 2018.
3. Severing enzymes amplify microtubule arrays through lattice GTP-tubulin incorporation, Johns Hopkins Graduate Student Retreat, 2018.
4. Tubulin composition tunes microtubule dynamics, American Society of Cell Biology Annual Meeting, 2018.